

AD-A109 681

FOREIGN TECHNOLOGY DIV WRIGHT-PATTERSON AFB OH  
JOURNAL OF AERONAUTICS AND ASTRONOMY.(U)

F/G 20/4

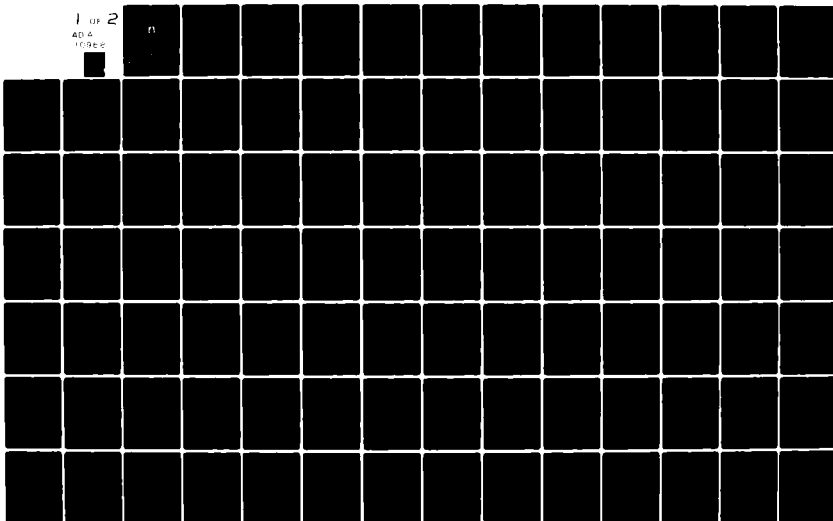
DEC 81

UNCLASSIFIED FTD-ID(RS)T-0722-81

NL

1 OF 2

AD-A  
109681





2.8



3.2



4

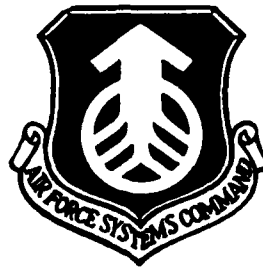


MIKROSKOP-RESOLUTION-TEST-CHART  
nach DIN EN 61970:2000

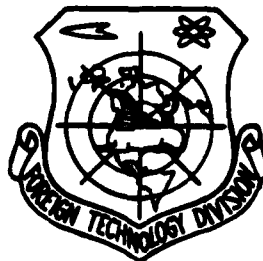
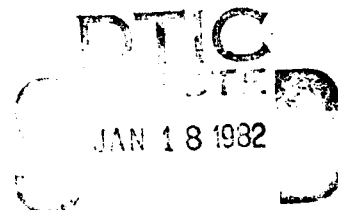
②

AD A109681

# FOREIGN TECHNOLOGY DIVISION



JOURNAL OF AERONAUTICS AND ASTRONOMY



01 15 82 069

Approved for public release;  
distribution unlimited.

DTIC FILE COPY



## EDITED TRANSLATION

FTD-ID(RS)T-0722-81

11 December 1981

MICROFICHE NR: FTD-81-C-002020

JOURNAL OF AERONAUTICS AND ASTRONOMY

English pages: 179

Source: Acta Aeronautica et Astronautica Sinica, Vol. 1, Nr. 1,  
1980, pp. 1-104

Country of origin: China

Translated by: SCITRAN  
F33657-81-D-0263

Requester: FTD/TQTA

Approved for public release; distribution unlimited.

Accession For
NTIS GEM1
DTIC
Unclassified
For Release
A

THIS TRANSLATION IS A RENDITION OF THE ORIGINAL FOREIGN TEXT WITHOUT ANY ANALYTICAL OR EDITORIAL COMMENT. STATEMENTS OR THEORIES ADVOCATED OR IMPLIED ARE THOSE OF THE SOURCE AND DO NOT NECESSARILY REFLECT THE POSITION OR OPINION OF THE FOREIGN TECHNOLOGY DIVISION.

PREPARED BY:

TRANSLATION DIVISION  
FOREIGN TECHNOLOGY DIVISION  
WP.AFB, OHIO.

# ACTA AERONAUTICA ET ASTRONAUTICA SINICA

(Quarterly)

Volume 1 Number 1 September 1980

---

## CONTENTS

An Approximate Analytical Method for Vortex-lift and Centre of Pressure on the Slender Wing Yin Xieyuan (The Science and Technology University of China) .....	1
A Penalty Function Method for Structural Optimum Design with Aeroelastic Constraints Wang Xianxin (Aerodynamic Research Centre of China) .....	12
An Aeronautical Structural Analysis System for Static Analysis(HAJIF-I) (The team for developing HAJIF-I Penned by Feng Zhongyue) .....	27
A Family of Tapered Beam Conforming Elements and Its Application to Beam Natural Vibration Analysis Zhu Derhao (Beijing Institute of Aeronautics and Astronautics) .....	51
Calculation of Internal and External Flow Field and Cowl Pressure Drag in the Supersonic Axisymmetric Nose Inlets Zhao Weimin Xu Suiwen (Power Plant Research Laboratory, Beijing Research Institute, Precision Machinery Corporation of China) .....	73
The Method for Calculating the Fuel Concentration Field in the Downstream Positions of the Pressure Jet Atomizer in the High Temperature Gas-stream Fu Weibiao (Tsinghua University) .....	95
A Vehicle Attitude Control System Forming the Error Signal by way of the Optimal Rotation Axis	

Dai Zongli Shi Ruohua (Beijing Institute of Control Engineering) Bi Dachuan (Institute of System Science and Mathematical Science Academia Sinica) .....	110
On the Application of Self-adaptive Flight Control System Based on Energy Balance Theory Li Lichun (Institute of Automatic Flight Control System) .....	128
Digital Filter Network Design by Using Observers Zhang Fuzhong (Beijing Electrical and Mechanical Engineering Institute) .....	144
On the Derivation of Bézier's Basic Functions Shi Fazhong, Han Daokang (Beijing Institute of Aeronautics and Astronautics) .....	161

#### SOCIETY NEWS

The Completely Successful Visit to USA by the Delegation of Chinese Society of Aeronautics and Astronautics .....	172
The Visit to China by the Delegation of Japan Society for Aeronautical and Space Sciences .....	173
The Conference on the Policy of CAGD/CAM Technique Development .....	174

# AN APPROXIMATE ANALYTICAL METHOD FOR VORTEX-LIFT AND CENTER OF PRESSURE ON THE SLENDER WING

Yin Xieyuan  
(The Science and Technology University of China)

## ABSTRACT

This paper presents a simplified analytical method for estimating the vortex-lift at the leading edge and the side edges as well as the center of pressure. It also provides two empirical correction functions. In comparison with other methods and the experimental data, this method offers good accuracy and is suitable for the needs of engineering design work.

During recent years, more and more people are interested in the nonlinear aerodynamics at high angle of attack. It mainly studies the nonlinear effects of the flow which is primarily characterized by detached vortex separation. It studies the formation, development and disintegration of a detached vortex as well as the effect of a detached vortex on the aerodynamic properties of the flying vehicle. Furthermore, it also studies the effective control and usage of a detached vortex, etc. It is a very important and active research area in the aeronautic circle at the present time.

At the present moment, there have been several theories already developed to calculate the aerodynamic characteristics of the front fringe vortex separation of the wing. However, they must probably require the aid of a high speed electronic computer. The purpose of this paper is to find an approximate analytical solution for the fast estimation of the aerodynamic characteristics of various shapes of wings. This is very convenient and useful to the design department, especially in the preliminary design stage. The author has reported a simplified method [1] several years ago to calculate

the vortex-lift at the leading edge. On the basis of the theoretical results mentioned above in [1], this paper derives the equations for the vortex-lift and the center of pressure. In addition, in order to perform engineering estimations, this paper also offers two empirical correction equations on the basis of the theoretical considerations as mentioned above. Recently, Purvis [2] proposed an analytical solution. The author discovered that the method used in this paper gave very similar results as the ones obtained in [2]. Furthermore, this method is more convenient.

## I. ANALYSIS

The theory of "leading edge suction analogy" by Polhamus [3] coincides very well with experimental results. It has already been widely used in engineering. Based on that theory

$$C_{L_{v,LE}} = K_{v,T} \sin^2 \alpha \cos \alpha / \cos \Lambda \quad (1)$$

$$K_{v,T} = K_p \left( 1 - \frac{K_p}{1.4} \right)$$

where  $K_p$  and  $K_{v,T}$  are the derivatives of the potential flow lift coefficient and the leading edge propulsion coefficient, respectively.  $\Lambda$  is the sweep angle of the leading edge. The most important advantage of this theory is that all the nonlinear terms can be obtained using the potential flow theory. In practice, it has been proven that Equation (1) is simple and reliable. However, it can only be used to calculate the total lift and it cannot give a distribution of the vortex-lift unless the distribution of the leading edge suction force is calculated based on the calculation of finite basic solution which is not within the limits of discussion in this paper. For the simple estimation of the distribution of the vortex-lift and the center of pressure, we assume, as shown in Figure 1, that the vortex-lift on the inner side wing  $LE_{in}$  is equal to the vortex-lift of a single wing when it is considered to be the inner side wing. In other words, it is assumed that the "leading edge suction analogy" is not only applicable to the entire



wing but also suitable for each inner side wing sections.  
Therefore:

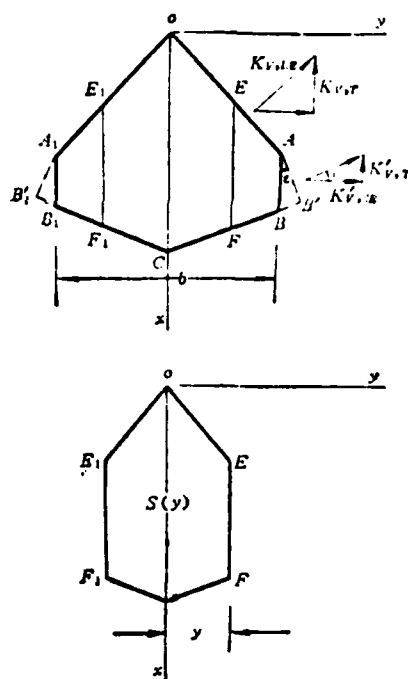
$$C_{l_{v, i, k}}(y) = C'_{l_{v, i, k}}(y) S'(y) / S_w \quad (2)$$

$$C'_{l_{v, i, k}}(y) = K'_{v, i, k}(y) \sin^2 \alpha \cos \alpha / \cos \Lambda \quad (3)$$

$$K'_{v, i, k}(y) = K'_v(y) \left( 1 - \frac{K'_v(y)}{\pi A'(y)} \right) \quad (4)$$

where all the values with "i" correspond to the inner side wing  $E_1 O E$  and  $S'(y)$  and  $S_w$  are the area of the inner side wing and that of the entire wing surface, respectively.

Figure 1. Schematic diagrams of the geometric relations and the calculation of the side edge vortex-lift.



In order to calculate the side edge vortex lift, it can be assumed further that the side edges  $AB$  and  $A_1 B_1$  extend outward at an angle  $\epsilon$  and the side edges  $AB$  and  $A_1 B_1$  become a part of the front edge. Using the "suction analogy" for the entire wing and

the inner side wing separately, the total propulsion and the propulsive force of the inner side wing can be determined. When  $\epsilon$  approaches zero, the side edge vortex lift can be obtained (see Figure 1).

$$C_{L_{V,SE}} = K_{V,SE} \sin^2 \alpha \cos \alpha \quad (5)$$

$$K_{V,SE} = \lim_{\epsilon \rightarrow 0} (K_{V,r} / \tan \epsilon)_{A \rightarrow A_1, S_1} \quad (6)$$

In addition, based on the definition of the distribution of the vortex lift

$$C_{L_{V,LE}}(y) = \frac{2}{S_w} \int_0^y c(y) c_{lv}(y) dy \quad (7)$$

where  $c(y)$  is the partial string length and  $c_{lv}(y)$  is the cross-sectional vortex lift coefficient. Substituting Equations (2) and (3) into the above, we get

$$c(y) c_{lv}(y) = \frac{1}{2} \frac{d}{dy} [K'_{V,r}(y) S'(y) / \cos \Lambda] \sin^2 \alpha \cos \alpha \quad (8)$$

Substituting into Equations (5) and (6) to obtain the side edge vortex lift, we get

$$C_{L_{V,SE}} = \lim_{\epsilon \rightarrow 0} \left\{ -\frac{1}{S} \int_{b/2}^{\frac{b}{2} + c_t \epsilon} \frac{d}{dy} [K'_{V,r}(y) S'(y) / \tan \epsilon] dy \sin \alpha \cos \alpha \right\} \quad (9)$$

or

$$C_{L_{V,SE}} = \left[ \frac{dK'_{V,r}}{d\epsilon} + \frac{K'_{V,r}}{S_w} \frac{dS'}{d\epsilon} \right]_{\epsilon=0} \sin^2 \alpha \cos \alpha \quad (10)$$

where  $b$  is the extending length of the wing and  $c_t$  is string length of the string sandwiched by the wing. Equation (10) was derived in [2]. Similarly, the centers of pressure of the vortex lifts at the front and side edges are

$$\frac{x_{V,LE}}{c_t} = \frac{\cos \Lambda}{S_w c_t K_{V,r}} \int_0^{b/2} x_{LE} \frac{d}{dy} [K'_r(y) S'(y) / \cos \Lambda] dy \quad (11)$$

and

$$\frac{x_{V,SE}}{c_t} = \frac{1}{S_w c_t K_{V,SE}} \lim_{\epsilon \rightarrow 0} \int_{b/2}^{\frac{b}{2} + c_t \epsilon} x'_{LE} \frac{d}{dy} [K'_r(y) S'(y) / \tan \epsilon] dy \quad (12)$$

respectively. Where  $c$  is the string length of the wing root;  $x_{f,e}$  is the string distance of the front edge measured from the apex of the wing;  $x'_{f,e} = x - x_{f,e}$  is the distance in the string direction measured from the apex of the side edge. Equations (9), (10), (11) and (12) are the general expressions of the vortex lift of the side edge and the center of pressure. From these we can see that they are functions of the potential flow lift force and the geometric shape of the wing.

As for a slender wing, on the basis of the theory on slender bodies by Jones, there are relations such as  $K_p = \frac{\pi}{2} A$ ,  $K_{v,e} = \frac{\pi}{4} A$ . Substituting them into Equation (8), we get

$$c(y)c_{lv}(y) = \pi y / \cos \Lambda \sin^2 \alpha \cos \alpha \quad (13)$$

From the above equation, we can see that the vortex lift distribution is a linear distribution within the limits of the theory for slender bodies which agrees with the conical flow assumption. Figure 2 shows the comparison between the cross-sectional vortex lift and the vortex lift on the inner side wing derived based on the assumptions used in this work and those reported in [2]. It demonstrates that the two are extremely close.

By substituting  $K_p$  and  $K_{v,e}$  into Equations (9) or (10), we get

$$C_{L_{v,se}} = \pi A \left( \frac{c_r}{b} \right) \sin^2 \alpha \cos \alpha$$

or

$$C_{L_{v,se}} = 4 \left( \frac{c_r}{b} \right) \frac{K_p^2}{\pi A} \sin^2 \alpha \cos \alpha \quad (14)$$

Although Equation (14) is obtained under the assumption of the slender body theory, even better results can be obtained if more accurate values of  $K_p$  can be determined. Based on the above equation, for a rectangular wing, we have  $K_{v,se} = \pi$  when the string extension is extremely small which is in agreement with Lamar [4].

Figure 3 is a comparison of the results obtained using Equation (14) with those obtained using the methods of Lamar [4] and Purvis [2] correspondingly. During the calculation, we took  $K_p = \frac{2\pi A}{\sqrt{A^2 + 4} + 2}$ . From this figure, we can see that the results of this work coincide with those of Lamar. The results obtained by Purvis are slightly higher.

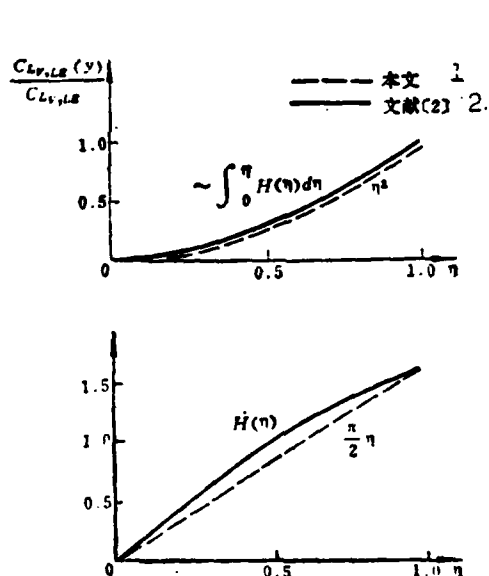


Figure 2. The distribution of the vortex lift: A comparison of this work and [2].  $H(\eta)$ : Equation (28) in reference [2]

Key: 1--this work; 2--reference [2]; 3--reference [4]; 4--Equation (52) of reference [2]; 5--this work and reference [4]

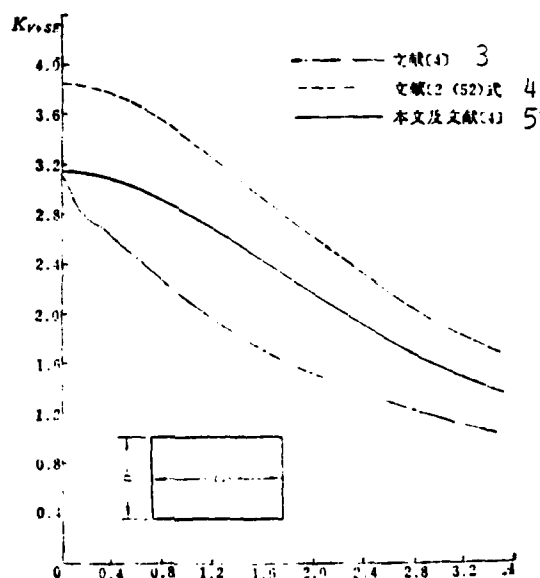


Figure 3. Comparison of  $K_{v,SP}$  for a rectangular wing

When substituting  $K_{v,LE}$  and  $K_{v,SE}$  into Equations (11) and (12) respectively, we get

$$\frac{x_{v,LE}}{c_r} = \frac{2}{3} \quad (\text{for triangular wing}) \quad (15)$$

$$\frac{x_{v,SE}}{c'_r} = \frac{2}{3} \quad (\text{for trapezoidal wing}) \quad (16)$$

$$\frac{x'_{v,SE}}{c_r} = \frac{1}{2} \quad (17)$$

where  $c'_r$  is the corresponding root string length at the leading edge of the trapezoidal wing,  $c'_r = \frac{b}{2} \tan \Lambda$ . From Equations (15), (16) and (17), we can see that the front fringe vortex lift and the pressure center of the side fringe obtained within the theoretical limits of the slender body theory are in agreement with those obtained by other workers. In the meantime, we also discovered that the centers of pressure of the leading edge vortex lift and the side edge vortex lift for a trapezoidal wing can be obtained separately, thus providing the theoretical basis for the following empirical correction equations.

## II. EMPIRICAL CORRECTIONS

Experimental results indicate that the "suction analogy" theory is only applicable within a range of ratio between the attack angle and string expansion. In order to extend the applicable range of that theory and to raise its accuracy, there have been many researchers who introduced various empirical or semi-empirical correction factors. For example, in [5], the correction factor  $K_{v,LE}$  for the front edge vortex lift for triangular wings and the side edge vortex lift optimization factor  $\bar{K}_{v,SE}$  in [6] are among them. This paper also introduces two correction equations as follows:

1. Center of pressure correction: From Equation (15) we know that under the conical flow assumption the center of pressure

of the front edge should be located at the 2/3 root string position. However, in reality, the strength of the vortex is not totally distributed conically especially near the rear fringe. In addition, when the attack angle increases the core of the vortex moves towards the inner side of the wing. Based on the experimental data, there is the following relation for the center of pressure of the vortex lift for a triangular wing:

$$\frac{x_{v,l.s}}{c_r} = \frac{2}{3} - 0.3729/\text{tg } \Lambda \quad (18)$$

If we further consider the effect of the attack angle on the drifting of the center of pressure, we can further use the following step:

$$\frac{x_{v,l.s}}{c_r} = \frac{x_p}{c_r} - \left[ \left( \frac{x_p}{c_r} \right) - \left( \frac{2}{3} - 0.3729/\text{tg } \Lambda \right) \right] \sin(3.6 \alpha) \quad (19)$$

where  $\frac{x_p}{c_r}$  is the corresponding center of pressure of the potential flow. The above equation can be used when  $\alpha \leq 25^\circ$ .

2. Improvement of the vortex lift: Experimental results indicate that because of the added induction reaction of the leading edge vortex on the side edge and the latter half of the wing surface, the experimental value of the vortex lift for a sharp triangular wing is higher than that obtained based on the calculation. Reference [7] gave a correction factor

$$k_v = 1.77 \left\{ 1 - \sin \frac{\pi \lambda}{2} \right\} \sin \frac{\pi \lambda}{2} + 1 \quad (20)$$

to express this type of constructive interference. Considering the effect of the glancing angle of the rear trailing edge, the final correction of the above equation becomes

$$k_v = \left\{ 1.77 \left( 1 - \sin \frac{\pi \lambda'}{2} \right) \sin \frac{\pi \lambda'}{2} + 1 \right\} \frac{\lambda'}{\lambda} \quad (21)$$

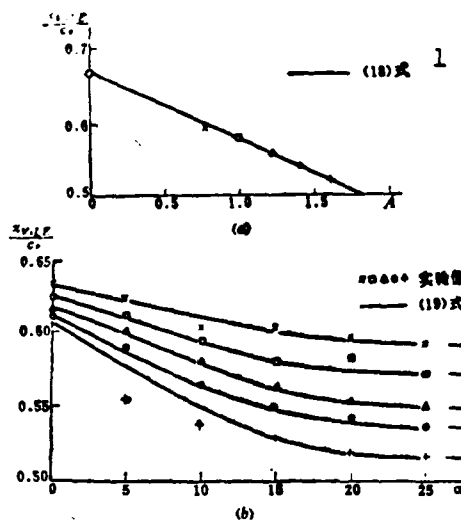


Figure 4. The variation of the center of pressure of vortex lift for triangular wings with string expansion ratio and attack angle

Key: 1--Equation (18); 2--experimental values; 3--Equation (19)

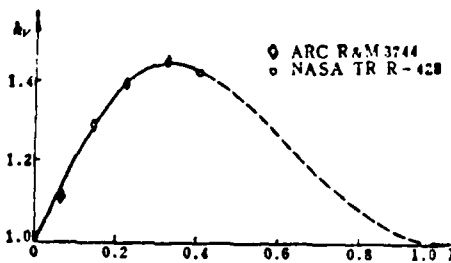


Figure 5. The improvement of the vortex lift for sharply carved triangular wings [7]

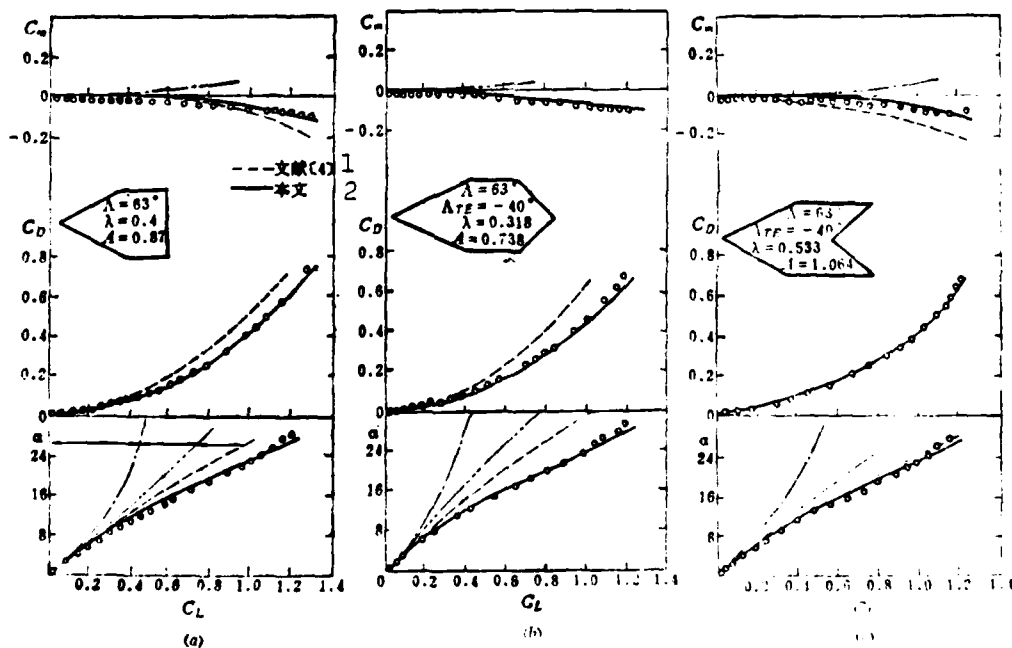


Figure 6. The comparison of the aerodynamic characteristics of a series of sharply carved trapezoidal wings

Key: 1--Reference [4]; 2--this work

where  $\lambda$  is the sharpness ratio  $\lambda = \frac{c_i}{c_r}$ ,  $\lambda'$  and  $\lambda'$  is the sharpness ratio of the basic sharp triangular wing,  $\lambda' = \frac{c_i}{c_r + b \tan \Lambda}$ .

The above mentioned Equations (19) and (20) are shown in Figures 4 and 5 respectively.

In summary, we can conclude based on the above discussion that for a trapezoidal wing the total vortex lift and the center of pressure can be expressed in a unified manner as

$$C_{L_v} = K_{v, tot} \sin^2 \alpha \cos \alpha \quad (22)$$

$$K_{v, tot} = k_v [K_{v, LE}^2 K_{v, T} / \cos \Lambda + K_{v, SE}] \quad (23)$$

$$\left(\frac{x}{c_r}\right)_v = k_v \left\{ K_{v, LE}^2 K_{v, T} / \cos \Lambda \left(\frac{x_{v, LE}}{c_r'}\right) \left(\frac{c_r'}{c_r}\right) + K_{v, SE} \left(\frac{x_{v, SE}}{c_r}\right) \right\} / K_{v, tot} \quad (24)$$

Key: 1--rear surface center

where rear surface center represents the face center of the wing area with the exception of the front fringe triangular area. Based on Equation (17), the center of pressure of the side edge vortex lift is located near the center of the side edge. But after considering the effect of the glancing angle of the trailing edge, it can be approximately assumed that the center of pressure of the side edge is located near the face of the rear wing surface.

### III. CONCLUSIONS AND DISCUSSION

The results obtained using the above method on a series of trapezoidal wings indicate that this method agrees with the experimental results very well (see Figure 6).

The method used in this paper can be expected to be extended to the calculation of the vortex and the center of pressure of a combined body. It is also not difficult to apply this method in the situation that the leading edge has turns such as a side stripe wing.



From the Prandtl-Goethert similarity law, we can consider the effect of compressibility.

The equations in this paper indicate that it is possible to obtain an optimal match for the maximum vortex lift for various rear glacing angle, sharpness ratio and string expansion ratio. This would be beneficial to the design department for shape selection.

This paper has been highly supported by Professor Tung Ping Kang who also proof-read the manuscript. The author wishes to express his thanks here.

#### REFERENCES

- [1] Yee Hsieh Huan. "An easy method to estimate the nonlinear vortex lift for wings with small string expansion ratio of any arbitrary planar shape". The Science and Technology University of China (Studying Mechanics) vol. 4, 1976.
- [2] Purvis, J. W. Analytical Prediction of Vortex Lift AIAA Paper 79-0363, 1979.
- [3] Polhamus, E. C. NASA TND-3767, 1966.
- [4] Lamar, J. E. NASA TRR-428.1974, 10.
- [5] Michael, R. M., Nielsen, J. N. NASA CR-2473, 1975.
- [6] Lamar, J. E. NASA SP-347.1975,3.
- [7] Huang Tung Lin. The method to calculate the longitudinal aerodynamic characteristics with large attack angle and total elasticity. Internal Report, the Science and Technology University of China, 1976, 12.

#### Abstract

This paper presents a simplified approximate analytical method for predicting vortex-lift and centre of pressure on the slender wing at high angle of attack, and proposes two empirical correlations as well. In comparison with other methods and experimental data, this method provides good accuracy and suits for preliminary aerodynamic design.

# A PENALTY FUNCTION METHOD FOR THE STRUCTURAL OPTIMUM DESIGN WITH AEROELASTIC CONSTRAINTS

Wang Xianxiu  
(Aerodynamic Research and Development Center of China)

## ABSTRACT

In this paper an interior penalty function method is used to obtain the minimum weight of a wing structure under the constraints of flutter, strength and minimum gage. In the paper three unconstrained optimization methods, viz., the steepest descent method, the DFP variable metric algorithm and the BFGS variable metric algorithm, are compared with one another. The quadratic interpolation method with the constraints approximated by quadratic polynomials is used to carry out the one-dimensional search. The convergent criterions used in the interior penalty function method are given. It also discusses several ways to reduce the computer time.

The results of the calculations indicate that the penalty function method is an effective method for the optimization of complicated structural design with aeroelastic constraints.

## I. INTRODUCTION

In the design of an aerospace vehicle, it is of practical importance to consider the aeroelastic constraints (mainly the velocity at which the structure begins to flutter) and strength constraints in order to reduce the weight of the structure. However, there are many difficulties involved in solving this problem. This is because the analysis of the aeroelastic properties of the structure is not only related to the structural dynamics but also to the unsteady aerodynamics which is even more complicated than the usual structural analysis. The traditional way is to choose the structural plan empirically and the aeroelastic analysis is

only for safety purposes and cannot be used as the design calculation method to select the optimal plan. In the last 20 years, due to the rapid development in electronic computers and the technology in the optimization of the structural design, it is then possible to solve the problem of the optimization of structural design which takes aeroelastic constraints into consideration. Currently, the analytical methods are divided into the optimization principle method and the mathematical method. This paper adopts the nonlinear mathematical penalty function method (also called the SUMT method) [1]. On the basis of [1] and through the experience of the use of the penalty function method numerically in the actual calculation and verification of aeroelastic constraints, we are presenting several improvement procedures in the actual realization of using the penalty function in the optimization of structural design with constraints in order to save more time in the calculation. The penalty function method transforms a multi-constraint problem into a series of easy to process unconstrained problems. It has the advantages of high adaptability, quickness, high reliability and high quality in the design optimization.

## II. THE TREATMENT OF MULTI-CONSTRAINTS

The multi-constraint problem of the optimization of flutter and strength can be changed into unconstrained problems through the use of the interior penalty method. The interior penalty function is

$$P(\vec{C}, r_k) = W G(\vec{C}) + r_k \sum_{i=1}^3 \ln g_i(\vec{C}) \quad (1)$$

where  $W G(\vec{C})$  is the target function which is the weight of the structure,  $g_i(\vec{C})$  represents the three non-parametric form constraints which the design variable must satisfy,  $r_k$  is called the penalty factors,  $k = 1, 2, \dots, N$ ,  $r_{k+1} = r_k / \Delta r$ , and  $r_k > r_{k+1} > \dots > r_N \approx 0$ .

To use this series of  $r_k$  values to determine  $\min P(\bar{C}, r_k)$  is to carry out a series of unconstrained optimization analyses. The advantage of using the interior penalty function method is that all the intermediate designs given in the process of searching for the optimal solution are all workable. The search can be stopped at any time and an adoptable design can always be obtained.

The three non-parametric (no coordinate systems) constraint functions are:

$$g_1(\bar{C}) = 1 - \frac{V_{lim}}{V_f} \geq 0 \quad (2)$$

which represents the constraint of flutter.  $V_{lim}$  is the given velocity value,  $V_f$  is the velocity at a given altitude the structure begins to flutter which can be given automatically by the computer by solving the flutter characteristics equation

$$g_2(\bar{C}) = A / \iint \left( 1 - \frac{\sigma(x, y)}{\sigma_{cr}} \right)^{-1} dx dy \quad (3)$$

which expresses the constraint of strength.  $A$  is the area of the wing.  $\sigma_{cr}$  is the allowable stress of the material.  $\sigma(x, y)$  is the Von Mises stress produced under the designed load condition at  $(x, y)$  on the wing

$$g_3(\bar{C}) = A / \iint \left( 1 - \frac{t_{min}}{t(x, y)} \right)^{-1} dx dy \quad (4)$$

which represents the constraint of minimum gage.  $t(x, y)$  is the thickness distribution of the thin plate and  $t_{min}$  is the given minimum value of the thin plate.

On the basis of the size of the computer (DJS-8), the model for structural analysis is selected either using upper and lower thin plated to form an all-directional laminated plate or solid thin plates with the front and rear fringes sharply carved as shown in Figure 1. The relation between the design variables  $\bar{C}$  and the thickness distribution  $t(x, y)$  is

(5)

$$t(x, y) = t_{min} + \sum_{m=0}^3 \sum_{n=1}^3 C_{3m,n} \tilde{x}^m \tilde{y}^n$$

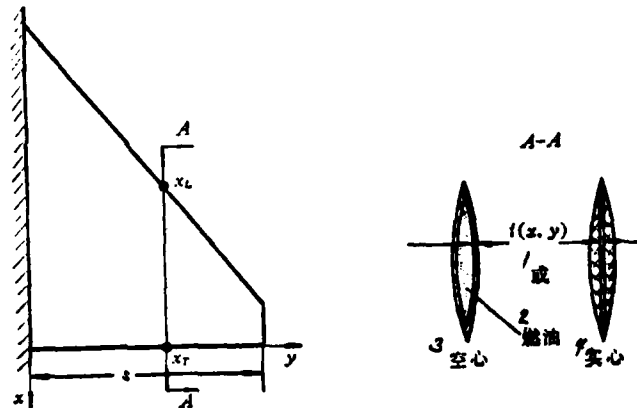
or

$$t(x, y) = t_{min} + \sum_{m=0}^3 \sum_{n=1}^3 C_{3m,n} \tilde{x}^m \tilde{y}^n (1 - \tilde{x}^2) \quad (6)$$

Equation (6) has been presented in [1]. In Equations (5) and (6)  $\tilde{x} = (x_L - 2x + x_T) / (x_L - x_T)$ ,  $\tilde{y} = 1 - y / s$ .  $x_L, x_T, s$  are shown in Figure 1. Of course, when  $y = S$ , there is  $t = t_{min}$ . Furthermore, when  $x = x_L$  or  $x_T$ , Equation (6) also makes  $t = t_{min}$ . Thus, the numbers of the design variable  $\bar{c} = \{C_{3m,n}\}$  are 12 and 6 respectively.

Figure 1. The model used in the calculation of wing structure

Key: 1--or; 2--fuel; 3--hollow; 4--solid;



In Equation (1), the  $r_1$  initial value of  $r_k$  should be selected so that the value of the penalty term

$$PF(\bar{c}_i^{(0)}) = r_1 \sum_{i=1}^3 b_i g_i^{-1}(\bar{c}_i^{(0)}) \quad (7)$$

at the initial point  $\bar{c}_i^{(0)}$  is close to that of the target function  $WG(\bar{c}_i^{(0)})$ . If the value of  $r_1$  is too large, then the entire calculation time is too long. If it is too small, then the property of P is not good and it becomes difficult to find the true minimum. Generally,  $\Delta r$  should be chosen so that 4~6 times of unconstrained optimization analyses can be carried out. If the

number of analyses is too small, it may show some false convergence. The  $b_1$  in Equation (1) is a constraint factor. Its given value can be used to control the relative weight of the constraints.

### III. UNCONSTRAINED OPTIMIZATION AND ONE-DIMENSIONAL SEARCH

In the  $k$ -th attempt of the unconstrained search cycles, the motion from  $\bar{c}_k^{(n)}$  to  $\bar{c}_k^{(n+1)}$  is given by the following equation

$$\bar{c}_k^{(n+1)} = \bar{c}_k^{(n)} + S^{(n)} \bar{z}^{(n)} \quad (8)$$

In this paper, three methods to determine  $\bar{z}^{(n)}$  are compared:

- (1) the steepest descent method. Taking the negative gradient direction of the function as the search direction.
- (2) DFP variable metric algorithm [3]
- (3) BFGS variable metric algorithm [3].

All three methods require the calculation of the gradient of  $P=WG+PF$ . Because  $WG(\bar{c})$  and  $\bar{c}$  have a linear relation,  $\partial WG / \partial \bar{c}$  can be expressed analytically. The partial derivatives of  $PF$  with respect to the design variables are calculated using the finite difference quotient method. The increment of the difference quotient is given in advance. Its magnitude should be proper so that half of the significant figures are lost in the difference quotient calculation.

Figure 2 shows the variations of the penalty function  $P$ , target function  $WG$  and penalty term  $PF$  in the unconstrained optimization analysis for  $r=1.33$ . It can be seen that the steepest descent method did not descend in the steepest way. Its approach to the minimum of the target function is in a jigsaw shape with a slow convergence process. The DFP variable metric algorithm and especially the BFGS variable metric algorithm are all very

effective. In general,  $N_c$  design variables only require  $N_c$  number of searches. Because some rounding-off error exists in the calculation, it may appear very infrequently that it does not totally converge after  $N_c$  searches. At this time, we can renew the search in the steepest descent direction. Figure 3 compares the structural weights and the shield thickness distributions of the final designs obtained using these three methods.

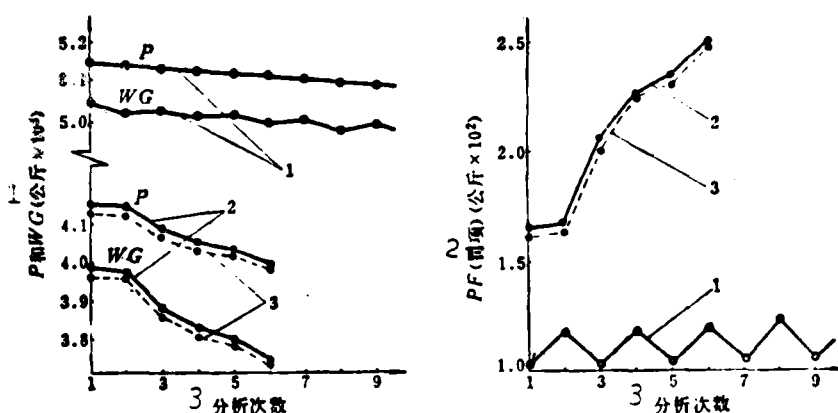


Figure 2. The comparison of the three unconstrained optimization methods.

1--steepest descent method 2--DFP method 3--BFGS method  
Key: 1--P and WG ( $\text{Kg} \times 10^3$ ); 2--PF (penalty term) ( $\text{kg} \times 10^2$ );  
3--number of analyses

The  $S^{(n)}$  in Equation (8) can be obtained from a one-dimensional search. In order to determine  $S^{(n)}$ , we let

$$\min P(S^{(n)}) = \min P(\bar{C}_1^{(n)} + S^{(n)} \bar{Z}^{(n)}) \quad (9)$$

From Figure 4, we can see that when the step length  $S=S_1$ , the constraint  $g_1=0$  (in the figure  $g_3=0$ ) and the value of the function  $P(S_1)$  is  $\infty$ . Furthermore, the variation of the derivative near the minimum is very large. It is not possible to use a polynomial of  $S$  to approach the function  $P$ . But the variation of the constraint function  $g_1(s)$  with  $S$  is very smooth; it can be easily

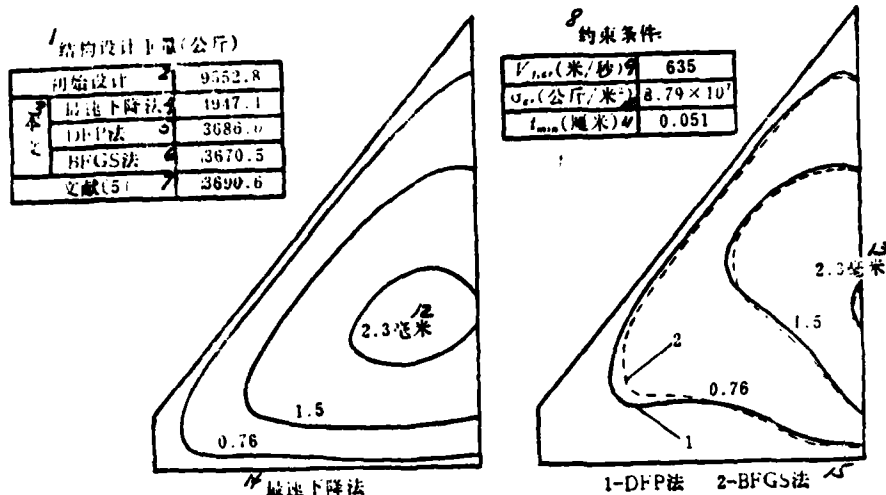
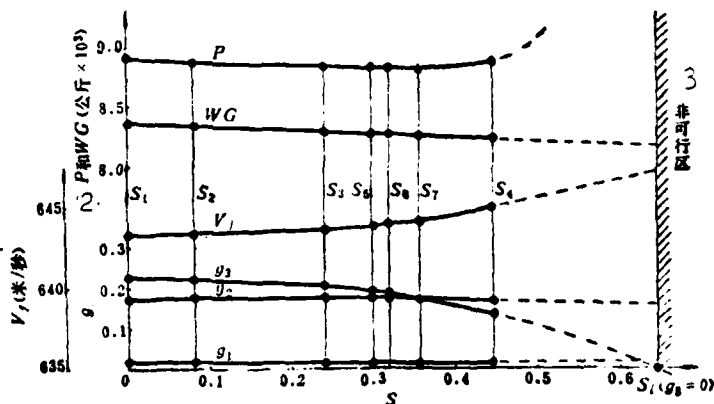


Figure 3. The shield thickness distributions obtained from the three unconstrained optimization methods

Key: 1--weight of the structural design (kg); 2--initial design; 3--this work; 4--steepest descent method; 5--DFP method; 6--BFGS method; 7--reference [5]; 8--constraints; 9--(m/sec); 10--(kg/m<sup>2</sup>); 11--(cm); 12--13--mm; 14--steepest descent method; 15--1-DFP method; 2-BFGS method

Figure 4. The process of one-dimensional search carried out by using the quadratic interpolation method.

Key: 1-- $V_f$  (m/sec)  
2-- $P^f$  and  $WG$  (kg $\times 10^3$ )  
3--unfeasible zone



approximated using a polynomial. By adding the linear analytical expression of the target function to it, we can use that expression to approximate the penalty function  $P(S)$  in order to save lots of time spent in the precise calculation of  $g_1$ . In this paper we used quadratic polynomials of  $S$  to approximate constraints  $g_2$ ,  $g_3$  and the flutter velocity  $V_{f0}$  which forms  $g_1$ .



#### IV. CONVERGENT CRITERIONS

The convergent criterions of the iterations are given under three conditions:

1. In one-dimensional searches, if  $S_j$  happens to satisfy both equations which follow when the search is terminated:

$$\left| \frac{dP_a(S_j)}{dS} \right| \leq \epsilon_1, \quad \left| \frac{dP(S_1)}{dS} \right| \quad (10)$$

$$|g_{1a}(S_j) - g_1(S_j)| \leq \epsilon_2, \quad (11)$$

$S_j$  is taken as the step length  $S^{(n)}$ . In the equations  $S_1=0$  and the subscript a represents the approximate value obtained using the polynomial form in the calculation. In this paper, we took  $\epsilon_1=0.2$ ,  $\epsilon_2=0.02$ .

Equation (11) is an auxiliary condition. In this paper we only considered flutter.

2. Unconstrained optimization analysis: In the k-th unconstrained optimization analysis, the convergence is judged by the following four conditions:

(1) vector gradient criterion: when the design variable  $\bar{c}_k^{(n)}$  satisfies

$$\|\nabla P(\bar{c}_k^{(n)}, r_k)\| \leq \epsilon_3 \|\nabla P(\bar{c}_k^{(n)}, r_k)\| \quad (12)$$

this unconstrained analysis is terminated. We took  $\epsilon_3=0.05$  in this paper.

(2) quadratic convergence criterion: if when  $l \geq N_c(N_c)$  ( $N_c$  is the number of design variables) Equation (12) is still not satisfied, then we calculate the quadratic convergence

$$Q = \frac{1}{2} \{ \nabla P(\bar{c}_k^{(n)}, r_k) \} [H^{(n)}] \{ \nabla P(\bar{c}_k^{(n)}, r_k) \} / P(\bar{c}_k^{(n)}, r_k)$$

where  $[H^{(n)}]$  is the matrix  $H^{(n)}$  in the variable metric algorithm. When  $0 < Q < \epsilon_4$ , (13)

we can consider that it is convergent. If  $Q < 0$  then it indicates that  $[H^{(n)}]$  is not orthogonal and we should renew the searches using the steepest descent method. If  $Q > \epsilon_4$ , then the DFP or the BFGS methods can still be used in the iterations. In this paper, we use  $\epsilon_4 = 0.02$ .

(3) Constraint criterion: when  $Q > \epsilon_4$ , if we continue going forward by a little step  $\Delta S$  in the steepest descent direction either the constraint is broken or even the constraint is not broken the function  $P$  does not decrease any further. In that case, this point can be used as the minimum of this unconstrained analysis and the search can be terminated.  $\Delta S$  is generally taken as  $0.5 \times 10^{-3} \sim 0.5 \times 10^{-4}$ .

(4) Limitation of the numbers of directional search. In a one-dimensional unconstrained optimization analysis of the accumulated number of the directional searches  $N_i \geq N_0 + 3$ , then we use this point as the optimal point to terminate this analysis.

### 3. Convergence criterion of the entire constraint problem.

In [4], the absolute upper and lower limits of the true minimum value of the target function  $WG(\bar{C}^*)$  in the penalty function method using the corresponding coupling equation of the minimization problem as

$$WG(\bar{C}_i^*) - PF_r \leq WG(\bar{C}^*) \leq WG(\bar{C}_i^*) \quad (14)$$

and

$$PF_r = r_r \sum_{i=1}^3 b_i g_i'(\bar{C}_i^*) \quad (15)$$

$C_k^*$  is the minimum point obtained from the unconstrained optimization analysis with  $r=r_k$ . From Figure 5 in this paper, it shows that Equation (14) is reliable. In the figure Equation (14) is not satisfied for the steepest descent method. This is because that in the calculation the number of iterations was used to control the convergence and a false convergence was produced. We are going to transform Equation (14) in this paper and define a

convergence determination quantity  $C_F$

$$\frac{WG(\bar{c}_i^*) - WG(\bar{c}^*)}{P(\bar{c}_i^*, r_i)} \leq \frac{PF_i}{P(\bar{c}_i^*, r_i)} = C_F \quad (16)$$

when

$$C_F \leq \epsilon_1 \quad (17)$$

$WG(\bar{c}_i^*)$  has already been approaching  $WG(\bar{c}^*)$  and the optimization process for the entire constraint problem can be terminated. In this paper,  $\epsilon_1 = 0.02$ .

## V. WAYS TO REDUCE COMPUTER TIME

When the DFP or BFGS variable metric algorithm is used and the first order derivatives are calculated from the finite difference quotient method, the required calculation can be estimated using the following equation:

$$T_{vm} = KN_g N_r N_s (2N_s + N_s + 1) t_p / N_s \quad (18)$$

In the equation  $K$  is an empirical coefficient determined by the values of  $\epsilon_i$  ( $i = 1, 2, \dots, 5$ ) in the convergent criterions. In this paper, it is approximately 1.15.  $N_{gs}$  is the total number of the constraints.  $N_g$  is the number of constraints considered in the calculation.  $N_r$  is the number of the penalty factors.  $N_0$  is the average number of function calculation in the one-dimensional search.  $t_p$  is the time required to calculate the function  $P$  once. This equation shows several ways to reduce the calculation time:

(1) To use extrapolation method to reduce the value of  $N_r$ . In the actual calculation we can see that if we plot the minimum point of constraint  $\bar{c}^*(r)$  as a function of  $r$ , the curve is very smooth as shown in Figure 6. Therefore, after obtaining  $\bar{c}^*(r_1)$  and  $\bar{c}^*(r_2)$  by carrying out unconstrained optimization analyses with respect to  $r_1$  and  $r_2$ , it is possible to obtain a better "initial point" using a proper extrapolation equation directly for  $r_{N_r} \approx 0$  and then carry out another unconstrained optimization analysis. Thus the value of  $N_r$  drops from the usual 4~6 times to

three times. The calculation load can be reduced by more than 20%. From numerical examples, this paper gives the following extrapolation equation:

$$\bar{c}^*(r) = \bar{c}^*(r_1) - \frac{\bar{c}^*(r_1) - \bar{c}^*(r_2)}{r_1^2 - r_2^2} (r_1^2 - r^2) \quad (19)$$

$\beta = 0.4$ . The extrapolation curves approximate very well as shown in Figure 6. Even if there are some differences, it is still all right because it is merely an "initial point" used in the iterative analysis. If the extrapolation point does not satisfy the constraints, we can increase  $\beta$  to 0.1 and then extrapolate again using Equation (19) until the constraints are satisfied. If when  $\beta = 1$  and the feasible extrapolation point can still not be found, then we should use the value of  $r_3$  to carry out a new series of unconstrained optimization analyses.

(2) To choose the proper number of design variables  $N_c$ . The increase of  $N_c$  can improve the optimized design as shown in Figure 7. But it also greatly increases the calculation time. When  $N_c$  changes from 6 to 12, the weight of the structure only decreases by 2.5% but the calculation time increases by 2.4 times. For that we adopted the method which gradual increases of design variables to reduce the calculation time. That is to use the optimal point with six variables as the initial point for the final unconstrained optimization analysis when the number of design variables is 12. Thus, the calculation time can be saved by 46%.

In addition, the use of an effective one-dimensional search method to reduce the value of  $N_0$  and the use of quadratic polynomials of the design variable  $\vec{C}$  to partially approximate  $g_1(\vec{C})$  and then to provide the approximate vector gradient of the penalty function and the second order derivatives in matrix form analytically can further reduce calculation time.

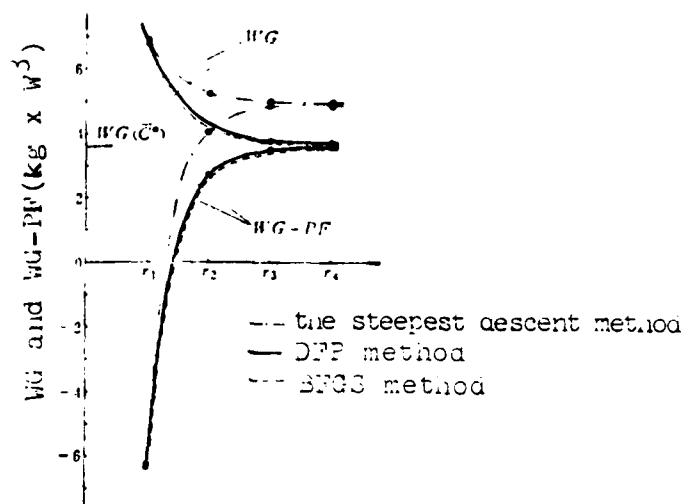


Figure 5. The Upper and Lower Limits of the Actual Minimum Value  $WG(C^*)$  of the Target Function

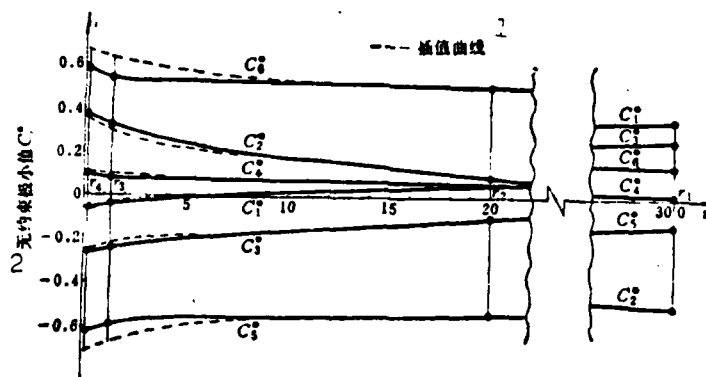


Figure 6. The relation between the unconstrained minimum value  $C^*$  with  $r$ .  
Key: 1--extrapolation curve; 2--unconstrained minimum value  $C_1^*$

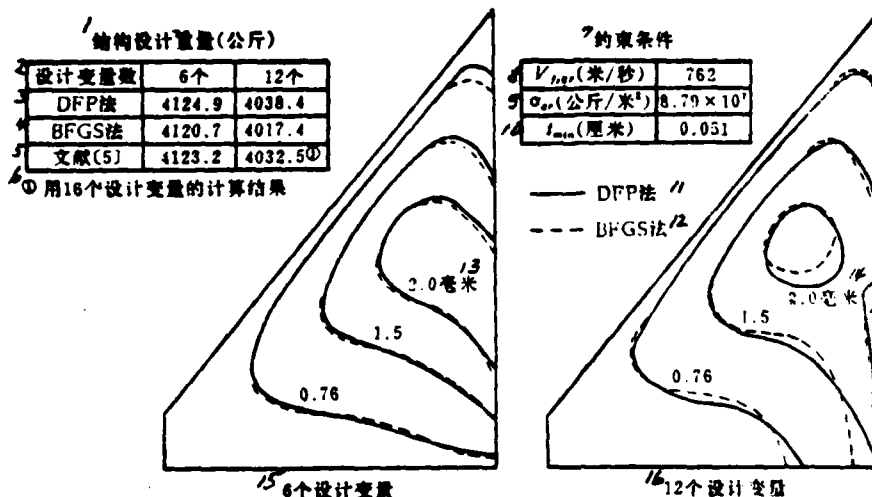


Figure 7. Shield thickness distributions of final designs obtained using various number of design variables.

Key: 1--weight of the structural design (kg); 2--number of design variables; 3--DFP method; 4--BFGS method; 5--reference [5]; 6--calculated results with 16 design variables; 7--constraints; 8--(m/sec); 9--(kg/m<sup>2</sup>); 10--(cm); 11--DFP method; 12--BFGS method; 13--mm; 14--mm; 15--6 design variables; 16--12 design variables

## VI. CONCLUDING REMARKS

The computation programming has been compiled using the FORTRAN language on the DJS-8 computer in this work. This program carried out an optimization calculation for a titanium alloy supersonic plane wing structure [5] with respect to flutter (or strength). The major calculated results have already been shown in Figures 2, 3 and 7, respectively. Figure 8 also shows the calculated based on six design variables considering flutter alone, strength alone and the combination of flutter and strength (all with minimum gage constraint). We can infer that the final structural designs are not quite the same.

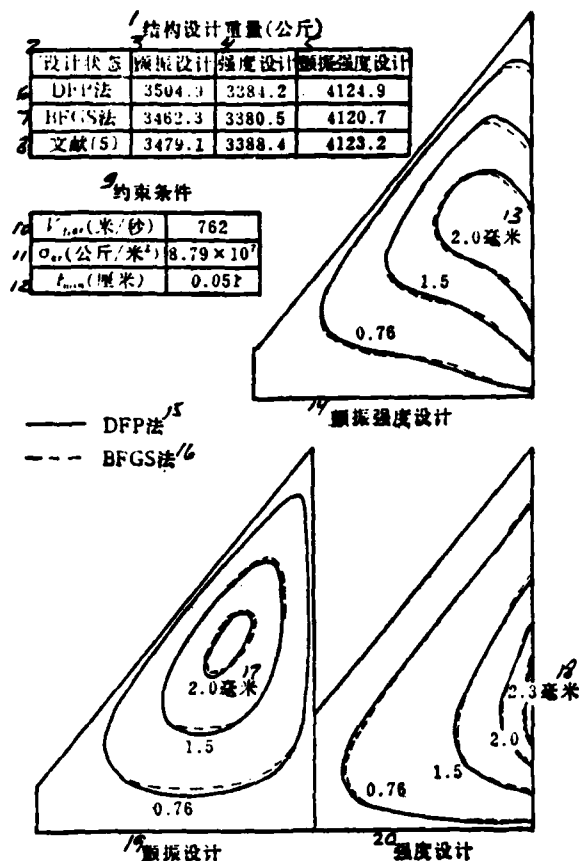


Figure 8. The distribution of shield thickness of the final designs obtained under three design conditions:  
 Key: 1--weight of structural design (kg); 2--design condition; 3--flutter design; 4--strength design; 5--flutter and strength design; 6--DFP method; 7--BFGS method; 8--reference [5]; 9--constraints; 10--m/sec; 11--kg/m<sup>2</sup>; 12--cm; 13--m; 14--flutter and strength design; 15--DFP method; 16--BFGS method; 17--mm; 18--mm; 19--flutter design; 20--strength design

For this type of structural design optimization problems with aeroelastic constraints, the use of the penalty function method is successful. It can significantly reduce the design weight of the wing structure and greatly improve the quality of the design. The method and program used in this work will be further examined and perfected in the actual design of aerospace vehicles.

#### REFERENCES

- [1] Stroud, W. J., Dexter, C. B. and Stein, M. "Automated Preliminary Design of Simplified Wing Structures to Satisfy Strength and Flutter Requirements", NASA TN D-6534.
- [2] Stein, M. and Sanders, J. L., Jr. "A Method for Deflection Analysis of Thin Low-Aspect-Ratio Wings", NASA TN 3640 June 1956.
- [3] Calculated Mathematics Special Topics from the Mathematic Department of Nanking University, "The Optimization Method", Science Publication, 1978.
- [4] Fiacco, A. V. and McCormick, G. P. "Nonlinear Programming, Sequential Unconstrained Minimization Techniques", John Wiley and Sons, Inc., 1968.
- [5] Aeroelastic Group of Institute No. 601: The Aeroelastic Analysis For a High Speed Destroying Attack Plane, Journal of Aerospace, Volume 1, 1978.

#### Abstract

In this paper an interior penalty function method is applied to minimize the weight of a wing structure under the constraints of flutter, strength and minimum gage. Three unconstrained optimization methods: steepest descent method, DFP variable metric algorithm and BFGS variable metric algorithm, are compared with each other. The quadratic interpolation method with the constraints approximated by quadratic polynomials is used in the one-dimensional search. Respective convergent criterions used in the interior penalty function are presented. Several ways to reduce computer time are pointed out and discussed here.



# AN AERONAUTICAL STRUCTURAL ANALYSIS SYSTEM FOR STATIC ANALYSIS(HAJIF-I)

*(The team for developing HAJIF-I*

*Penned by Feng Zhongyue)*

## Abstract

This aeronautical structural analysis system for static analysis(HAJIF-I) is the first large software system developed by the Chinese Aeronautical Establishment(CAE). By using multilevel substructure analysis and finite element displacement method, this system is suitable for various linear static analysis of aeronautical structures. The maximum capacity of the system is as follows, 3000 nodal DOF of each substructure, 99 substructures, 10 levels of substructures. The system provides some statements for automatic data generation, so the initial data necessary for computation can be generated automatically. There are also several special statements for structural analysis, thus enabling user to organize his own computation flow. The system offers two solvers for high order sparse matrix, i. e. a modified variable bandwidth method and a hyper-matrix method. One of these methods will be chosen by users according to computer capacity and structural characteristics. The system consists of a sequence of functional modules which are independent of each other, so it can be modified and extended easily. There are approximately 30,000 source statements in the system and most of them were written in FORTRAN IV. At the end of this paper, a user's specification for stress analysis of an aircraft is presented as an example to demonstrate that the system is easy to handle.

# AN AERONAUTICAL STRUCTURAL ANALYSIS SYSTEM FOR STATIC ANALYSIS (HAJIF-I)

## The Team for Developing HAJIF-I

Feng Zhongyue

### ABSTRACT

The aeronautical structural analysis system for static analysis is the largest software programming system ever developed by the aeronautical industry. This system uses the multilevel substructural analysis technique which is suitable for various linear static analysis of all types of aeronautical structures. It is capable of solving 99 substructures and the nodal point degree of freedom for each substructure is 3000. This system provides specific statements for automatic data generation and structural analysis. It has a stronger original data generation capability as well as the flexibility for the user to organize his own computation flow. The system offers two ways to solve the high order sparse matrix problems, viz., a modified variable bandwidth method and the hypermatrix method. The user can choose one of the two methods based on the characteristics of the structure and the capacity of the computer. The program organization adopts a two level module structure for each of modification and gradual expansion of the capacity of the system. The entire system contains approximately 30000 source statements and most of them were written in FORTRAN IV which can be easily transferred into different computers. Finally in this paper, we used the user manual for a particular airplane which used this system to perform a stress analysis as an example to indicate that this system is very convenient.

## 1. INTRODUCTION

The development of a general, flexible and large structural analysis computer program system is now imminent. Electronic computers were used to carry out structural analysis in our country in the late 50's. In the late 50's, the design department in the aeronautical industry used matrix displacement methods and matrix force methods to compile the program for the stress analysis of wing structures. In the early 60's, they used direct strength methods and the substructure analysis technique to compile programs to obtain the design and actually applied such results to the design of new airplanes. From the 70's on, because of the fast advance in the development of the finite element method and the computation technique, there have been many special and general computer programs being compiled by various researchers in the country for static structural analysis, dynamic analysis and optimization purposes. The magnitude of problem solving capability has exceeded ten thousand degrees of freedom. But due to the limitation of the hardware of the computer and the lack of emphasis on the software work, the development and advancement of computer programming system is always slower in our country as compared to foreign countries. It is the common feeling among many engineering technical people working on structural analysis and computation that we must concentrate our efforts to develop our own large and general structural analysis system as soon as possible based on the experience acquired over the past years so that it can provide us a flexible and effective tool in the development of new airplanes and in scientific research work.

In the late 70's, the aeronautic authority held meetings on the exchange of finite element study and the research on structural strength. After considering the developmental trend both home and abroad as well as the urgent needs from various fields, we believed that we had already had the basic conditions needed to develop a large and general structural analysis system. Therefore, the

Aeronautical Research Institute of China concentrated all the relevant technical personnel from four research institutions to form a development team. After checking the needs of various users in the country and studying the information on similar types of program systems abroad, this development team began the development of the static analysis part of the system on the basis of the conditions presently available in our country. It is named as the I model of the aeronautical structural system and an abbreviation HAJIF-I is adopted based on the spelling in Chinese.

## II. DESIGN CONCEPTS

From the survey of users, we found that it is necessary to improve the automation and flexibility of the programs developed recently in our country because of the limitations of computer capacity and operating system. Therefore, when we determined the emphases of our developmental work, we placed our attention on three areas which are the automatic formation of original data, the establishment of specific statements of structural analysis for the user and the efficient solution of high order sparse matrix problems. The purpose was to minimize to the extent possible the work load of data preparation by people and also to increase the efficiency and flexibility of the system. The actual design concepts are

1. Generality. A large program system must be able to be applicable to various types and sizes of structures. Therefore, this system adopted the multi-substructural analysis technique. Actually any large complicated structure of various shapes can be divided into substructures of the proper size. By putting these substructures together by different classes, it is possible to make the solution seeking process not too large for all the substructures of various levels so that it can be conveniently handled using the computer.

---

Received in October 1979

2. Flexibility. The system provides specific statements for the users in structure analysis. The words in these statements are formed by the abbreviations of the spelling in Chinese. The users can use these statements to realize the 15 fixed flow routes. Furthermore, they can write their particular computation process based on their needs.

3. Automation. In order to minimize the amount of labor involved in the preparation of initial data, the system provides specific statements to generate data. The users can use these statements to carry out an effective displacement under load, the division of the structural lattice and the formation of the nodal position.

4. High efficiency. In solving for high order sparse matrix, the system provides a modified variable bandwidth method and a hypermatrix method which are suitable for the third generation computers. The user can choose a suitable and efficient method based on structural characteristics and the computer to solve the problem.

5. Expansion capability and ease of modification. In the program organization area the system adopts a modular structure. Each module completes a particular function. They are all mutually independent. Therefore, when the system requires expansion or modification, it is only necessary to supplement with new modules or to modify relevant modules without changing the other modules. This enables the system to gradually develop further and continually improve.

6. Interruption and diagnosis capabilities. The system has the capability of interruption processing. It can obtain the solution in steps. After the occurrence of pre-arranged interruptions, it can be restarted. This is very important when the computation time is long and under the conditions that accidents may happen. The system must also have some diagnostic capability. On the basis of the characteristics of the error, it should either issue warnings or terminate the computation.

7. Ease of computer transfer. For the convenience of future transfer of computer, FORTRAN-IV was used in the compilation of the program for the most part with the exception of a few programs. By doing so, it is naturally unavoidable to suffer some losses in computation efficiency.

### III. FUNCTIONS

HAJIF-I can complete the stress and distortion analyses of various types of thin-wall structures and structure frames under external loads. As for the system itself, there is no limit to the magnitude of the problem it can handle. But because during its development the loading equipment only had 256K in internal memory and the average speed of double accuracy floating point calculation was less than ten thousand times an hour plus the stability time was short (about 3-4 hours), thus we limited the total number of degrees of freedom for each nodal point of every substructure to be less than 3000. The number of substructures is less than 99 and the level of substructure is less than 10. Considering that the system is going to be mainly used for thin wall structures, thus the degree of freedom for each nodal point is limited to six.

Based on the basic requirements of structural static analysis, the two methods in the system fix the 15 most commonly seen analysis flow routes using the specific statements for the user in structural analysis. The user only has to choose the proper statements in the source program based on his need. The control module will dispatch the corresponding functional module to sequentially execute the entire computation included by a statement. The modified variable bandwidth offers 11 fixed flow routes. The hypermatrix method offers four fixed flow routes and the details are shown in Table 1.

The element warehouse in the system can compute the strength matrix of an element and the effective nodal load of distributed

load and temperature. It can also calculate the nodal force of the element according to the nodal displacement, stress of a given inner point of an element and the residual strength. The element warehouse has 18 displacement coordinated types of elements for the users to choose from and details are shown in Table 2.

The material warehouse of this system contains seven types of material. They are LY12 aluminum alloy plates and preforms, high strength aluminum alloy LC4 plates and preforms, high strength steel 30CrMnSiA, super high strength steel 30 CrMnSiNi<sub>2</sub>A, and stainless 1 Cr18Ni9Ti.

#### IV. MECHANICAL PLAN

HAJIF-I adopted the finite displacement method to solve the static problem of elastic structures which is widely used both at home and abroad. The equilibrium relations of the structure can be expressed by a series of linear algebraic equations which can be written in the matrix form as

$$[K]\{\delta\} = \{P\} \quad (1)$$

The following is a brief introduction on the establishment of this series of equations and the methods of calculating stress analysis and the influencing coefficients.

TABLE 1. FIXED FLOW ROUTES

Sequence Number	Statement	NAME
		modified variable bandwidth method
1	JLFX01	assembly from stiffness matrix to trigonometric analysis
2	JLFX02	boundary stiffness matrix to trigonometric analysis
3	JLFX03	assembly from stiffness matrix to displacement substitution
4	JLFX04	assembly from stiffness matrix to stress calculation
5	JLFX05	assembly from stiffness matrix to influencing coefficient computation
6	JLFX06	superposition of boundary stiffness matrix to displacement substitution
7	JLFX07	superposition of boundary stiffness matrix to stress calculation
8	JLFX08	superposition of boundary stiffness matrix to influencing coefficient calculation



TABLE 1 (continued)

Sequence Number	Statement	NAME
9	JLFX09	displacement substitution
10	JLFX10	stress calculation
11	JLFX11	influencing coefficient calculation
12	JLFX51	assembly from substructural stiffness matrix to equivalent load
13	JLFX52	superposition of substructural boundary stiffness matrix to equivalent load
14	JLFX53	substitution from substructural displacement to stress calculation
15	JLFX54	complete static analysis flow process

TABLE 2. WAREHOUSE OF ELEMENTS

Number	Symbol for element	Name of element
1	G01	spatial variable cross-sectional pole element
2	G02	through symmetric surface pole element
3	L01	spatial equi-cross-sectional beam element
4	L02	planar equi-cross-sectional beam element
5	L03	planar three-point equi-cross-sectional beam element
6	L04	planar-two-point equi-cross-sectional transition beam element
7	L05	planar equi-cross-sectional oblique beam element
8	L06	planar equi-cross-sectional curved beam element
9	J01	trapezoidal shearing plate element
10	J02	through symmetrical surface trapezoidal shearing plate element
11	J03	general quadrilateral shearing plate element
12	J04	equi-planar general quadrilateral shearing plate element
13	M01	three-point triangular thin film element
14	M04	planar rectangular thin film element
15	M05	general quadrilateral thin film element
16	W02	rectangular curved plate element
17	Y02	linear stiffness element
18	Y04	body stiffness element

TABLE 2 (continued)

No. of nodal points	order of stiffness matrix
2	6
1	3
2	12
2	12
3	12
2	9
2	12
2	12
4	12
2	6
4	12
4	12
3	9
4	12
4	12
4	24

## 1. The assignment of degree of freedom

There are five types of structural nodal DOF in the ideal structural mechanical model:

- (1) internal degree of freedom of the substructure (I) which is the degrees of freedom of all the internal nodal points in the substructure
- (2) boundary degree of freedom of the substructure (B) which is the degree of freedom of all the nodal points on the boundary of the substructure
- (3) motion boundary degree of freedom (V) which is the degree of freedom when the distortion of a nodal point in the direction of a degree of freedom is a given value (it can be zero)
- (4) symmetric surface degree of freedom (S) which is the degree of freedom of the nodal points on the symmetric surface of the structure. It is again divided into symmetric (d) and asymmetric (f) types
- (5) permanent sustaining degree of freedom (K) which is the corresponding degree of freedom provided by the constraints needed to eliminate solid body motion of the structure.

## 2. Coordinate system

For the convenience of problem description, this system offers five orthogonal coordinate systems. They are mutually related through transformation matrices formed by directional cosines:

- (1) substructural coordinate system (Z). It is used in the analysis of the substructure itself
- (2) element coordinate system (Y). It is established with respect to each element according to the characteristics of each element to form the stiffness matrix for each element
- (3) nodal point coordinate system (J). At some nodal points, when the supporting reaction force exists or there

are parts which are connected to the main structure with planar force exerting on them, then it is necessary to establish coordinate systems for these nodal points. The use of this method can eliminate the symptom which may appear in the stiffness matrix which is formed according to another coordinate system because the stiffness component in the direction perpendicular to the planar force exerting object is zero. Thus, the solution seeking process of the structural equilibrium equations is not necessarily carried out under a unified coordinate system

- (4) geometric part coordinate system (H). It is established according to the characteristics of each geometric part in the substructure. It provides the typical parameters of the geometric parts and the lattice of the formation calculation
- (5) complete structure coordinate system (Q). It is used as the common reference system for all the substructures.

### 3. Treatment of constraints

The nodal degrees of freedom corresponding to the structural stiffness matrix assembled from the stiffness matrices of the elements may be linearly related to one another. Therefore, we must carry out constraint treatment in order to eliminate non-independent degrees of freedom.

#### (1) Multi-point constraint

The initial substructural equilibrium equation set obtained can be expressed as

$$\{K_s\} \{\delta_s\} = \{P_s\} \quad (2)$$

$\delta_s$  can be divided into  $\delta_n$  independent degrees of freedom and  $\delta_y$  non-independent degrees of freedom. This equation (2) can be divided as:

$$\begin{Bmatrix} \bar{K}_{nn} & K_{ny} \\ K_{yn} & K_{yy} \end{Bmatrix} \begin{Bmatrix} \delta_n \\ \delta_y \end{Bmatrix} = \begin{Bmatrix} P_n \\ P_y \end{Bmatrix} \quad (3)$$

$\delta_n$  and  $\delta_y$  have the following linear relation

$$\{\delta_y\} = [G_y] \{\delta_n\} \quad (4)$$

Substituting Equation (4) into Equation (3) and eliminating the non-independent degrees of freedom  $\delta_y$ , we get

$$[K_{nn}] \{\delta_n\} = \{P_n\} \quad (5)$$

where

$$\begin{aligned} [K_{nn}] &= K_{nn} + K_{ny}G_y + G_y^T K_{yn} + G_y^T K_{yy} G_y \\ \{P_n\} &= P_n + G_y^T P_y \end{aligned}$$

multi-point constraint is primarily used to simulated very stiff elements.

## (2) Single point constraint

If there are forced distortions  $Y_v$  along certain degrees of freedom, then the independent degrees of freedom  $\delta_n$  can be divided into forced distortions  $\delta_v$  and unconstrained degrees of freedom  $\delta_z$ , i.e.,

$$\begin{aligned} \{\delta_n\} &= \{Y_v\} \\ \{\delta_n\} &= \begin{Bmatrix} \delta_v \\ \delta_z \end{Bmatrix} \end{aligned} \quad (6)$$

Thus Equation (5) can be divided into:

$$\begin{Bmatrix} \bar{K}_{nn} & K_{nz} \\ K_{zn} & K_{zz} \end{Bmatrix} \begin{Bmatrix} \delta_v \\ \delta_z \end{Bmatrix} = \begin{Bmatrix} \bar{P}_n \\ P_z \end{Bmatrix} + \begin{Bmatrix} 0 \\ q_z \end{Bmatrix} \quad (7)$$

where  $q_z$  is the constraint force in the  $\delta_v$  direction. Substituting Equation (6) into (7) and eliminating the forced distortions  $\delta_v$ , we get

$$[K_{zz}] \{\delta_z\} = \{P_z\} \quad (8)$$

where  $[K_{zz}]$  is the same as  $\bar{K}_{zz}$  in Equation (7). Then

$$\{P_z\} = \bar{P}_z - K_{nz} Y_v$$

and we can obtain the constraint force

$$q_i = -P_i + K_{ii}\delta_i + K_{ir}\delta_r \quad (9)$$

All the constraint treatments are carried out under the nodal point coordinate system.

#### 4. Substructural analysis

After constraint treatment, the substructural equilibrium Equation (3) can be divided according to the internal degree of freedom  $\delta_i$  and boundary degree of freedom  $\delta_b$  as

$$\begin{bmatrix} K_{ii} & K_{ib} \\ K_{bi} & K_{bb} \end{bmatrix} \begin{Bmatrix} \delta_i \\ \delta_b \end{Bmatrix} = \begin{Bmatrix} P_i \\ P_b \end{Bmatrix} \quad (10)$$

Cancelling out  $\delta_i$ , we get

$$[K_b] \{\delta_b\} = \{\bar{P}_b\} \quad (11)$$

where the boundary stiffness:

$$[K_b] = K_{bb} - K_{bi}K_{ii}^{-1}K_{ib}$$

and the boundary equi-effective load:

$$\{\bar{P}_b\} = P_b - K_{bi}K_{ii}^{-1}P_i$$

#### 5. Treatment of extending structure

There are several extending structures connected to the main structure  $r_0$  and they are numbered as  $r = 1, 2, \dots, n$  as shown in Figure 1. For each extending structure, it is possible to obtain its boundary stiffness and boundary

equivalent load according to substructural analysis. Then, they can be added to the corresponding nodal points of the basic structure connecting to the extending structures. From these we obtain the stiffness and load on internal nodal points of the new basic structure which takes the contributions of the extending structures into consideration. Extending structures can also be treated as first level substructures.

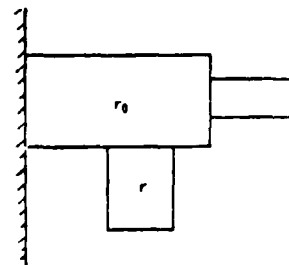


Figure 1. Schematic diagram of extending structures

## 6. Treatment of symmetry

Symmetry is frequently encountered in aeronautical structures. It may be symmetric for whole structures or for part of the structure. For example, a substructure itself or two substructures mutually may be symmetric. At this time, through symmetry treatment, we can only calculate half of the symmetric structure and the calculated results of the other half can be obtained through reflection or other methods. It can significantly reduce the computation time.

### (1) Using load analysis to treat the symmetry properties

Under the condition that the complete structure is symmetric, if the load is symmetric or asymmetric, it is possible to calculate half of it. If the load is not symmetric, then we should first decompose the load into a symmetric and an asymmetric group. The nodal degree of freedom on the symmetric plane of the structure is treated based on the single point constraint treatment. Therefore, under symmetric load, the distortion of the nodal points on the symmetry plane and that corresponding to the asymmetric degree of freedom are zero. Under asymmetric load, the nodal distortion on the symmetry plane and that corresponding to the symmetric degree of freedom are zero. First, we calculate half of the structure and then obtain the symmetric results for the other half by combining the displacements under the two sets of loads.

### (2) Using substructure substitution method to treat the symmetry properties

For two substructures I and II under different loads and symmetric, we can calculate substructure I and then reflect the load on substructure II to substructure I to obtain the results of substructure I under the load condition of substructure II. Then through



another reflection, we can obtain the results for substructure II. This method is called substructure substitution method. By using this method, it is not necessary to separate an unsymmetric load into symmetric and asymmetric parts.

#### 7. Connection of substructures and analysis of multi-level substructures

The boundary stiffness and boundary equivalent load obtained from substructural analysis are assembled according to the structural relations into the first level substructure. By eliminating the degrees of freedom  $\delta_1$  of the internal points of the first order substructures, we can calculate the boundary stiffness and boundary equivalent load of the first level substructure. Using the boundary stiffness and boundary equivalent load of the first level substructures, we can assemble them into second level substructures. Similarly, it moves on to the highest level, i.e., the entire structure.

The above process of the gradual disappearance of the degrees of freedom is approximately shown in Figure 2. Finally, the equilibrium equation of the entire structure is

$$(K_e)\{\delta_e\} = \{P_e\} \quad (12)$$

After determining  $\delta_k$ , we can substitute it backwards by the level to obtain  $\delta_j$  and  $\delta_1$ . Then, based on the actual displacement of the nodal point, the internal force and stress of the element can be determined using the equilibrium equation of the element.

#### 8. Calculation of the influencing coefficient

The system can calculate the influencing coefficient of the wing structure with the consideration of the elasticity of the frame of the aircraft. During the calculation, we add unit load onto the points at which the influencing coefficients are computed. By

repeating the displacement calculation in the structural analysis, we can obtain the displacement of every point under unit load conditions. These displacements can be used too from the influencing coefficient matrix  $C^{ZZ}$ . From  $C^{ZZ}$  we can take out elements in the tangential and normal directions. From the displacement, we can use a five point interpolation method to calculate the turning angle and then obtain  $C^{\theta Z}$  and  $C^{\phi Z}$

$$\delta_s = \begin{Bmatrix} \delta_y \\ \delta_z \end{Bmatrix} \rightarrow \delta_n = \begin{Bmatrix} \delta_y \\ \delta_z \end{Bmatrix} \rightarrow \delta_r = \begin{Bmatrix} \delta_u \\ \delta_w \end{Bmatrix} \rightarrow \delta_\theta = \begin{Bmatrix} \delta_\theta \\ \delta_\phi \end{Bmatrix} \rightarrow \delta_K$$

$\xrightarrow{1}$  多点约束处理  $\xrightarrow{2}$  单点约束处理  $\xrightarrow{3}$  0级子结构分析  $\xrightarrow{4}$  2级子结构分析  
 消去 $\delta_y$  消去 $\delta_z$  消去 $\delta_u$  消去 $\delta_w$

Figure 2. Gradual elimination of nodal DOF

Key: 1--elimination of  $\delta_y$  by multi-point constraint treatment;  
 2--elimination of  $\delta_z$  by single point constraint treatment;  
 3--elimination of  $\delta_u$  by 0th level substructural analysis;  
 4--elimination of  $\delta_w$  by multi-level substructural analysis

## V. PREPARATION OF DATA

When carrying out large complex structural analysis on the computer, the preparation of the original data is very complicated. The time required to prepare the original data very frequently exceeds the time used to carry out the operation on the computer. In order to simplify the data preparation work, HAJIF-I is equipped with an external load calculation module and a structural data formation module for the user.

### 1. Calculation of external load

The load calculation module provided by the system can place the aerodynamic force distribution of the wing, tail and body of the aircraft obtained from the wind tunnel experiments or calculated based on the strength specifications on the nodal points of the aerodynamic lattice. The mass distribution of the structure can

similarly be concentrated on each structural nodal points using the load computation module. With the aerodynamic load and mass distributions, it is possible to calculate the linear and angular accelerations of the entire aircraft. Therefore, the moment of inertia is obtained. The moment of inertia calculated this way is naturally in equilibrium with the aerodynamic load.

## 2. Formation of structural data

The formation and organization of data use an assembly type of technique. Each substructure can be divided into several geometric parts and structural data are generated on the basis of geometric parts. In order for the users to easily control the system, it provides data formation statements for the users. The users use statements to provide the original data and the data formation module can automatically generate the relevant structural data according to the needs of the users.

### (1) External load equivalent displacement statement

The aerodynamic load calculated using the load computation module is distributed onto the nodal points of the aerodynamic computational lattice. These nodal points are generally different from those of the idealized structure. Therefore, it is necessary to move these loads equivalently to the structural nodal points.

Using statement DY LX01 can transfer the aerodynamic load on the wing from aerodynamic nodal points equivalently to the structural nodal points on the wing.

Using statement DY LX02 can transfer the aerodynamic load on the body from the aerodynamic nodal points to the structural nodal points on the body.

For loads that these two statements cannot be used, a statement can be provided manually.

## (2) Geometric part shape statement

For geometric parts with regular geometric shape, we can use the geometric part shape statement to automatically carry out the lattice distribution of this part and simultaneously generate the nodal numbering and coordinate systems. The only original data provided by the user are the coordinate systems of the control points and the parameters used in the distribution of the lattice. The system has 13 geometric part shape statements as shown in Table 3.

## (3) Elemental position formation statement

Which nodal points are connected to an element can be automatically provided by the elemental position formation statement. The system is equipped with five elemental position formation statements as shown in Table 4.

## (4) Repetition statement

In the data describing an idealized mechanical model, some of them have a repetitive and cumulative nature. Using the repetition statement to describe such data can drastically reduce the work load. The equi-difference repetition statement DC can be used to provide data formed by an algebraic series. If a certain cumulative law exists between a few DC statements, then it is also possible to use a second level repetition statement DCF to write a single statement.

Identical repetition statement DTF can be used to provide a series of identical data.

TABLE 3. GEOMETRIC PART SHAPE STATEMENT

Number	Part shape statement
1	JHLX01
2	JHLX02
3	JHLX03
4	JHLX04
5	JHLX05
6	JHLX06
7	JHLX07
8	JHLX08
9	JHLX09
10	JHLX10
11	JHLX80
12	JHLX81
13	JHLX82

TABLE 3 (continued)

Function
dividing a segment of a straight line at a ratio
dividing a segment of an arc at a ratio
dividing a segment of a parabola at a ratio
dividing a segment of a simple curve according to a fixed law
dividing a segment of a compositional curve according to a fixed law
dividing a triangular lattice
dividing a quadrilateral lattice
dividing a right conical lattice formed on the basis of a computational curve
dividing a right cross-sectional conical lattice formed on the basis of two composition curves
dividing the parabolic cross-sectional conical lattice formed on the basis of three compositional curves
geometric part types with irregular nodal points
dividing the planer quadrilateral lattice surrounded by four compositional curves
dividing the curved lattice formed on the basis of several parallel compositional curves which also are compositional curves in the longitudinal direction

TABLE 4. ELEMENTAL POSITION FORMATION STATEMENTS

Number	Elemental position statement	Function
1	YSWZ01	spatial line formed by linear elements
2	YSWZ02	spatial plane formed by linear and planar elements. Two parameters are used to determine the transverse and longitudinal dividing segments
3	YSWZ03	spatial plane formed by linear and planar elements. One parameter is used to determine the dividing number of segments on three sides
4	YSWZ04	A tube formed by linear and planar elements. Two parameters are used to determine the number of segments along the long axis and the radial direction
5	YSWZ06	spatial plane formed by linear and planar elements. One parameter is used to determine the number of segments in one direction while another parameter is used to determine the number of segments in the other two directions

## VI. DECOMPOSITION OF HIGHER ORDER MATRIX

HAJIF-I requires that the limitations to the bandwidth and the order of the stiffness matrix must be minimized for the matrix decomposition method used. This type of requirement is often in contradiction to the high efficiency of computation. Therefore, in the development of the system, we developed two methods so that higher efficiency can be achieved under the conditions that these requirements are satisfied. There are two ways to increase the efficiency:

(1) Minimize the number of multiplication and addition of the inner level in the matrix decomposition to avoid computations which are not going to alter the results of the computation;

(2) minimize the amount of data exchanged between the internal and external memories of the computer because the speed of data transmission between the internal and external memories is several orders of magnitude slower than that of internal memory operations.

### 1. Modified variable bandwidth method

For a series of linear algebraic equations such as shown in Equation (1)

$$[K]\{\delta\} = \{P\}$$

where  $[K]$  is symmetrically orthogonal. It can be decomposed trigonometrically as the following:

$$[K] = U^T D U \quad (13)$$

Therefore, Equation (1) can be written as

$$U^T D Y = P \quad (14)$$

$$Y = U \delta \quad (15)$$

Equation (14) is called the progressive form and Equation (15) is the iterative form.  $U$  is the unit upper triangular matrix.  $D$  is



a diagonal matrix. Their elements can be obtained using the following equations:

$$d_{ii} = k_{ii} - \sum_{r=m_i}^{i-1} \frac{\bar{u}_{ri}}{d_{rr}} \quad (16)$$

$$\bar{u}_{ji} = u_{ji} d_{ii} - \sum_{r=m_m}^{i-1} u_{jr} u_{ri} \quad (17)$$

where  $m_i$  represents the first non-zero element of the  $i$ th column of the matrix  $[K]$  and

$$m_m = \text{MAX}\{m_i m_j\}$$

represents the half bandwidth of the  $i$ th row. The cumulative term in Equation (17) is the inner cycle of the computation. Please note that there is only one multiplication involved. Based on Equations (16) and (17), all the zeros outside the bandwidth do not participate in the computation. In addition, all the non-zero elements of the  $i$ th and  $j$ th columns smaller than  $m_m$  also do not participate in the calculation so that the (1) requirement to raise the computational efficiency is satisfied.

The storage format of this method is the upper triangular variable bandwidth memory. In order to overcome the disadvantage of the variable bandwidth methods used here and abroad involving the transfer of large amounts of useless elements for the decomposition between internal and external memories, the data in the internal memory are automatically formed into pieces and effective columns. The criterion used to judge an effective column is that when  $m_j > i$ , column  $j$  is ineffective and when  $m_j < j$ , column  $j$  is effective. In the pieces every column is a principal column in the decomposition. For the columns follow the pieces, only the elements of the effective columns needed in the computation are transferred into the internal memory. Thus, the only elements stored in the internal memory are the ones necessary for the decomposition computation each time. The amount of data exchanged between the internal and external memories is reduced.

In the substructural analysis, we cannot proceed based on the direct decomposition as in Equation (13) because it is necessary to provide the boundary stiffness and the boundary equivalent load of the substructure. At this time we have to use Equation (10) which is

$$\begin{bmatrix} K_{ii} & K_{ib} \\ K_{bi} & K_{bb} \end{bmatrix} \begin{Bmatrix} \delta_i \\ \delta_b \end{Bmatrix} = \begin{Bmatrix} P_i \\ P_b \end{Bmatrix} \quad (10)$$

Decomposition with respect to Equation (10) is equivalent to the following transformation:

$$\begin{bmatrix} (U_i^T D_i)^{-1} & 0 \\ 0 & I \end{bmatrix} \begin{bmatrix} K_{ii} & K_{ib} \\ K_{bi} & K_{bb} \end{bmatrix} \begin{Bmatrix} \delta_i \\ \delta_b \end{Bmatrix} = \begin{bmatrix} (U_i^T D_i)^{-1} & 0 \\ 0 & I \end{bmatrix} \begin{Bmatrix} P_i \\ P_b \end{Bmatrix} \quad (18)$$

After expansion we get

$$\begin{bmatrix} U_i & (U_i^T D_i)^{-1} K_{ib} \\ K_{bi} & K_{bb} \end{bmatrix} \begin{Bmatrix} \delta_i \\ \delta_b \end{Bmatrix} = \begin{bmatrix} (U_i^T D_i)^{-1} P_i \\ P_b \end{bmatrix} \quad (19)$$

From equations

$$\bar{K}_b = K_{bb} - K_{bi} K_{ii}^{-1} K_{ib}$$

$$P_b = P_b - K_{bi} K_{ii}^{-1} P_i$$

we can get

$$\bar{K}_b = K_{bb} - (D_i^{-1} (U_i^T)^T K_{ib})^T D_i (D_i^{-1} (U_i^T)^T K_{ib}) \quad (20)$$

$$P_b = P_b - (D_i^{-1} (U_i^T)^T K_{ib})^T D_i (D_i^{-1} (U_i^T)^T P_i) \quad (21)$$

Therefore, we know that  $D_i^{-1} (U_i^T)^T K_{ib}$  and  $D_i^{-1} (U_i^T)^T P_i$  are the results of decomposition of Equation (10).

## 2. Hyper-matrix method

The basic concept of the hyper-matrix method is to divide a large matrix (called original level matrix) into many submatrices (called original level submatrices) according to the rows and columns by an equal distance. The size of the submatrix is just

equal to the length of the logic record of the document. The address of these submatrices can be stored in the auxiliary memory which is directly accessible. We can arrange these submatrices according to corresponding position in the original level matrix to obtain a second level address index matrix (the address of a submatrix whose elements are all zero is defined as zero). If the order of the second level address index matrix is still too high, we can use the above described method to divide further to obtain a third level address index matrix.

On the basis of the hyper-matrix method concept, the stiffness matrix and load matrix in Equation (10) can be organized according to third order hyper-matrix method and then carry out trigonometrical decomposition. That is:

$$[K] = \begin{bmatrix} K_1 & K_2 \\ K_3 & K_4 \end{bmatrix} = \begin{bmatrix} K_{11} & & & \\ K_{21} & K_{22} & & \\ \dots & \dots & \dots & \dots \\ K_{n_1 1} & K_{n_1 2} & \dots & K_{n_1 n_1} \\ \dots & \dots & \dots & \dots \\ K_{n_2 1} & K_{n_2 2} & \dots & K_{n_2 n_1} & \dots & K_{n_2 n_2} \end{bmatrix} \quad (22)$$

$$[P] = \begin{bmatrix} P_1 \\ P_2 \end{bmatrix} = \begin{bmatrix} P_{11} & P_{12} & \dots & P_{1n_0} \\ P_{21} & P_{22} & \dots & P_{2n_0} \\ \dots & \dots & \dots & \dots \\ P_{n_1 1} & P_{n_1 2} & \dots & P_{n_1 n_0} \\ \dots & \dots & \dots & \dots \\ P_{n_2 1} & P_{n_2 2} & \dots & P_{n_2 n_0} \end{bmatrix} \quad (23)$$

where  $K_{ij}$  ( $i, j = 1, 2, \dots, n_1$ ) and  $P_{ik}$  ( $i = 1, 2, \dots, n_1, k = 1, 2, \dots, n_0$ ) are the original level submatrices of  $[K]$  and  $[P]$ , respectively.  $n_1$  is the original level piece number of the substructural internal degree of freedom.  $n_2$  is the original level piece number of the total substructural degree of freedom.  $n_0$  is the original piece number of the condition under load.

Consider the piece breaking form in Equation (22), and let

$$(K) = LDL^T + B \quad (24)$$

where

$$L = \begin{bmatrix} L_1 & 0 \\ L_{n_1} & 0 \end{bmatrix}, \quad D = \begin{bmatrix} D_1 & 0 \\ 0 & 0 \end{bmatrix}$$

Further, satisfy the following equations:

$$K_1 = L_1 D_1 L_1^T \quad (25)$$

$$K_{n_1} = L_{n_1} D_1 L_1^T \quad (26)$$

then

$$B = \begin{bmatrix} 0 & 0 \\ 0 & \bar{K}_{n_1} \end{bmatrix} \quad (27)$$

$$\begin{aligned} \bar{K}_1 &= K_1 - L_{n_1} D_1 L_1^T \\ \bar{P}_1 &= P_1 - L_{n_1} L_1^{-1} P_1 \end{aligned} \quad (28)$$

Let the division of L and D be the same as that for K and expand K, L and D according to Equation (26) in terms of original level submatrices and also let

$$\bar{L}_{ii} = L_{ii} D_{ii} \quad (29)$$

$$\bar{K}_{ii} = K_{ii} - \sum_{q=1}^{m_i} L_{iq} L_{iq}^T \quad (30)$$

where  $m_i = \min(j-1, n_1)$ , then

$$\bar{L}_{ii} \bar{L}_{ij}^T = \bar{K}_{ii} \quad (31)$$

where  $j = 1, 2, \dots, i$ ,  $i = 1, 2, \dots, n_1$ . There are three situations with respect to  $\bar{K}_{ij}$ :

(1)  $i, j > n_1$ , from Equation (27), we know the  $\bar{K}_{ij}$  at this time is the original level submatrix of  $\bar{K}_B$ .

(2)  $i = j$ ,  $i \leq n_1$ . From Equations (29), (30) and (31), we know

$$L_{ii} D_{ii} L_{ii}^T = K_{ii}$$

This equation is the corrected CHOKESKEY trigonometrical decomposition of the original level main diagonal submatrix.

(3)  $i > j, j \leq J_0 = \min(i-1, n_1)$  . From Equation (31), we can find  $\bar{L}_{ij}$  and then obtain  $L_{ij}$  from Equation (29).

The hyper-matrix method has less amount of data transfer between the internal and external memories. It is suitable to solve for a larger structure with a relatively smaller internal memory and it has the advantage of a simpler program design.

#### A FAMILY OF TAPERED BEAM CONFORMING ELEMENTS AND ITS APPLICATION TO BEAM NATURAL VIBRATION ANALYSIS

Beijing Institute of Aeronautics and Astronautics  
Zhu Dechao

#### ABSTRACT

This paper gives the explicit expressions for the stiffness and mass matrices of the tapered beam elements with displacement functions based on the third, fifth and seventh order polynomial, respectively. In addition, a general method for evaluating the expressions of the stiffness and mass matrices of even higher order tapered beam elements with arbitrary odd power is also given. Then by means of these high order conforming elements, we calculated the first five natural frequencies and vibrational modes for the six types of linear tapered beams under suspending arm support, two-ended simple support and two-ended fixed support conditions. The results indicate that under all conditions, the higher order elements exhibit better convergence than the lower order elements.

However, if boundary conditions of imposing forces are applied, then under the conditions of using fewer elements with deeper tapered beams, the results obtained from the high order elements are not better than those obtained from the lower order elements.

## I. INTRODUCTION

The beam is an important structural element. As for the use of the finite element method to calculate the natural vibration problem of the beam, there have been many published papers in this area. In a recent paper [3], the natural vibration problem of the linear tapered suspending beam was calculated using high order elements (the displacement function of the element corresponds to fifth and seventh order polynomials). Its results indicate that under certain conditions the use of high order element cannot compensate for the loss in accuracy due to the roughness of segmentation. It is especially worth our attention that, for conically shaped or other deeply tapered beams, when a few elements are used, the results obtained using higher order elements are poorer than those with lower order elements. This completely is a surprise to everyone. In clarity, this problem is one of the purposes of this paper.

Starting from the variational principle, this paper first reviews the continuity and boundary conditions which should and must be satisfied by the finite element displacement method. In addition, on the basis of the above it gives the explicit expressions for the stiffness and mass matrices of tapered beam conforming elements with elemental displacement functions corresponding to the third, fifth and seventh order polynomial. Since the conforming elements can vigorously treat the problem based on the variational principle, the

---

Received in February 1980

results obtained from high order elements are satisfactory. It has better convergence than low order elements. Furthermore, because high power polynomial displacement function can better reflect the distortion characteristics of tapered beams, the deeper the taper of the beam is the more significant the advantage of the high order elements becomes. For example, for a conically shaped suspending beam, with merely one element, a seventh power high order element can give the first few natural frequencies with sufficient accuracy. As for the type of high order elements used in [3], because the boundary conditions imposed exceed the range required by the variational principle, under certain conditions the results obtained using high order elements are not better than those using lower order elements. The deeper the beam taper is, the more significant this disadvantage becomes and it further deviates from the rational of using high order elements.

## II. VARIATIONAL FORM OF THE BEAM NATURAL VIBRATION PROBLEM

As we commonly know that the natural vibration angular frequency  $\omega$  of the Bernoulli beam and the Rayleigh quotient have the following relation:

$$\omega^2 = St \frac{\int_0^l EJ \left( \frac{d^2 w}{dx^2} \right)^2 dx}{\int_0^l \rho A w^2 dx} \quad (1)$$

where  $x$  is the longitudinal coordinate of the beam;  $l$ ,  $w(x)$ ,  $EJ(x)$ ,  $\rho A(x)$  are the length, the bending, the bending stiffness and the unit length mass of the beam respectively.  $St$  represents the stationary value of the generalized function.

In Equation (1),  $w$  is an independent variable function. According to the variational principle, we only have to satisfy its displacement boundary conditions which are for

$$\begin{aligned} \text{fixed supported end:} \quad w = \frac{dw}{dx} = 0 \\ \text{simple supported end:} \quad w = 0 \end{aligned} \quad (2)$$

Under the above conditions, after carrying out variational operations and partial integrations, we can prove without too much difficulty that the variation Equation (1) and the natural vibration equilibrium differential equation and its imposed boundary conditions are completely equivalent [4].

Furthermore, it is common knowledge that because the highest order of the derivative of the variable function  $w$  is 2, therefore, it is required that  $w$  has  $C^1$  continuity in the selection of variable function in the finite element method. We might as well call those finite elements which totally satisfy or merely satisfy the displacement boundary conditions and the  $C^1$  continuity requirement as conforming elements and call the finite elements which exceed the range of boundary conditions and continuity requirements as excessively conforming elements.

Apparently, excessively conforming elements are not suitable for use under the conditions that the elasticity or the inertia characteristic of the beam is changing abruptly (that is corresponding to the conditions that the properties of the materials or the shape of the cross-sectional section change suddenly or there is concentration of mass in the structure). It is because at the locations where those changes occur, higher order derivatives actually are not continuous and using excessively conforming elements may even lead to the convergence toward an inaccurate solution. In that case, what is the comparison between the effect of using excessively conforming elements with that of the conforming elements for beams with continuous elasticity and inertia? This is also an interesting problem in this paper.

### III. THE FAMILY OF CONFORMING BEAM ELEMENTS

For high order polynomial displacement functions, they can be matched with various types of nodal parameter combinations and Figure 1 shows some of the examples. Corresponding to the fifth and



and seventh order polynomial displacement functions, [3] adopted the form shown in Figure 1a to establish two kinds of high order beam elements. Because it is required that high order derivatives must be continuous at the junctions of neighboring elements (i.e., for fifth order displacement functions it is required that  $\frac{d^3w}{dx^3}$  is continuous and for the seventh order displacement function, both  $\frac{d^4w}{dx^4}$  and  $\frac{d^5w}{dx^5}$  are continuous), as well as that the imposed boundary conditions must be satisfied, therefore, this is a type of excessively conforming elements. In this paper we will use the symbols (TB57) and (TB7) to represent the fifth and seventh order excessively conforming elements with the imposition of boundary conditions and use (TB5) and (TB7) to represent the corresponding elements when boundary conditions are imposed. Actually, all we have to consider is that the higher order derivatives are internal nodal parameters of the elements and do not force them to be continuous at the junctions. This way we can also obtain the corresponding conforming elements. Of course, in order to reduce the bandwidth of the final beam matrix, it is better to rearrange the nodal parameters into a proper sequence. The explicit expressions for the stiffness and mass matrices of (TB5) and (TB7) have already been given in [3].

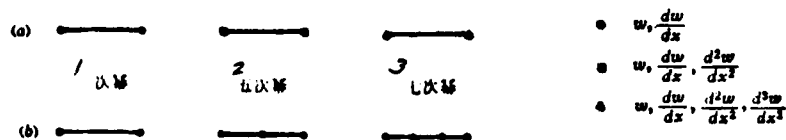


Figure 1

Key: 1--3rd order power; 2--5th order power; 3--seventh order power

For the convenience of the establishment of the family of conforming elements corresponding to an arbitrary high odd power polynomial displacement function, this paper suggests that we adopt the same nodal parameter combination as shown in Figure 1b. Assuming

an element has  $n$  nodal points, with the exception of the two nodal points located at the two ends of the element, the remaining are internal nodal points of the element. Every nodal point is assigned by two nodal parameters  $w$  and  $\frac{dw}{dx}$ , respectively. Thus, there are a total of  $2n$  nodal parameters. The corresponding displacement function is a  $(2n-1)$  power polynomial which can be expressed as [5]:

$$w(x) = \sum_{i=1}^n \left[ H_{0i}(x) w(x_i) + H_{1i}(x) \frac{dw(x_i)}{dx} \right] \quad (3)$$

where  $w(x_i)$  and  $\frac{dw(x_i)}{dx}$  represent the displacement and its derivative of the element at the  $i$ th nodal point which are the two nodal parameters at the  $i$ th nodal point,  $H_{j,i}(x)$  is an  $n$  point first under Hermitian intrapolation function and its actual expression is:

$$H_{0i}(x) = \left[ 1 - 2 \frac{dL_i(x_i)}{dx} (x - x_i) \right] [L_i(x)]^2$$

$$(i = 1, 2, \dots, n) \quad (4)$$

$$H_{1i}(x) = (x - x_i) [L_i(x)]^2$$

where

$$L_i(x) = \frac{\prod_{j \neq i} (x - x_j)}{\prod_{j \neq i} (x_i - x_j)} \quad (i, j = 1, 2, \dots, n) \quad (5)$$

which is a Lagrange intrapolation function.

Using the characteristics of the Hermitian intrapolation function, we know that the Hermitian intrapolation function for each term in Equation (3) is the shape function of the corresponding nodal parameter. For the convenience of the calculation which follows, we are rewriting Equation (3) into:

$$w(x) = xHW \quad (6)$$

where  $x = [1 \quad x \quad x^2 \quad \dots \quad x^{2n-1}]$ ,

$W = \left[ w_1 \quad \frac{dw_1}{dx} \quad \dots \quad w_n \quad \frac{dw_n}{dx} \right]^T$ ,  $T$  represents a matrix transformation symbol.

H is the matrix formed by an array of the coefficients of the Hermitian intrapolation function.

When the nodal points are evenly distributed, we can use Equations (5) and (4) to directly derive the following results where L is the length of the element.

(1) Third order polynomial,  $n = 2$

$$H = \begin{bmatrix} 1 & 0 & 0 & 0 \\ 0 & 1 & 0 & 0 \\ -\frac{3}{L^2} & -\frac{2}{L} & \frac{3}{L^2} & -\frac{1}{L} \\ \frac{2}{L^3} & \frac{1}{L^2} & -\frac{2}{L^3} & \frac{1}{L^2} \end{bmatrix} \quad (7 (a))$$

(2) Fifth order polynomial,  $n = 3$

$$H = \begin{bmatrix} 1 & 0 & 0 & 0 & 0 & 0 \\ 0 & 1 & 0 & 0 & 0 & 0 \\ -\frac{23}{L^2} & -\frac{6}{L} & \frac{16}{L^2} & -\frac{8}{L} & \frac{7}{L^2} & -\frac{1}{L} \\ \frac{66}{L^3} & \frac{13}{L^2} & -\frac{32}{L^3} & \frac{32}{L^2} & -\frac{34}{L^3} & \frac{5}{L^2} \\ -\frac{68}{L^4} & -\frac{12}{L^3} & \frac{16}{L^4} & -\frac{40}{L^3} & \frac{52}{L^4} & -\frac{8}{L^2} \\ \frac{24}{L^5} & \frac{4}{L^4} & 0 & -\frac{16}{L^4} & -\frac{24}{L^5} & \frac{4}{L^4} \end{bmatrix} \quad (7 (b))$$

(3) Seventh order polynominal,  $n = 4$

$$H = \begin{bmatrix} 4 & 0 & 0 & 0 & 0 & 0 & 0 & 0 \\ 0 & 4 & 0 & 0 & 0 & 0 & 0 & 0 \\ -\frac{291}{L^2} & -\frac{44}{L} & 0 & -\frac{108}{L} & \frac{243}{L^2} & -\frac{54}{L} & \frac{48}{L^2} & -\frac{4}{L} \\ \frac{1691}{L^3} & \frac{193}{L^3} & \frac{972}{L^3} & \frac{864}{L^3} & -\frac{2187}{L^3} & \frac{513}{L^3} & -\frac{476}{L^3} & \frac{40}{L^3} \\ -\frac{4230}{L^4} & -\frac{432}{L^3} & -\frac{4860}{L^4} & -\frac{2619}{L^3} & \frac{7290}{L^4} & -\frac{1836}{L^3} & \frac{1800}{L^4} & -\frac{153}{L^3} \\ \frac{5418}{L^5} & \frac{522}{L^4} & \frac{8991}{L^5} & \frac{3807}{L^4} & -\frac{11178}{L^5} & \frac{3078}{L^4} & -\frac{3231}{L^5} & \frac{279}{L^4} \\ -\frac{3483}{L^5} & -\frac{324}{L^4} & -\frac{7290}{L^5} & -\frac{2673}{L^4} & \frac{8019}{L^5} & -\frac{2430}{L^4} & \frac{2754}{L^5} & -\frac{243}{L^4} \\ \frac{891}{L^6} & \frac{81}{L^5} & \frac{2187}{L^6} & \frac{729}{L^5} & -\frac{2187}{L^6} & \frac{729}{L^5} & -\frac{891}{L^6} & \frac{81}{L^5} \end{bmatrix} \quad (7 (c))$$

The elements established according to Equation (6) because it is only required for  $w$  and  $\frac{dw}{dx}$  to be continuous at the end points, it is then a type of conforming elements which are represented by TB3, TB5 and TB7 in this paper, respectively. Similarly, we can easily obtain a high order conforming element family.

#### IV. THE EXPRESSIONS FOR THE STIFFNESS AND MASS MATRICES OF TAPERED BEAM ELEMENT

For linearly tapered beam elements, its cross-sectional area ( $A(x)$ ) and the rotational inertia  $J(x)$  about the axis of center of gravity can always be expressed as:

$$A(x) = A_{m-1} \left( 1 + \alpha_1 \frac{x}{L} + \alpha_2 \frac{x^2}{L^2} \right) \quad (8)$$

$$J(x) = J_{m-1} \left( 1 + \beta_1 \frac{x}{L} + \beta_2 \frac{x^2}{L^2} + \beta_3 \frac{x^3}{L^3} + \beta_4 \frac{x^4}{L^4} \right)$$

where  $A_{m-1}$  and  $J_{m-1}$  are the cross-sectional area and rotational inertia of the  $m$ th element on its left side respectively. All the

coefficients  $\alpha_1$  and  $\beta_1$  are not difficult to calculate based on the actual situation.

Therefore, the mass matrix  $M$  and the stiffness matrix  $K$  of the tapered beam element can be calculated according to:

$$\begin{aligned} M &= \rho A_{m-1} H^T \left( \int_0^L \left( 1 + \alpha_1 \frac{x}{L} + \alpha_2 \frac{x^2}{L^2} \right) x^T x dx \right) H \\ K &= EJ_{m-1} H^T \left[ \int_0^L \left( 1 + \beta_1 \frac{x}{L} + \beta_2 \frac{x^2}{L^2} + \beta_3 \frac{x^3}{L^3} + \beta_4 \frac{x^4}{L^4} \right) \frac{d^2 x^T}{dx^2} \cdot \frac{d^2 x}{dx^2} dx \right] H \end{aligned} \quad (9)$$

where  $\rho$  and  $E$  are density and elastic modules, respectively. Actually, by using a simple computation program we can calculate the results of Equation (9). Because of the symmetry of the matrix, we are only going to write the upper triangular portion.

#### 1. TB3

$$\begin{aligned} m_{11} &= V(936 + 216\alpha_1 + 76\alpha_2) \\ m_{12} &= VL(132 + 42\alpha_1 + 17\alpha_2) \\ m_{13} &= V(324 + 162\alpha_1 + 92\alpha_2) \\ m_{14} &= VL(-78 - 36\alpha_1 - 19\alpha_2) \\ m_{22} &= VL^2(24 + 9\alpha_1 + 4\alpha_2) \\ m_{23} &= VL(78 + 42\alpha_1 + 25\alpha_2) \\ m_{24} &= VL^2(-18 - 9\alpha_1 - 5\alpha_2) \\ m_{33} &= V(936 + 720\alpha_1 + 580\alpha_2) \\ m_{34} &= VL(-132 - 90\alpha_1 - 65\alpha_2) \\ m_{44} &= VL^2(24 + 15\alpha_1 + 10\alpha_2) \end{aligned}$$

The above are elements of the mass matrix and  $V = \rho A_{m-1} / 2520$ .

$$\begin{aligned} k_{11} &= J(1260 + 630\beta_1 + 504\beta_2 + 441\beta_3 + 396\beta_4) / L^3 \\ k_{12} &= J(630 + 210\beta_1 + 147\beta_2 + 126\beta_3 + 114\beta_4) / L^3 \\ k_{13} &= -k_{11} \\ k_{14} &= J(630 + 420\beta_1 + 357\beta_2 + 315\beta_3 + 282\beta_4) / L^3 \\ k_{22} &= J(420 + 105\beta_1 + 56\beta_2 + 42\beta_3 + 36\beta_4) / L \\ k_{23} &= -k_{12} \\ k_{24} &= J(210 + 105\beta_1 + 91\beta_2 + 84\beta_3 + 78\beta_4) / L \\ k_{33} &= k_{11} \\ k_{34} &= -k_{14} \\ k_{44} &= J(420 + 315\beta_1 + 266\beta_2 + 231\beta_3 + 204\beta_4) / L \end{aligned}$$

The above are the elements of the stiffness matrix and  $J = EJ_{m-1}/105$ .

2. TB5

$$m_{11} = V(54392 + 5616\alpha_1 + 1108\alpha_2)$$

$$m_{12} = VL(2964 + 442\alpha_1 + 111\alpha_2)$$

$$m_{13} = V(22880 + 7280\alpha_1 + 3328\alpha_2)$$

$$m_{14} = VL(-4160 - 312\alpha_1 + 288\alpha_2)$$

$$m_{15} = V(6812 + 3406\alpha_1 + 2428\alpha_2)$$

$$m_{16} = VL(-754 - 312\alpha_1 - 201\alpha_2)$$

$$m_{22} = VL^2(208 + 39\alpha_1 + 12\alpha_2)$$

$$m_{23} = VL(2288 + 832\alpha_1 + 416\alpha_2)$$

$$m_{24} = VL^2(-312 + 48\alpha_2)$$

$$m_{25} = VL(754 + 442\alpha_1 + 331\alpha_2)$$

$$m_{26} = VL^2(-78 - 39\alpha_1 - 27\alpha_2)$$

$$m_{33} = V(146432 + 73216\alpha_1 + 39936\alpha_2)$$

$$m_{34} = VL(3328\alpha_1 + 3328\alpha_2)$$

$$m_{35} = V(22880 + 15600\alpha_1 + 11648\alpha_2)$$

$$m_{36} = VL(-2288 - 1456\alpha_1 - 1040\alpha_2)$$

$$m_{44} = VL^2(3328 + 1664\alpha_1 + 1024\alpha_2)$$

$$m_{45} = VL(4160 + 3848\alpha_1 + 3248\alpha_2)$$

$$m_{46} = VL^2(-312 - 312\alpha_1 - 264\alpha_2)$$

$$m_{55} = V(54392 + 48776\alpha_1 + 44268\alpha_2)$$

$$m_{56} = VL(-2964 - 2522\alpha_1 - 2191\alpha_2)$$

$$m_{66} = VL^2(208 + 169\alpha_1 + 142\alpha_2)$$

where  $V = \rho A_{m-1}/360360$

$$k_{11} = J(504108 + 93654\beta_1 + 47784\beta_2 + 32769\beta_3 + 26028\beta_4)/L^3$$

$$k_{12} = J(112662 + 12474\beta_1 + 5907\beta_2 + 4290\beta_3 + 3546\beta_4)/L^3$$

$$k_{13} = J(-354816 - 19008\beta_1 + 23232\beta_2 + 36432\beta_3 + 41184\beta_4)/L^3$$

$$k_{14} = J(190080 + 57024\beta_1 + 38544\beta_2 + 31416\beta_3 + 27648\beta_4)/L^3$$

$$k_{15} = J(-149292 - 74646\beta_1 - 71016\beta_2 - 69201\beta_3 - 67212\beta_4)/L^3$$

$$k_{16} = J(23958 + 14652\beta_1 + 14949\beta_2 + 15279\beta_3 + 15426\beta_4)/L^3$$

$$k_{22} = J(32868 + 2673\beta_1 + 880\beta_2 + 594\beta_3 + 492\beta_4)/L$$

$$k_{23} = J(-88704 - 3168\beta_1 + 3696\beta_2 + 5280\beta_3 + 5808\beta_4)/L^3$$

$$k_{24} = J(31680 + 6336\beta_1 + 4840\beta_2 + 4224\beta_3 + 3816\beta_4)/L$$

$$k_{25} = J(-23958 - 9306\beta_1 - 9603\beta_2 - 9570\beta_3 - 9354\beta_4)/L^3$$

$$k_{26} = J(3762 + 1881\beta_1 + 2035\beta_2 + 2112\beta_3 + 2142\beta_4)/L$$

$$k_{33} = J(709632 + 354816\beta_1 + 270336\beta_2 + 228096\beta_3 + 202752\beta_4)/L^3$$

$$k_{34} = J(76032\beta_1 + 76032\beta_2 + 71808\beta_3 + 67584\beta_4)/L^3$$

$$\begin{aligned}
k_{3,0} &= J (-354816 - 335808\beta_1 - 293568\beta_2 - 264528\beta_3 - 243936\beta_4)/L^3 \\
k_{3,1} &= J (88704 + 85536\beta_1 + 78672\beta_2 + 73392\beta_3 + 69168\beta_4)/L^3 \\
k_{3,2} &= J (126720 + 63360\beta_1 + 47872\beta_2 + 40128\beta_3 + 35328\beta_4)/L^3 \\
k_{3,3} &= J (-190080 - 133056\beta_1 - 114576\beta_2 - 103224\beta_3 - 95232\beta_4)/L^3 \\
k_{3,4} &= J (31680 + 25344\beta_1 + 23848\beta_2 + 22968\beta_3 + 22296\beta_4)/L^3 \\
k_{3,5} &= J (504108 + 410454\beta_1 + 364584\beta_2 + 333720\beta_3 + 311148\beta_4)/L^3 \\
k_{3,6} &= J (-112662 - 100188\beta_1 - 93621\beta_2 - 88671\beta_3 - 84594\beta_4)/L^3 \\
k_{3,7} &= J (32868 + 30195\beta_1 + 28402\beta_2 + 26895\beta_3 + 25572\beta_4)/L^3
\end{aligned}$$

where  $J = EJ_{m-1}/3465$

### 3. TB7

$$\begin{aligned}
m_{11} &= V (17304912 + 1047591\alpha_1 + 130754\alpha_2) \\
m_{12} &= VL (536520 + 46461\alpha_1 + 7663\alpha_2) \\
m_{13} &= V (4420170 + 1036881\alpha_1 + 407025\alpha_2) \\
m_{14} &= VL (-1690956 - 145503\alpha_1 + 20466\alpha_2) \\
m_{15} &= V (4230144 + 1003833\alpha_1 + 505926\alpha_2) \\
m_{16} &= VL (-561816 + 43605\alpha_1 + 98037\alpha_2) \\
m_{17} &= V (1174734 + 587367\alpha_1 + 473239\alpha_2) \\
m_{18} &= VL (-76296 - 29835\alpha_1 - 22172\alpha_2) \\
m_{22} &= VL^2 (21216 + 2295\alpha_1 + 488\alpha_2) \\
m_{23} &= VL (264384 + 70227\alpha_1 + 30618\alpha_2) \\
m_{24} &= VL^2 (-79866 - 5967\alpha_1 + 2403\alpha_2) \\
m_{25} &= VL (231336 + 70227\alpha_1 + 39609\alpha_2) \\
m_{26} &= VL^2 (-22032 + 5967\alpha_1 + 8370\alpha_2) \\
m_{27} &= VL (76296 + 46461\alpha_1 + 38798\alpha_2) \\
m_{28} &= VL^2 (-4590 - 2295\alpha_1 - 1807\alpha_2) \\
m_{33} &= V (48183984 + 17065161\alpha_1 + 6849684\alpha_2) \\
m_{34} &= VL (-892296 + 334611\alpha_1 + 387099\alpha_2) \\
m_{35} &= V (14053662 + 7026831\alpha_1 + 4192479\alpha_2) \\
m_{36} &= VL (-446148 + 334611\alpha_1 + 498636\alpha_2) \\
m_{37} &= V (4230144 + 3226311\alpha_1 + 2728404\alpha_2) \\
m_{38} &= VL (-231336 - 161109\alpha_1 - 130491\alpha_2) \\
m_{44} &= VL^2 (793152 + 210681\alpha_1 + 91854\alpha_2) \\
m_{45} &= VL (446148 + 780759\alpha_1 + 616734\alpha_2) \\
m_{46} &= VL^2 (322218 + 161109\alpha_1 + 129033\alpha_2) \\
m_{47} &= VL (561816 + 605421\alpha_1 + 550989\alpha_2) \\
m_{48} &= VL^2 (-22032 - 27999\alpha_1 - 25596\alpha_2) \\
m_{55} &= V (48183984 + 31118823\alpha_1 + 20903346\alpha_2)
\end{aligned}$$

$$\begin{aligned}
m_{10} &= VL(892296 + 1226907\alpha_1 + 1171419\alpha_2) \\
m_{11} &= V(4420170 + 3383289\alpha_1 + 2753433\alpha_2) \\
m_{12} &= VL(-264384 - 194157\alpha_1 - 154518\alpha_2) \\
m_{13} &= VL^2(793152 + 582471\alpha_1 + 463644\alpha_2) \\
m_{14} &= VL(1690956 + 1545453\alpha_1 + 1379484\alpha_2) \\
m_{15} &= VL^2(-79866 - 73899\alpha_1 - 65529\alpha_2) \\
m_{16} &= V(17304912 + 16257321\alpha_1 + 15340484\alpha_2) \\
m_{17} &= VL(-536520 - 490059\alpha_1 - 451261\alpha_2) \\
m_{18} &= VL^2(21216 + 18921\alpha_1 + 17114\alpha_2)
\end{aligned}$$

where  $V = \rho A_m L / 196035810$

$$\begin{aligned}
k_{11} &= J(934670880 + 76109190\beta_1 + 28088748\beta_2 + 19021014\beta_3 + 16211061\beta_4)/L^3 \\
k_{12} &= J(129575160 + 5900778\beta_1 + 2022066\beta_2 + 1505520\beta_3 + 1330632\beta_4)/L^3 \\
k_{13} &= J(-197026830 + 62106045\beta_1 + 86283711\beta_2 + 86867640\beta_3 + 83043206\beta_4)/L^3 \\
k_{14} &= J(318995820 + 40747941\beta_1 + 23867946\beta_2 + 19998657\beta_3 + 18268740\beta_4)/L^3 \\
k_{15} &= J(-562933800 - 51460110\beta_1 - 29279556\beta_2 - 21926862\beta_3 - 16720344\beta_4)/L^3 \\
k_{16} &= J(150115680 + 44118594\beta_1 + 39776670\beta_2 + 37788444\beta_3 + 36010656\beta_4)/L^3 \\
k_{17} &= J(-174710250 - 87355125\beta_1 - 85092903\beta_2 - 83961792\beta_3 - 82567026\beta_4)/L^3 \\
k_{18} &= J(16988400 + 10092537\beta_1 + 10184688\beta_2 + 10331199\beta_3 + 10422792\beta_4)/L^3 \\
k_{22} &= J(23051808 + 858078\beta_1 + 179520\beta_2 + 123624\beta_3 + 109728\beta_4)/L \\
k_{23} &= J(-51175800 + 3440151\beta_1 + 7119414\beta_2 + 7212726\beta_3 + 6881760\beta_4)/L^2 \\
k_{24} &= J(34856406 + 2448225\beta_1 + 1799253\beta_2 + 1624698\beta_3 + 1507086\beta_4)/L \\
k_{25} &= J(-61410960 - 2445066\beta_1 - 2153466\beta_2 - 1784592\beta_3 - 1388016\beta_4)/L^2 \\
k_{26} &= J(15466464 + 3266406\beta_1 + 3234492\beta_2 + 3118176\beta_3 + 2978208\beta_4)/L \\
k_{27} &= J(-16988400 - 6895863\beta_1 - 6988014\beta_2 - 6933654\beta_3 - 6824376\beta_4)/L^2 \\
k_{28} &= J(1612962 + 806481\beta_1 + 837255\beta_2 + 852642\beta_3 + 860778\beta_4)/L \\
k_{33} &= J(1658095920 + 898135290\beta_1 + 659459232\beta_2 + 547738524\beta_3 + 483257016\beta_4)/L^3 \\
k_{34} &= J(214938360 + 158133222\beta_1 + 127191546\beta_2 + 110697192\beta_3 + 100225836\beta_4)/L^3 \\
k_{35} &= J(-898135290 - 449067645\beta_1 - 256449807\beta_2 - 160140888\beta_3 - 104516730\beta_4)/L^3 \\
k_{36} &= J(383818500 + 290934423\beta_1 + 247454676\beta_2 + 221984874\beta_3 + 204467004\beta_4)/L^3 \\
k_{37} &= J(-562933800 - 511473690\beta_1 - 489293136\beta_2 - 474465276\beta_3 - 461783592\beta_4)/L^3 \\
k_{38} &= J(61410960 + 58965894\beta_1 + 58674294\beta_2 + 58751568\beta_3 + 58801140\beta_4)/L^2 \\
k_{44} &= J(169221312 + 43158258\beta_1 + 28807164\beta_2 + 24026382\beta_3 + 21572568\beta_4)/L \\
k_{45} &= J(-383818500 - 92884077\beta_1 - 49404330\beta_2 - 31394385\beta_3 - 21336372\beta_4)/L^2 \\
k_{46} &= J(114804378 + 57402189\beta_1 + 49419639\beta_2 + 45428364\beta_3 + 42580890\beta_4)/L \\
k_{47} &= J(-150115680 - 105997086\beta_1 - 101655162\beta_2 - 99301464\beta_3 - 97158204\beta_4)/L^2 \\
k_{48} &= J(15466464 + 12200058\beta_1 + 12168144\beta_2 + 12252546\beta_3 + 12313296\beta_4)/L \\
k_{55} &= J(1658095920 + 759960630\beta_1 + 521284572\beta_2 + 394329222\beta_3 + 314613072\beta_4)/L^3 \\
k_{56} &= J(-214938360 - 56805138\beta_1 - 25863462\beta_2 - 11418140\beta_3 - 2991816\beta_4)/L^3
\end{aligned}$$



$$k_{1,7} = J (-197026830 - 259432875\beta_1 - 235555209\beta_2 - 212261472\beta_3 - 193375998\beta_4) / L^3$$

$$k_{1,8} = J (51175800 + 54615951\beta_1 + 50936688\beta_2 + 47350737\beta_3 + 44189064\beta_4) / L^3$$

$$k_{1,9} = J (169221312 + 126063054\beta_1 + 111711960\beta_2 + 102141648\beta_3 + 94898304\beta_4) / L$$

$$k_{1,10} = J (-318995820 - 278247879\beta_1 - 261367884\beta_2 - 248357178\beta_3 - 237485844\beta_4) / L^3$$

$$k_{1,11} = J (34856406 + 32408181\beta_1 + 31759209\beta_2 + 31284792\beta_3 + 30867318\beta_4) / L$$

$$k_{1,12} = J (934670880 + 858261690\beta_1 + 809941248\beta_2 + 770688540\beta_3 + 737726616\beta_4) / L^3$$

$$k_{1,13} = J (-129575160 - 123674382\beta_1 - 119795670\beta_2 - 116433504\beta_3 - 113412996\beta_4) / L^3$$

$$k_{1,14} = J (23051808 + 22193730\beta_1 + 21515172\beta_2 + 20892510\beta_3 + 20311848\beta_4) / L$$

where  $J = EJ_{min} / 1441440$

## V. COMPARISON OF NUMERICAL RESULTS

In order to compare the results obtained using the conforming elements with those using the excessively conforming elements and to examine the effect of the imposed boundary conditions, we calculated the natural vibration characteristics of six types of rectangular cross-sectional linear tapered beams under certain support conditions. Due to the limitation of pages, the following is a list of some typical results. In Tables 1 to 6, part of the results of suspending arm beam, double ended simple support beam and double ended fixed support beam with dimensionless angular frequency  $\bar{\omega} = \omega l^2 \sqrt{\rho A / EJ}$  are presented where  $\rho A$  and  $EJ$  are parameters of the cross-section at the bottom of the beam. In those tables  $\alpha$  and  $\beta$  represent the cross-sectional width to height ratio at the tip and the bottom, respectively. NE represents the number of elements used. NF represents the net total degree of freedom. The bracket represents the results of the excessively conforming elements after the imposition of boundary conditions [3]. In Tables 7 to 9, part of the vibration mode results obtained using TB7 to calculate the suspending arm beam are given. Tables 7 and 8 give the conditions at the two extremes, respectively. They are the nodal parameters at the cross-sections on the bottom, in the middle and at the end of the first and second orders of the dimensionless vibration modes for conical and even suspending arm beams. In Table 9, the results of fifth order dimensionless vibration mode at various cross-sections are given. On the cross-section where two elements are next to each

other, two second and third order derivative values obtained according to different elements are given in order to compare the continuity of the higher order derivatives.

TABLE 1. NATURAL FREQUENCY OF CONICAL SUSPENDING ARM BEAM  $\alpha=\beta=0$

1 元素	NE	NF	2 一 阶	3 二 阶	4 三 阶	5 四 阶	6 五 阶
TB3	1	2	8.73517	25.18142			
(TB5)	1	3	8.74506	23.18407	68.85968		
TB5	1	4	8.71926	21.18104			
(TB7)	1	4	8.75096	22.83025	55.37000	169.39409	
(TB7)	1	6	8.71926	21.14567	38.46463	62.03181	109.1810
TB7	1	6	8.71926	21.14567	38.46463	62.03181	109.1810
TB3	2	4	8.72388	21.71782	41.92455	94.86600	
(TB5)	2	6	8.72021	21.25307	40.39639	72.27633	128.51948
TB5	2	8	8.71926	21.14598	38.47467	61.27990	91.47960
(TB7)	2	8	8.72089	21.27920	40.25180	70.13591	117.87538
(TB7)	2	10	8.71926	21.14566	38.45379	60.68294	87.91506
TB7	2	12	8.71926	21.14566	38.45378	60.68098	87.91129
TB5	3	12	8.71926	21.14568	38.45548	60.71451	88.37100
(TB7)	3	14	8.71926	21.14566	38.45377	60.68021	87.83591
TB7	3	18	8.71926	21.14566	38.45377	60.68016	87.83170
TB3	4	8	8.71961	21.20345	39.10222	62.76943	98.77109
(TB5)	4	12	8.71927	21.14939	38.54472	61.57121	92.29457
TB5	4	16	8.71926	21.11566	38.45104	60.68801	87.89500
(TB7)	4	16	8.71936	21.15169	38.57220	61.60905	91.70001
(TB7)	4	18	8.71926	21.14566	38.45377	60.68011	87.83108
TB7	4	24	8.71926	21.14566	38.45377	60.68011	87.83101
7 正 确 解			8.7192	21.146	38.453		

Key: 1--element; 2--first order; 3--second order; 4--third order; 5--fourth order; 6--fifth order; 7--accurate solution

TABLE 2. NATURAL FREQUENCY OF THE UNIFORM SUSPENDING ARM  
BEAM  $\alpha=\beta=1.0$

元 素	NE	NF	一 阶	二 阶	三 阶	四 阶	五 阶
TB3	1	2	3.53270	34.80861			
(TB5)	1	3	3.51602	22.22655	64.76539		
TB5	1	4	3.51602	22.15783			
(TB7)	1	1	3.51602	22.03545	61.76748	136.2812	
(TB7)	1	6	3.51602	22.03480	61.71629	128.3893	223.5514
TB7	1	6	3.51602	22.03480	61.71629	128.3893	223.5514
TB3	2	4	3.51772	22.22151	75.15707	218.1381	
(TB5)	2	6	3.51602	22.03474	61.87149	123.2772	206.4655
TB5	2	8	3.51602	22.03464	61.78096	122.5857	203.8610
(TB7)	2	8	3.51602	22.03449	61.69745	120.9381	200.0271
(TB7)	2	10	3.51602	22.03449	61.69735	120.9184	199.9074
TB7	2	12	3.51602	22.03449	61.69731	120.9101	199.9062
TB5	3	12	3.51602	22.03450	61.69820	120.9983	200.6371
(TB7)	3	14	3.51602	22.03449	61.69721	120.9020	199.8626
TB7	3	18	3.51602	22.03449	61.69721	120.9020	199.8615
TB3	4	8	3.51613	22.06019	62.17492	122.6580	228.1377
(TB5)	4	12	3.51602	22.03449	61.69753	120.9065	200.1347
TB5	4	16	3.51602	22.03449	61.69742	120.9047	199.9800
(TB7)	4	16	3.51602	22.03449	61.69719	120.9022	199.8597
(TB7)	4	18	3.51602	22.03449	61.69721	120.9019	199.8597
TB7	4	24	3.51602	22.03449	61.69721	120.9019	199.8596
7 正 确 解			3.51602	22.03449	61.69717	120.9019	199.8595

Key: 1--element; 2--first order; 3--second order; 4--third order;  
5--fourth order; 6--fifth order; 7--accurate solution

TABLE 3. NATURAL FREQUENCY OF THE DOUBLE END SIMPLE SUPPORT  
CONICAL BEAM  $\alpha=\beta=0$

1	元 素	NE	NF	2 一 阶	3 二 阶	4 三 阶	5 四 阶	6 五 阶
	TB5	1	4	2.08544	19.96628			
	(TB7)	1	6	1.47084	17.40871			
	TB7	1	6	1.47084	17.40871			
	TB5	2	8	1.37526	17.71500	37.27740	68.07741	120.3690
	(TB7)	2	10	1.02854	16.36602	34.51085	59.21249	92.64939
	TB7	2	12	1.00260	16.31783	34.36167	58.82510	91.55358
	TB5	3	12	1.09878	16.50460	34.96012	60.47547	95.45769
	(TB7)	3	12	1.28687	16.90177	36.06196	62.51789	97.86165
	(TB7)	3	14	0.829911	16.02976	33.50046	56.88121	86.22648
	TB7	3	18	0.809006	15.99869	33.41023	56.47287	85.78722
	TB5	4	16	0.941530	16.21001	34.03882	57.99904	89.24791
	(TB7)	4	18	0.714344	15.86809	33.03487	55.61990	84.01120
	TB7	4	24	0.696516	15.81537	32.97026	55.47633	83.72831

Key: 1--element; 2--first order; 3--second order; 4--third order;  
5--fourth order; 6--fifth order

TABLE 4. NATURAL FREQUENCY OF DOUBLE END SIMPLE SUPPORT  
TAPERED BEAM  $\alpha=0, \beta=1$

1	元 素	NE	NF	2 一 阶	3 二 阶	4 三 阶	5 四 阶	6 五 阶
	TB5	1	4	9.26806	39.35791			
	(TB7)	1	6	9.26775	39.14187			
	TB7	1	6	9.26775	39.14187			
	TB5	2	8	9.26775	39.14383	88.69302	158.5249	258.8534
	(TB7)	2	10	9.26775	39.14024	88.51708	157.6319	247.0560
	TB7	2	12	9.26775	39.14024	88.51688	157.6271	246.6728
	TB5	3	12	9.26775	39.14032	88.52866	157.7543	247.6269
	(TB7)	3	12	9.27175	39.17198	88.62429	157.8775	246.9732
	(TB7)	3	14	9.26775	39.14024	88.51651	157.6204	246.1670
	TB7	3	18	9.26775	39.14024	88.51651	157.6203	246.1600
	TB5	4	16	9.26775	39.14025	88.51724	157.6465	246.5850
	(TB7)	4	18	9.26775	39.14024	88.51651	157.6201	246.1560
	TB7	4	24	9.26775	39.14024	88.51651	157.6201	246.1560

Key: 1--element; 2--first order; 3--second order; 4--third order;  
5--fourth order; 6--fifth order

TABLE 5. NATURAL FREQUENCY OF DOUBLE END FIX SUPPORT  
CONICAL BEAMS  $\alpha=\beta=0$

元 素	NE	NF	一 阶	二 阶	三 阶	四 阶	五 阶
TB5	1	2	15.67724	61.88788			
(TB7)	1	4	11.85050	33.01927			
TB7	1	4	11.85050	33.01927			
TB5	2	6	11.42549	30.88580	64.23691	121.2606	228.3332
(TB7)	2	8	10.23016	26.35448	51.02326	86.95781	139.8448
TB7	2	10	10.15240	26.07759	50.28704	85.03259	134.9419
TB5	3	10	10.43559	27.07015	52.76716	90.03410	143.1205
(TB7)	3	12	9.70621	24.52313	46.36655	76.10099	115.2326
TB7	3	16	9.65592	24.35079	45.95214	75.23542	113.4546
TB5	4	14	9.98151	25.46343	48.62850	80.68925	123.1514
(TB7)	4	16	9.45322	23.66025	44.31312	71.90778	107.1181
TB7	4	22	9.41629	23.53479	44.01933	71.32913	106.0614

Key: 1--element; 2--first order; 3--second order; 4--third order;  
5--fourth order;; 6--fifth order

TABLE 6. NATURAL FREQUENCY OF UNIFORM DOUBLE END FIX SUPPORT  
BEAMS  $\alpha=\beta=1.0$

元 素	NE	NF	一 阶	二 阶	三 阶	四 阶	五 阶
TB5	1	2	22.41994	62.92853			
(TB7)	1	4	22.37375	61.69325			
TB7	1	4	22.37375	61.69325			
TB5	2	6	22.37331	61.73254	122.2430	202.8946	321.8728
(TB7)	2	8	22.37329	61.67299	120.9226	199.9169	300.6265
TB7	2	10	22.37329	61.67295	120.9129	199.9154	299.0739
TB5	3	10	22.37330	61.67315	120.9808	200.4706	303.3462
(TB7)	3	12	22.37329	61.67282	120.9035	199.8631	298.6645
TB7	3	16	22.37329	61.67282	120.9035	199.8618	298.5915
TB5	4	14	22.37329	61.67299	120.9047	199.9619	299.0478
(TB7)	4	16	22.37329	61.67282	120.9034	199.8596	298.5575
TB7	4	22	22.37329	61.67282	120.9034	199.8596	298.5567

Key: 1--element; 2--first order; 3--second order; 4--third order;  
5--fourth order; 6--fifth order

TABLE 7. FIRST ORDER VIBRATION MODE OF A SUSPENDING CONICAL BEAM  $\alpha=\beta=0$

1 橫 面		NE	1	2	4	6
		NF	6	12	18	24
2 根 部	$l^2 \frac{d^2 w}{dx^2}$		0.88865	0.88865	0.88865	0.88865
	$l^3 \frac{d^3 w}{dx^3}$		1.87570	1.87558	1.87557	1.87557
3 中 部	$w$			0.16318	0.16318	0.16318
	$l \frac{dw}{dx}$			0.78686	0.78686	0.78686
	$l^2 \frac{d^2 w}{dx^2}$			2.51524	2.51524	2.51524
	$l^2 \frac{d^2 w}{dx^2}$			2.51524	2.51524	2.51524
	$l^3 \frac{d^3 w}{dx^3}$			4.97500	4.97504	4.97504
	$l^3 \frac{d^3 w}{dx^3}$			4.97504	4.97504	4.97504
4 自由端	$w$		1.	1.	1.	1.
	$l \frac{dw}{dx}$		2.87613	2.87615	2.87615	2.87615
	$l^2 \frac{d^2 w}{dx^2}$		6.33503	6.33545	6.33546	6.33546
	$l^3 \frac{d^3 w}{dx^3}$		10.92723	10.93281	10.93303	10.93303

Key: 1--cross-section; 2--bottom; 3--middle; 4--free end

TABLE 8. SECOND ORDER VIBRATION MODE OF SUSPENDING CONICAL BEAMS  $\alpha=\beta=0$

截面		NE	1	2	4	6
		NF	6	12	24	36
2 底部	$12 \frac{d^2 w}{dx^2}$		-0.73545	-0.73402	-0.73396	-0.73396
	$13 \frac{d^3 w}{dx^3}$		-0.32855	-0.38935	-0.39472	-0.39488
3 中部	$w$			-0.06074	-0.06074	-0.06074
	$1 \frac{dw}{dx}$			-0.03363	-0.03363	-0.03363
	$12 \frac{d^2 w}{dx^2}$			2.15214	2.15235	2.15235
	$13 \frac{d^3 w}{dx^3}$			2.15233	2.15235	2.15235
	$13 \frac{d^3 w}{dx^3}$			19.55613	19.57092	19.57136
	$13 \frac{d^3 w}{dx^3}$			19.57563	19.57183	19.57148
4 自由端	$w$		1.	1.	1.	1.
	$1 \frac{dw}{dx}$		7.04008	7.05085	7.05102	7.05102
	$12 \frac{d^2 w}{dx^2}$		37.00994	37.25440	37.26144	37.26157
	$13 \frac{d^3 w}{dx^3}$		153.99387	157.44318	157.63147	157.63630

Key: 1--cross-section; 2--bottom; 3--middle; 4--free end

TABLE 9. FIFTH ORDER VIBRATION MODE OF SUSPENDING  
CONICAL BEAMS NE=6, NF=36

$x/l$	0	1/6	2/6	3/6	4/6	5/6	1
$w$	0.	0.0047	0.0035	-0.0100	0.0118	-0.0271	1.0
$1 \frac{dw}{dx}$	0.	0.0354	-0.0649	-0.0312	0.2301	-0.8614	29.27
$1^2 \frac{d^2w}{dx^2}$	0.5197	-0.2131	-0.7168	1.579	-1.017	-1.212	612.2
$1^2 \frac{d^2w}{dx^2}$		-0.2131	-0.7169	1.578	-1.019	-1.231	
$1^3 \frac{d^3w}{dx^3}$	-2.171	-6.095	3.864	17.99	-74.02	121.5	11235
$1^3 \frac{d^3w}{dx^3}$		-6.105	3.854	18.18	-72.60	125.7	

Based on the numerical results, we can obtain the following conclusions:

1. When the same number of elements is used, higher order elements always have better convergence of low order elements. Even when only one TB7 element is used, we can get the frequency value with pretty high accuracy. However, under the conditions that few elements are used and the taper is deep, the results obtained using high order elements are not as good as those using low order elements after boundary conditions are imposed. In addition, conforming elements always bring about better results than excessively conforming elements, especially for beams with deep tapers.

2. For the same net number of degree of freedom, the results obtained using conforming high order elements are also better than those using conforming low order elements. Under the conditions that the beams are tapered, the results of conforming high order elements are better than those of excessively conforming elements after the boundary conditions are imposed. When the beam is relatively more uniform, although the latter gives better results yet



the difference is very small. If we consider that only fewer elements are required for high order conforming elements to reach the same total number of degree of freedom and the average bandwidth is also narrower, it still has its advantages. But, if boundary conditions are not imposed, then for beams with sudden changes in characteristics the results of excessively conforming elements are going to be better than those of conforming elements. It is interesting to note that this difference increases as the degree of taper increases.

3. [3] speculated that sometimes the results of high order elements are poor due to the taper in the beam. We believe that this is only a superficial cause. Since boundary conditions exceeding the requirements of the variational principle were imposed in [3], we believe that it is the true reason why the results become poor.

4. The most controversial point of the conforming elements is that higher order derivatives may not be continuous at the neighboring point between two elements. But from Tables 7 and 8, we can see that only few TB7 elements can satisfy the continuity requirements of the high order derivatives of first and second order vibration modes with sufficient accuracy. Even for fifth order vibration modes, as shown in Table 9, as long as the number of total degree of freedom is maintained at 7 to 8 times that of the number of order, then the continuity of high order derivatives can still be satisfied very well. On the other hand, we can estimate the accuracy of the calculated results from the degree that the continuity is satisfied. It is not necessary to carry out the checking through the increase of the number of elements used. Apparently, the latter method is more time consuming. Using excessively conforming elements, although superficially the continuity of the high order derivatives can be maintained, yet based on the characteristics of the Rayleigh quotient we know that the deviation of the vibration mode is greater than that

of the frequency by one order of magnitude. If its frequency deviation is greater than that of the conforming elements, then its vibration mode actually is going to be greater than that of the conforming elements.

The results for other support conditions indicate that the above conclusions are also valid. Therefore, by summarizing the above situation and considering that beams in actual engineering very frequently have some kind of discontinuity, we believe that the use of high order conforming elements is even worthwhile recommending and boundary conditions should not be imposed.

#### REFERENCES

- [1] G. M. Lindberg, 1963 Aeronautical Quarterly 14, 387-395.  
Vibration of non-uniform beams.
- [2] J. Thomas and E. Dokumaci, 1973 Aeronautical Quarterly, 24, 39-46. Improved finite elements for vibration analysis of tapered beams.
- [3] C. W. S. To, 1979 Journal of Sound and Vibration 63, 33-50. Higher order tapered beam finite elements for vibration analysis.
- [4] Hu High Chang, Theory and Application of Variational Principle in Elastic Mechanics, pp 94-96, 1978 published by Beijing Institute of Aeronautics and Astronautics (the book will be officially published by Science Publishers).
- [5] P. Tong and J. N. Rossettos, 1977, 164 Finite-Element Method (Basic technique and implementation), MIT Press.

### Abstract

The explicit expressions for the stiffness and mass matrices of the tapered beam conforming elements with displacement functions based on the 3rd, 5th and 7th order polynomial respectively are given, and a general method for evaluating the stiffness and mass matrices of even higher order beam element with arbitrary odd power is also developed. Then by means of these elements are calculated the first five natural frequencies and corresponding modes of these elements are calculated the first five natural frequencies and corresponding modes of the linearly tapered beams with rectangular cross section in six manners under various boundary conditions (e. g. fixed-fixed, simply supported-simply supported, cantilever, etc.) Numerical results are presented for several typical cases. The results indicate that the higher order element exhibits better convergence than the lower order element in all cases without imposition of natural boundary conditions. Otherwise the higher order element would lead to worse results than the lower order element for deeply tapered beams with a few elements used in calculation. Hence, it may be concluded that the reason for the worse convergence of the higher order element in some cases is the imposition of the natural boundary conditions in advance, but it is not necessary for the displacement variational principle.

CALCULATION OF INTERNAL AND EXTERNAL FLOW FIELD AND COWL PRESSURE  
DRAG IN THE SUPERSONIC AXISYMMETRIC NOSE INLETS

Power Plant Research Laboratory, Beijing Research Institute,  
Precision Machinery Corporation of China

Zhou Weimin and Xia Suiwen

ABSTRACT

In order to calculate the flow field of the supersonic axisymmetric nose inlet, a general program is compiled using the finite difference method. This program is suitable for the direct problem of aerodynamic design of inlets such as the pitot-type, single cone, bi-cone, triple cone, and isentropic cone, etc. Because in the calculation of inviscid flow field in the let "separation singularity" difference method and implicit-explicit difference scheme are used, results of calculation obtained reach a second order accuracy at boundary points, internal points and near singular points. This program can provide the required internal and external flow characteristics in the inlet.

This paper lists five examples and compares the results obtained using the characteristic line method and the experimental results. The extent of agreement is satisfactory.

---

Received in April, 1980

# TABLE OF SYMBOLS

$L$	--characteristic length
$Z$	--axial component of the cylindrical coordinate system (relative to $L$ )
$R$	--radial component of the cylindrical coordinate system (relative to $L$ )
$V_{\infty}$	--velocity of incoming flow from a distance ahead
$\rho_{\infty}$	--density of incoming flow from a distance ahead
$u$	--velocity component in the $Z$ direction (relative to $V_{\infty}$ )
$v$	--velocity component in the $R$ direction (relative to $V_{\infty}$ )
$p$	--static pressure (relative to $\rho_{\infty} V_{\infty}^2$ )
$p_{\infty}$	--static pressure of incoming flow from a distance ahead
$p_{0\infty}$	--total pressure of incoming flow from a distance ahead
$\rho$	--density (relative to $\rho_{\infty}$ )
$a$	--speed of sound (relative to $V_{\infty}$ )
$C_{da}$	--added drag coefficient per unit area
$C_{dp}$	--total cowl pressure drag coefficient (relative to the inlet area)
$C_p$	--pressure coefficient
$F_H$	--flow flux coefficient of the inlet
$LM$	--total number of boundaries in the flow field
$M_1$	--Mach number in front of the compression angle or the expansion angle
$M_2$	--Mach number after the compression angle wave
$\bar{p}$	-- $p/r$
$\bar{p}_0$	--ratio of local total pressure to total incoming flow pressure
$R_0$	--inlet radius of exponent type of cowl
$R_{max}$	--outlet radius of exponent type of cowl
$\bar{Z}$	--the ratio of $Z$ to the total length of the cowl for exponent type of cowl
$\theta$	--angle between the direction of the flow and the $Z$ axis
$\beta_1$	--angle between the direction of flow before the compression angle shock wave and the $Z$ axis
$\beta_2$	--angle between the direction of flow after the compression angle shock wave and the $Z$ axis

$\epsilon_0$ --angle between compression angle shock wave and the direction of flow in front of the wave

$\alpha$ --exponent in Equation (13)

$p_B$ --tangential interrupted lower side pressure

$p_U$ --tangential interrupted upper side pressure

## I. INTRODUCTION

Supersonic inlet is an important part of a jet engine. It has great influence on the function of the combustion chamber and the propulsion of the engine. In general, a great deal of accurate flow field calculation must be used to determine its aerodynamic characteristics. The aerodynamic shape is chosen by comparing the internal and external characteristics.

In other countries, the classic method to calculate the inviscid flow field of the supersonic inlets is the method of characteristics [1,2]. However, we have not yet seen any published information on the calculation of cowl pressure drag under non-design conditions. We considered the fact that in the calculation of the external flow field of the cowl we must solve the singular point problems at the interceptions of various types of interrupted surfaces. It is not easy to treat these problems using the method of characteristics. Therefore, we chose the difference method proposed by Chu Youyeh [3] and compiled the computation program for the supersonic inviscid internal and external flow fields at zero attack angle (domestic 111 machine BCY language) to satisfactorily solve the computational problem of the entire flow field. Regardless whether it is on the boundaries, at the internal points, and near the singular points, the accuracy all reaches the second order and it saves computer time. Using this program, it is possible to simultaneously calculate the internal and external flow fields of the inlets and internal flow and external drag characteristics which is very practical in the design and model selection of the inlets.

## II. BRIEF DESCRIPTION OF THE NUMERICAL METHOD

The difference method proposed by Chu Youyeh [3] adopts a curvilinear coordinate system which makes all the necessary boundaries (including various breaks) the coordinates. Accurate interruption conditions are used to leap over breaks so there is no difference at the breaks. In the meantime, the mixed use of implicit-explicit difference scheme has the advantages of smaller break error, larger allowable step and higher accuracy.

### 1. Basic equations and boundary conditions

In the cylindrical coordinate system, the equations to describe inviscid thermally nonconductive axisymmetric steady turbulent flow are:

$$\begin{cases} u \frac{\partial u}{\partial Z} + v \frac{\partial u}{\partial R} + \frac{1}{\rho} \frac{\partial p}{\partial Z} = 0 \\ u \frac{\partial v}{\partial Z} + v \frac{\partial v}{\partial R} + \frac{1}{\rho} \frac{\partial p}{\partial R} = 0 \\ \rho \left( \frac{\partial u}{\partial Z} + \frac{\partial v}{\partial R} \right) + u \frac{\partial \rho}{\partial Z} + v \frac{\partial \rho}{\partial R} + \frac{v \rho}{R} = 0 \\ u \frac{\partial \rho}{\partial Z} + v \frac{\partial \rho}{\partial R} - u \left( u \frac{\partial \rho}{\partial Z} + v \frac{\partial \rho}{\partial R} \right) = 0 \end{cases} \quad (1)$$

Introducing a new coordinate system  $\xi, \eta$  and the transformation equations are:

$$\begin{cases} Z = \eta \\ R = F_l(\eta) + \xi_l [F_{l+1}(\eta) - F_l(\eta)] \end{cases}$$

where  $l = 1, 2, \dots, LM-1$ ,

$l$ --zone symbol

$F_l$ --boundaries of characteristic lines divided by the shock wave, tangential breaks, surfaces of objects in the flow field.

In the new coordinate system, the calculated zone is a rectangular area and Equations (1) become:

$$A \frac{\partial X}{\partial \eta} + B \frac{\partial X}{\partial \xi} = D \quad (2)$$

where

$$X = \begin{bmatrix} u \\ v \\ p \\ \rho \end{bmatrix}, \quad D = \begin{bmatrix} 0 \\ 0 \\ -\rho v/R \\ 0 \end{bmatrix}$$

$$A = \begin{bmatrix} V_n & 0 & \eta_z/\rho & 0 \\ 0 & V_n & \eta_k/\rho & 0 \\ \rho \eta_z & \rho \eta_k & 0 & V_n \\ 0 & 0 & V_n & -a^2 V_n \end{bmatrix}, \quad B = \begin{bmatrix} V_t & 0 & \xi_z/\rho & 0 \\ 0 & V_t & \xi_k/\rho & 0 \\ \rho \xi_z & \rho \xi_k & 0 & V_t \\ 0 & 0 & V_t & -a^2 V_t \end{bmatrix}$$

$$V_n = \vec{\eta} \cdot \vec{v}, \quad V_t = \vec{\xi} \cdot \vec{v}, \quad \vec{v} = \begin{bmatrix} u \\ v \end{bmatrix}, \quad \vec{\xi} = \begin{bmatrix} \xi_z \\ \xi_k \end{bmatrix}$$

$$\vec{\eta} = \begin{bmatrix} \eta_z \\ \eta_k \end{bmatrix}, \quad \eta_z = \frac{\partial \eta}{\partial Z}, \quad \eta_k = \frac{\partial \eta}{\partial R}, \quad \xi_z = \frac{\partial \xi}{\partial Z}, \quad \xi_k = \frac{\partial \xi}{\partial R}$$

Equations (2) are a set first order quasi-linear hyperbolic equations with two variables. In order to make the format and accuracy of the boundary points the same as those of the internal points, we used the equations compatible with Equations (2) as the basic equations in the calculation. On the basis of the definition of compatible equation:

$$U \left( \frac{\partial X}{\partial \eta} + \lambda \frac{\partial X}{\partial \xi} \right) = \overline{M} \quad (3)$$

where



$$\bar{\lambda} = \begin{bmatrix} \lambda_1 & 0 & 0 & 0 \\ 0 & \lambda_2 & 0 & 0 \\ 0 & 0 & \lambda_3 & 0 \\ 0 & 0 & 0 & \lambda_4 \end{bmatrix}, \quad \bar{M} = \begin{bmatrix} a^2 \rho v / R \\ 0 \\ 0 \\ a^2 \rho v / R \end{bmatrix}$$

$$U = \begin{bmatrix} g_1^* & g_2^* & g_3^* & 0 \\ V_{1u} & V_{1v} & V_{1\rho} & 0 \\ 0 & 0 & V_1 & -a^2 V_1 \\ g_1^* & g_2^* & g_3^* & 0 \end{bmatrix}, \quad \lambda_1 = \frac{\beta_1 \pm \sqrt{\beta_2^2 - \beta_1 \beta_3}}{\beta_1}, \quad \lambda_2 = V_1 / V_1,$$

$$\beta_1 = V_1^2 - a^2 \bar{\eta} \cdot \bar{\eta}, \quad \beta_2 = V_1 V_1 - a^2 \bar{\xi} \cdot \bar{\eta}, \quad \beta_3 = V_1^2 - a^2 \bar{\xi} \cdot \bar{\xi}$$

$$\bar{g}^* = \begin{bmatrix} g_1^* \\ g_2^* \end{bmatrix} = \rho a (V_1 \bar{N}^* - a \bar{\eta}), \quad g_1^* = a \bar{N}^* \cdot \bar{\eta} - V_1,$$

$$\bar{N}^* = (V_1 N_1^{*2} + V_1 N_2^{*2}) (N_1^{*2} \bar{\xi} + N_2^{*2} \bar{\eta}) / a$$

$$N_1^{*2} = (\bar{\xi} \cdot \bar{\xi} - 2 \lambda_2 \bar{\xi} \cdot \bar{\eta} + \lambda_2^2 \bar{\eta} \cdot \bar{\eta})^{-1/2}, \quad N_2^{*2} = -\lambda_2 N_1^{*2}$$

It should be pointed out in the derivation Bernoulli's constant is not used.

Boundary conditions: On the boundary of object surface, the condition that the velocity in the normal direction is zero is satisfied. On the shock wave boundary, the relations derived from the dynamics on the interruption surfaces are satisfied. On the tangential broken boundary, the conditions that the pressure is equal on both sides and the direction of the velocity is the same but the magnitude is different are all satisfied. On the boundaries of the characteristics, the slope and velocity relation is satisfied.

## 2. The difference format and the solution of the series of difference equations--a brief introduction

The difference format and the method of solving the difference equations used in the paper originate from [3]. Due to the limitation of available page numbers, only a brief introduction is given here.

Let us assume that the lattice distances in the  $\eta$  and  $\xi_1$  directions are  $\Delta\eta$  and  $\Delta\xi_1$  ( $l=1, 2, \dots, LM-1$ ), respectively. Let us use  $f_{lm}$  to represent the value of the function  $f$  at  $\eta = K\Delta\eta$ ,  $\xi_1 = m\Delta\xi_1$  (in the following description, the subscript 1 is omitted in the areas where no confusion results). Two steps of calculation are required for each step of progress in the  $Z$  direction. The first step is to obtain the value at  $\eta + \frac{1}{2}\Delta\eta$  from the value at  $\eta$  which is called the transition layer. The second step is to obtain the value at  $\eta + \Delta\eta$  from those at  $\eta$  and  $\eta + \frac{1}{2}\Delta\eta$  which is called the regular layer. The formats are of implicit and explicit types and both are second order two-step schemes.

(1) Difference format: Let us write any one of the equations in (3) as

$$u^* \left( \frac{\partial X}{\partial \eta} + \lambda \frac{\partial X}{\partial \xi} \right) = b$$

where  $u^*$  is a four-dimensional row vector,  $X$  is still a four-dimensional column vector,  $b$  is a pure quantity and  $\lambda$  is either  $\lambda_+$ ,  $\lambda_-$ , or  $\lambda_2$ .

Let us introduce the following symbols:

$$T_n^{\pm} \equiv \lambda_n^{\pm} \Delta\eta / \Delta\xi, \quad T_n^{\pm} \equiv \lambda_{n \pm 1/2}^{\pm} \Delta\eta / \Delta\xi, \quad T_{n+1}^{\pm} \equiv \lambda_{n+1}^{\pm} \Delta\eta / \Delta\xi, \\ T_{n+1}^{\pm} \equiv \lambda_{n+1/2}^{\pm} \Delta\eta / \Delta\xi$$

A. Implicit scheme at the transition layer.

$$u_{n+1/2}^* \{ (1 - T_n^{\pm}) X_{n+1/2-1/2}^{\pm} + (1 + T_n^{\pm}) X_{n+1/2+1/2}^{\pm} \} \\ = \Delta\eta b_{n+1/2}^{\pm} + u_{n+1/2}^* (X_{n+1/2-1/2}^{\pm} + X_{n+1/2+1/2}^{\pm}) \quad (4)$$

In this equation and the following equations, whenever the symbol " $\mp$ " occurs, if  $\lambda > 0$  then choose the upper symbol and if  $\lambda < 0$ , then choose the lower symbol.

B. Implicit scheme at the regular layer:

$$\begin{aligned}
& u_m^{K+1/2} [(1 - T_m^{K+1/2}) X_{m+1/2-1/2}^K + (1 + T_m^{K+1/2}) X_{m+1/2+1/2}^K] \\
& = 2\Delta\eta b_{m+1/2}^K + u_m^{K+1/2} [(1 - T_m^{K+1/2}) X_{m+1/2-1/2}^K + (1 + T_m^{K+1/2}) X_{m+1/2+1/2}^K]
\end{aligned} \quad (5)$$

C. Explicit scheme at the transition layer:

$$u_m^K X_m^{K+1/2} = \frac{1}{2} \Delta\eta b_m^K + u_m^K \left[ \left(1 + \frac{1}{2} T_m^K\right) X_m^K + \frac{1}{2} T_m^K X_{m+1}^K \right] \quad (6)$$

D. Explicit scheme at the regular layer:

$$u_m^{K+1/2} X_m^{K+1} = \Delta\eta b_{m+1/2}^K + u_m^{K+1/2} (X_{m+1/2}^K - (T_m^{K+1/2} + 1)(X_{m+1/2-1/2}^{K+1/2} - X_{m+1/2+1/2}^{K+1/2})) \quad (7)$$

In addition, on the basis of Equation (7), a transition scheme whose coefficients always vary smoothly is formed as described in detail in [3].

E. Transition layer format in the calculation of the boundary  $F_1$

$$F_l^{K+1/2} = F_l^K + \left( \frac{dF_l}{d\eta} \right)^K \frac{\Delta\eta}{2} \quad (8)$$

F. Regular layer format in the calculation of the boundary  $F_1$

$$F_l^{K+1} = F_l^K + \left( \frac{dF_l}{d\eta} \right)^{K+1/2} \Delta\eta \quad (9)$$

(2) Methods to solve the difference equation in various zones.

According to the types of boundary, there are eight kinds of computational zones. For each zone, based on the method used in [3], we separate Equation (3) into three groups according to the magnitude of  $|\lambda|$  to establish the format and to form and to solve the set of difference equations for the zone. In order to ensure the stability of the difference format, the implicit format can only be used for  $|\lambda| \geq \epsilon > 0$  and the explicit format can only be used for  $|\lambda| \leq \epsilon \leq \Delta\xi/\Delta\eta$  (in the calculation  $\epsilon$  is  $10^{-4}$  or  $0.9 \Delta\xi/\Delta\eta$ ).

When the entire set of equations are explicit, they can be solved directly. Otherwise, it is necessary to impose the boundary conditions for various zones and then to seek for the solution according to the "matrix tracing method for the unclosed linear algebraic equation set" proposed in [3]. Naturally, in some types of zones the solution method can be simplified. It is not going to be further discussed here.

### III. CALCULATION OF SINGULAR POINT NEIGHBORING AREAS

In the flow field of supersonic nose gas inlet, there are multiple solutions in some points. Sometimes it is even infinite. This program satisfactorily resolved the problem of computing the neighboring areas of these singular points.

(1) Compression angle: when the air flow meets a concave turning angle, a shock wave is created as shown in Figure 1. We used the following third order equation to obtain the initial slope  $\text{tg} \epsilon_0$  of this shock wave by letting  $x = \text{tg} \epsilon$  :

$$x^3 + A_1 x^2 + A_2 x + A_3 = 0 \quad (10)$$

where  $A_1 = A_2(1 + M_1^2)$ ,  $A_2 = (5 + 6M_1^2)/(5 + M_1^2)$ ,  $A_3 = 5/(5 + M_1^2)/\text{tg}(\beta_2 - \beta_1)$

Newtonian iteration method can be used to search for the roots of Equation (10). The initial value used is the characteristic line corresponding to  $M_1$ . After  $\text{tg} \epsilon_0$  is obtained, the other parameters behind the wave can be determined according to the relations of parameters in front and behind the shock wave.

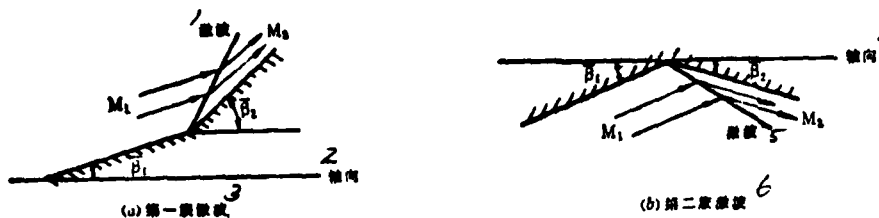


Figure 1. Compression angle

Key: 1--shock wave; 2--axial direction; 3--the first family of shock waves; 4--axial direction; 5--shock wave; 6--second family of shock waves

(2) Expansion angle: When the gas flow runs into a convex turning angle, a center expansion wave is created as shown in Figure 2. The flow parameters in the expansion region fluctuate violently. A slight mishandling in the process will easily cause the accuracy to decrease drastically. We obtained very good calculation accuracy based on the following method.

When the calculation progresses to the expansion angle, the program immediately provides a signal to add two characteristic boundaries in the flow field whose slopes are:

$$\operatorname{tg} \delta_1 = \pm \operatorname{tg} \left( \arcsin \frac{1}{M_1} \right), \quad \operatorname{tg} \delta_2 = \operatorname{tg} \left( \delta \pm \arcsin \frac{1}{M_2} \right) \quad (11)$$

where  $\delta = \pm(\alpha_2 - \alpha_1)$ ,  $M_2 = \sqrt{1 + \beta_2^2}$ ,  $\beta_2$  is obtained using the Newtonian iteration method for the following equation:

$$\arctg(K_1 \beta_2) - K_1 \arctg \beta_2 \pm K_1 \delta + c = 0 \quad (12)$$

where  $K_1 = \sqrt{1/6}$ ,  $c = -\arctg(K_1 \beta_1) + K_1 \arctg \beta_1$ ,  $\beta_1 = \sqrt{M_1^2 - 1}$ . In Equations (11) and (12), "+" corresponds to Figure 2a and "-" corresponds to Figure 2b.

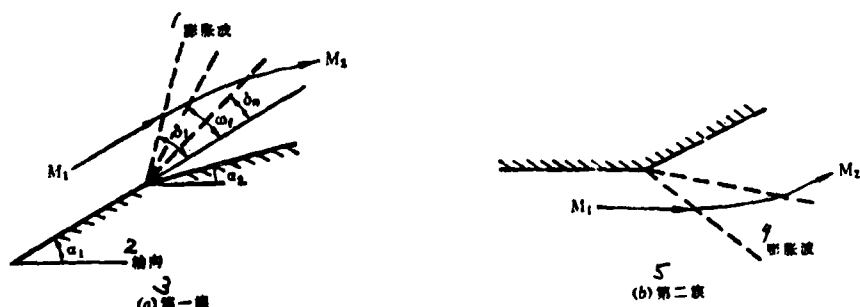


Figure 2. The expansion angle

Key: 1--expansion wave; 2--axial direction; 3--the first family; 4--expansion wave; 5--the second family

In order to obtain the parameters of the corresponding radial lines in the expansion region within the angle  $(\delta_1 - \delta_2)$ , we used the separation point method as follows (using Figure 2a as an example):

$$\omega_i = \arctg((1 - i/N) \operatorname{tg}(\delta_i + \alpha_i) + i \operatorname{tg}(\delta_n + \alpha_i)/N) - \alpha_i$$

$i = 0, 1, \dots, N$ ,  $N$  is the total number of points separated

Then we used the Newtonian iteration method to determine the corresponding  $\beta_1$  from the following equation:

$$\arctg(K_1 \beta_1) - K_1 \arctg \beta_1 + K_1 \omega_1 + K_1 \arctg \frac{1}{\beta_1} + c = 0$$

$\beta_1 = \sqrt{M_1^2 - 1}$ ,  $M_1$  is the Mach number on the radial line.

The other parameters can be obtained from the characteristics.

### (3) Superposition of two families of shock waves:

When calculating the external flow field of the inlet under non-design Mach number, it creates the intersection of two first families of shock waves and the intersection between the first family shock wave and the tangential interruption. At this time there may be two different flow structures at the intersection. In the program, from the intensities of the two shock waves and the local Mach number, the final structure can be determined. When the computation progresses to the interception, the initial parameters at the interception can be solved according to the following procedure:

A. Using the initial value of  $\theta_5$  to determine the structure of the flow field: let us take the flow direction and parameters on the lower side of the upper boundary of zone (III) as  $\theta_5^{(0)}$  and the parameters on the lower side of the tangential interruption and solve for the compression angle and determine the parameters in zone (VI). If  $p_s > p_v$ , then the structure in Figure 3a is chosen. Otherwise, the structure in Figure 3b is selected.

B. Correction of  $\theta_5$ : Let us take  $\theta_5^{(1)} = \theta_5^{(0)} + \Delta\theta$ , where  $\Delta\theta$  is the correction quantity ("+" corresponds to Figure 3a, "-" corresponds to Figure 3b).

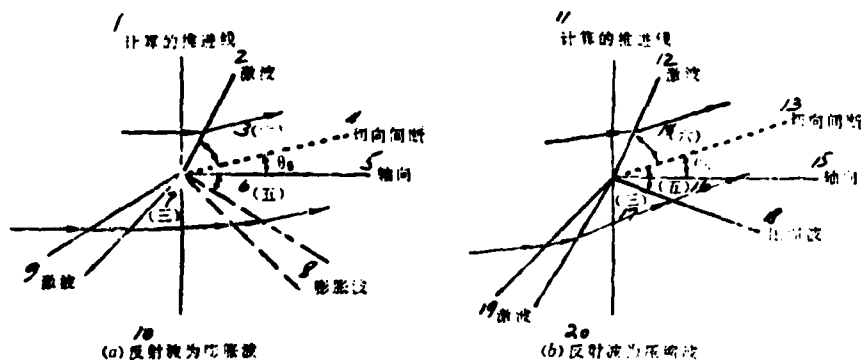


Figure 3. The intersection of two first families of shock waves  
Key: 1--progressive line of calculation; 2--shock wave; 3--(VI); 4--tangential interruption; 5--axial direction; 6--(V); 7--(III); 8--expansion wave; 9--shock wave; 10--reflected wave is an expansion wave; 11--progressive line of calculation; 12--shock wave; 13--tangential interruption; 14--(VI); 15--axial direction; 16--(V); 17--(III); 18--compression wave; 19--shock wave; 20--reflected wave is a compression wave

C. Solving for the compression angle and then determining the parameters in Zone (VI).

D. Solving for the compression or expansion angle to determine the parameters in Zone (V).

E. Evaluating whether  $F(\theta_s) = |p_r(\theta_s) - p_s(\theta_s)| < \epsilon_1$  is valid ( $\epsilon_1$  is a small quantity). If not valid, then use the following equation to correct  $\theta_5$ :

$$\theta_5^{(n+1)} = \theta_5^{(n)} - F(\theta_5^{(n)}) (\theta_5^{(n)} - \theta_5^{(n-1)}) / (F(\theta_5^{(n)}) - F(\theta_5^{(n-1)}))$$

$n = 1, 2, \dots$  repeat until procedure C~E all converge.

The procedures to solve the flow field structure of an intersecting tangential interruption with shock waves are similar as the ones described above.

(4) Hanging shock wave: In an isoentropic cone or quasi-isoentropic cone inlet, under non-design working conditions, a hanging shock wave is created in the flow field due to the intersection of characteristics. Its unique property is that its initial position is unknown. We used an "automatic formation and strength-

ening of shock waves" method in one program to obtain relatively satisfactory results. As we progress along the  $n$  direction, when the characteristics have a tendency to intersect each other, the variations of parameters begin to be violent. Therefore, we added an upper and a lower characteristic boundaries and also increased the density of the lattice in this region. At the point where the characteristics are about to intersect, we introduced a zero intensity shock wave boundary. Its initial slope is taken as the slope of the characteristic line. The parameters on both sides are taken as the local parameters. As we continued to calculate downstream, the shock waves would automatically form and intensify.

#### IV. FORMATION OF THE SOLUTION AND FUNCTIONS OF THE PROGRAM

Using the solution of the steady differential equation of a conical flow to obtain the critical value, we then used the difference method to calculate the flow field in front of the cross-section of the inlet and further obtain the solution of the internal flow field in the tube and the external flow field outside the cowl.

This program can be used to calculate the flow fields of single-cone, bicone, triple-cone, isoentropic cone, quasi-isoentropic and pitot-type inlets. The surfaces of the object, including the center conical surface, inner and outer walls of the cowl, can be formed by sectional curves. The number of sections has no limits. Each section can be one of the following seven types of curves: circular arc, elliptical arc, hyperbolic curves, third order polynomial, quadratic polynomial, linear line and scattered points (using third order spline interpolation).

The program can automatically determine whether the calculation has progressed to reach the front fringe and various singular points, etc., and automatically ascertain the flow field structure at that point.



The input parameters are the geometric parameters of the surface of the object and the Mach number of the incoming flow,

Output parameters: In the flow field in front of the inlet, it can output  $Z, R, M, \theta, \bar{p}, \bar{p}_0, F_{H1}, C_{d1}$  along the stream line. Along the characteristics, we can output  $Z, R, M, \theta, \bar{p}_0$ . In the external flow field outside the cowl, we can output  $Z, R, M, \theta, \bar{p}, \bar{p}_0, C_p, C_D$ . In the internal flow field, we can output  $Z, R, M, \theta, \bar{p}, \bar{p}_0$ . In addition, it can print the Bernoulli constant to verify the accuracy.

The direction of the progress and the step length can be adjusted by the control desk at any time and the radial step length is automatically adjusted by the program according to the magnitude of the zone area and the degree of variation of the parameters.

## V. EXAMPLE AND DISCUSSION

In order to evaluate the practicability of the program, a few actual examples were computed and the results were compared with those obtained using the method of characteristics or the experimental data.

Example 1. Calculation of the isentropic center cone flow field with concentrating focus at  $M_\infty=3.25$ : The computation states are  $M_\infty=3.25$  and 2.75. When  $M_\infty=3.25$  the position of the focus concentrating point of the characteristics of the entire flow field (regardless whether radial or axial) are the same to the third place after the decimal point is the same as the one obtained using the method of the characteristics. When  $M_\infty=2.75$ , the calculated hanging shock wave is as shown in Figure 4. Because there is no actual available example using the method of characteristics for the hanging shock wave of an isentropic cone inlet, we made a comparison of the initial point of the hanging shock wave calculated using the conventional characteristics method (only the initial point was

calculated, not the hanging shock wave) with our results. It can be seen from the figure that the hanging shock wave calculated using the difference method accurately passed through the initial point of the hanging shock wave obtained using the method of characteristics. The intensity of the shock wave after this point becomes very weak.

Example 2. The calculation of internal flow field of a single cone mixed type inlet with  $M_\infty=3.5$ : The coordinates of the shape of the surface are shown in [4]. In the calculation, the center cone surface and the inner surface of the cowl were treated using the third order spline intrapolation method by sections based on the requirements of the shape of the surface as discussed in [4]. The results of the calculation are shown in Figures 5 and 6. From the figures, it indicates that the positions of the shock wave reflection points and the shock wave intensities agree very well with those of the characteristics method before the third reflection. After the third reflection, only very small differences appear. But there are still some differences when compared with the experimental results [5]. The reason apparently is due to the strong interference between the shock wave and the adhesion layer in the internal flow field where viscosity can no longer be omitted.

Example 3. The calculation of the cowl pressure drag in the exponent type of inlet. The equation of the shape of the surface is

$$R = R_{\max} - (R_{\max} - R_0)(1 - \bar{z})^\alpha \quad (13)$$

The parameters used in the calculation are  $R_0/R_{\max}=0.742$ ,  $\alpha=6.12$ ,  $M_\infty=2.2, 2.5, 3.0, 4.0$ .

The corresponding results obtained using the method of characteristics and this calculation are compared and shown in Figures 7 and 8. From the figures it shows that the two methods coincide very well.

AD-A109 681 FOREIGN TECHNOLOGY DIV WRIGHT-PATTERSON AFB OH  
JOURNAL OF AERONAUTICS AND ASTRONOMY.(U)

F/G 20/4

DEC 81

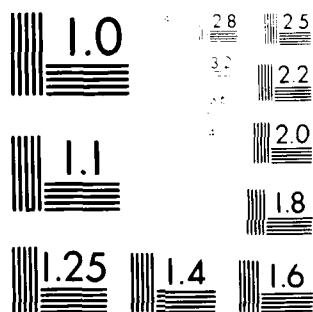
UNCLASSIFIED FTD-ID(RS)T-0722-81

NL

2 OF 2

AD A  
10969

END  
DATE  
FILMED  
02 82  
DTIC



Resolution Test Chart  
100% Contrast, 100% Modulation

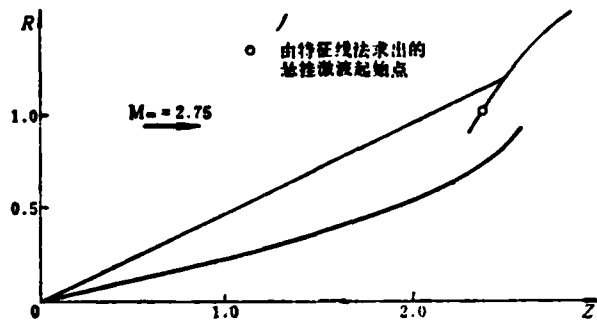


Figure 4. Hanging shock wave of isentropic center cone under non-design conditions

Key: 1--initial point of the hanging shock wave obtained using the method of characteristics

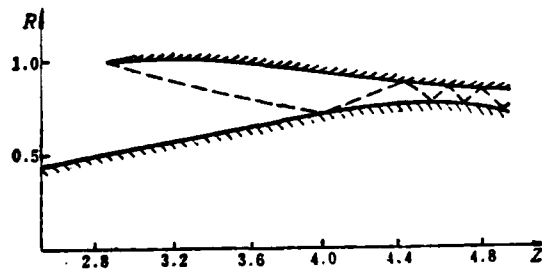


Figure 5. Series of waves of internal flow field of a single-cone mixed type inlet with  $M_\infty = 3.5$

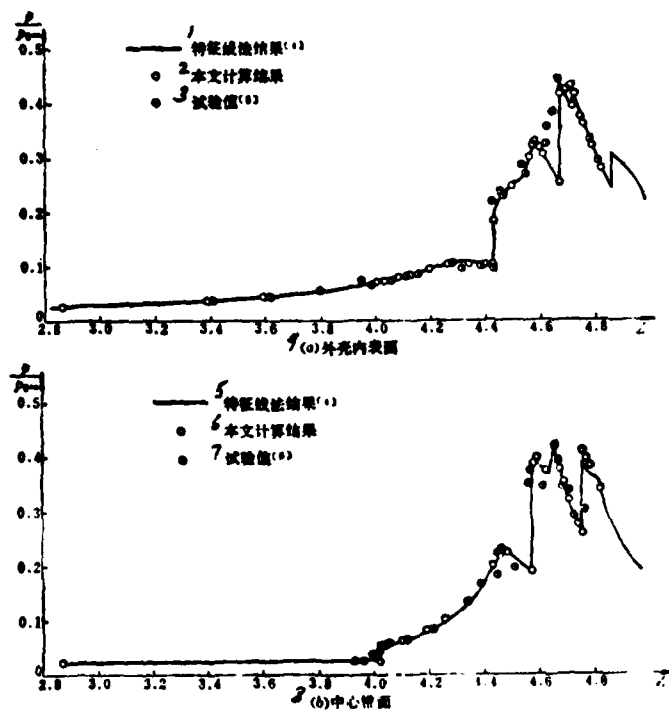


Figure 6. Pressure distribution of the internal flow field of a single cone mixed type inlet with  $M_{\infty}=3.5$

Key: 1--results from the method of characteristics; 2--calculated results of this work; 3--experimental value [5]; 4--inner surface of the cowl; 5--results from the method of characteristics [4]; 6--calculated results of this work; 7--experimental value [5]; 8--center conical surface

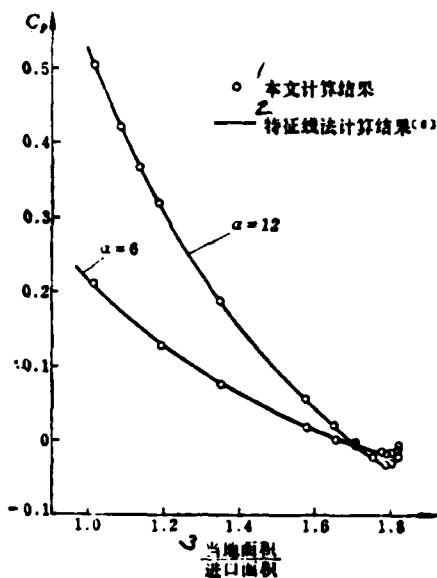


Figure 7. Cowl pressure distribution of an exponent type inlet with  $M_0=2.0$

Key: 1--calculated result in this work; 2--calculated result using the method of characteristics [6]; 3--local area/inlet area;

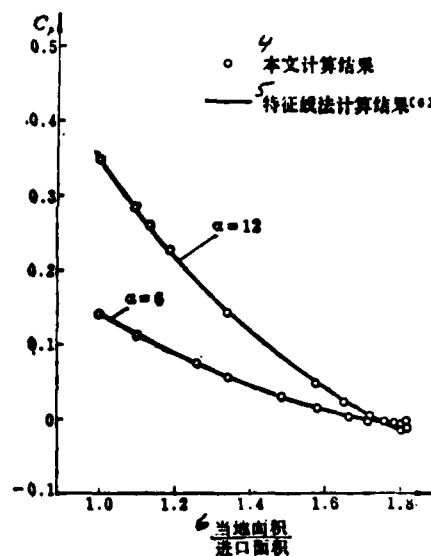


Figure 8. Cowl pressure drag of an exponent type inlet with  $M_0=3.0$

4--calculated result in this work; 5--calculated result using the method of characteristics [6]; 6--local area/inlet area

Example 4. Calculation of cowl pressure drag in a quasi-elliptically shaped inlet [7].

The experimental results in [7] are the origin of the experimental curve of the external drag of the inlets adopted by the American Handbook of Aerodynamics [8]. We calculated the external flow field and pressure drag of cowls 1, 5 and 9 in that literature. The coordinates of the external shape are given in [7]. Figure 9 gives the calculated results of cowls 1 and 5 as well as the calculated results of the shock wave expansion method and the experimental values. From the figure, the calculated results in this work are very close to the experimental values. For the cowl 9 with a large external angle ( $34^\circ$ ) at the front fringe of the cowl, as everybody knows, it is not advisable to use either the linear

method or the shock wave expansion method to calculate the pressure drag. Figure 10 gives the distribution of the calculated partial pressure coefficient of cowl 9 in this work and the corresponding experimental values. From the figure, it shows that the two methods coincide very well. The results calculated using the shock wave expansion method, however, differ significantly from the experimental values. When  $M_\infty=3.88$  and  $4.9$ , the calculated  $C_{Dp}$  for cowl 9 are  $0.182$  and  $0.169$ , respectively. They are very close to the experimental values ( $0.180$  and  $0.175$ , respectively).

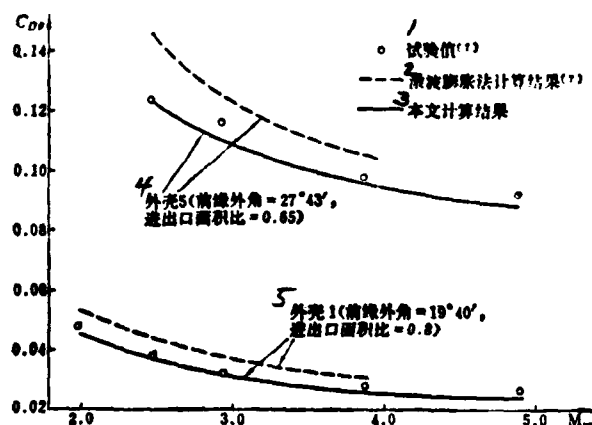


Figure 9. Cowl pressure drag coefficient of a quasi-elliptical inlet

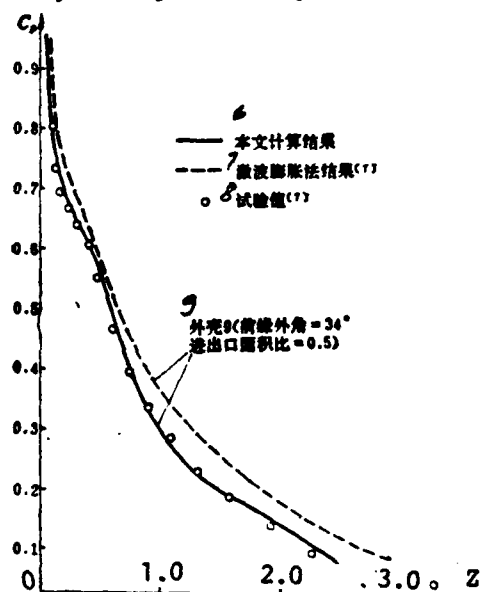


Figure 10. Cowl pressure drag distribution of a quasi-elliptical inlet

Key: 1--experimental values; 2--calculated results using the shock wave expansion method; 3--calculated results in this work; 4--cowl 5 (front fringe external angle =  $27^\circ 43'$ , ratio of inlet and outlet area =  $0.65$ ); 5--cowl 1 (front fringe external angle =  $19^\circ 40'$ , ratio of inlet and outlet area =  $0.8$ ); 6--calculated results in this work; 7--results of the shock wave expansion method; 8--experimental values; 9--cowl 9 (front fringe external angle =  $34^\circ$  ratio of inlet and outlet ratio =  $0.5$ )

Example 5. Calculation of cowl pressure drag distribution of single cone external pressure type inlets. The coordinates of the surface shape are shown in [9]. This program was used to calculate the external flow field outside the cowl and the cowl pressure distribution when  $M_\infty=1.99$ . Figure 11 is a comparison of the calculated



results of the cowl pressure distribution with the experimental values. From the figure, it shows that the calculated results agree with the experimental values very well near the front fringe which has a determining effect on the cowl pressure drag. It shows significant improvement over the calculated results obtained using the linear theory used in the original reference.

In addition to the comparison with the results obtained using the method of characteristics and the experimental data, we calculated the Bernoulli constants for all the lattice points to check the accuracy of the results based on the conservation of energy of the uniform incoming flow which requires the Bernoulli constant  $\left(\frac{1}{2}(u^2+v^2)+3.5p/\rho=\right.$  constant) everywhere in the flow field should be equal to the value of the incoming flow. With respect to the expansion angle, compression angle and regions before and after the intersection of two shock waves where the accuracy cannot be easily ensured, the Bernoulli constant at the lattice point of the flow field deviates from the incoming flow value by  $10^{-4}\sim 10^{-5}$ . In the calculation of the flow field with hanging shock waves, near the hanging shock wave the maximum deviation is about  $5\times 10^{-4}$ . The maximum deviation everywhere in the flow field is less than  $10^{-5}$ .

It has been emphasized in Section II that the equations in each zone in the layer along the progressing direction are divided into three groups. For the second group of equations, an explicit format was used. Therefore, the second group of equations exist in a certain region, the step length of this layer is controlled by the program based on the stability requirements. Otherwise, the step length is adjusted by the control desk according to the slope variation of the surface of the object. The calculated results indicate that larger step length can be used where the variation of the slope is small (assuming the first cone length of the center cone is 1.0 then the step length is  $0.01\sim 0.05$ ) Otherwise, relatively smaller step length ( $0.005\sim 0.01$ ) must be used.

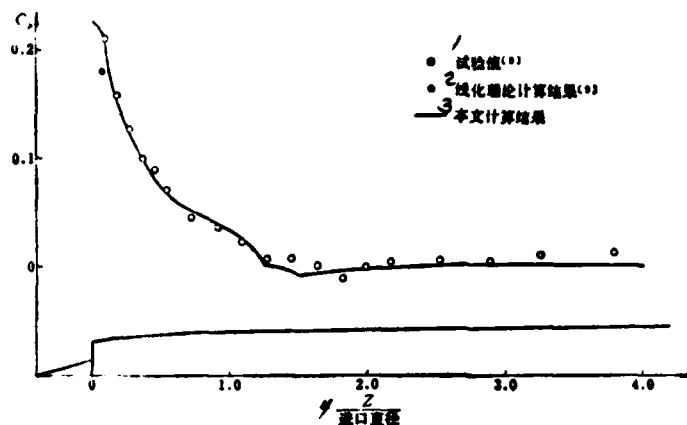


Figure 11. Cowl pressure distribution of a  $25^\circ$  single cone external type inlet

Key: 1--experimental values; 2--calculated results using the linear theory; 3--calculated results in this work; 4--inlet diameter

The iterative method was used many times in the calculation. In order to ensure that the accuracy of the results is not affected by the iterative error, we took the iterative error to be  $10^{-8}$  (relative error).

For scattered point type of surface, due to the limitation of the length of the program, we only considered the multi-section third order sampling intrapolation value. The calculated results indicate that it satisfies the requirements in the treatment of some scattered point type of surface but the accuracy of the Bernoulli constant decreases (the maximum error in the example is  $2\sim 3 \times 10^{-3}$ ).

## VI. CONCLUSIONS

1. This program uses the "separation singularity" difference method whose results agree very well with those using the method of characteristics.

2. The calculated results in the work agree with the experimental values satisfactorily.

3. Because the program can be applied to various types and shapes of inlets and to calculate the internal and external flow fields as well as the cowl pressure drag under design and non-design conditions, it is very practical in the aerodynamic design and selection of inlets.

Comrade Zhang Paushen has participated in part of the work. We wish to express our thanks.

During the compilation of the program, Comrades Chu Youyee, Chung Sichang and Chen Bingmoo from the Computation Center of the Chinese Academy of Science provided enthusiastic guidance and assistance. The authors wish to express their thanks.

#### REFERENCES

- [1] B. H. Anderson, Design of supersonic inlets by a computer program incorporating the method of characteristics. NASA TND-4960. 1969.
- [2] V. L. Sorensen, Computer program for calculating flow fields in supersonic inlets. NASA TND 2897. 1965.
- [3] Chu Youyee et al, "Difference Method in the Initial Boundary Value Problem and the Loop Flow", Science Publication, 1980.
- [4] J. Sybery and T. E. Hickcox, Design of a bleed system for a MACH 3.5 inlet. NASA CR-2187.
- [5] L. L. Presley, Internal flow calculations for axisymmetric supersonic inlets of angle of attack. AIAA p 75-1214.
- [6] L. L. Presley and E. A. Mossman, A study of several theoretical methods for computing the zero-lift wave drag of a family of open-nosed bodies of revolution in  $M = 2.0 \sim 4.0$ . NACA TN 4368.
- [7] N. E. Samanich, Pressure drag of axisymmetric cowls having large initial lip angles at Mach number from 1.90 to 4.90. NACA Memo 1-16-59E.
- [8] U. S. Bureau of Ordnance (Navy Dept.), Handbook of supersonic aerodynamic. V. 6. sec 17. Ducts, nozzle & diffusers. 1964.
- [9] M. I. Weinstein and Joseph Davids, Force and pressure characteristics for a series of nose inlets at Mach number from 1.59 to 1.99. [ conical-spike all-external-compression inlet with supersonic cowl lip. NACA RM E50J30.

### Abstract

A general program using finite-difference method is written to calculate the flow field of supersonic axisymmetric nose inlet. This program is suitable to the direct problem of aerodynamic design of inlets e.g. pitot-type, single-cone, bicone, triple-cone and isentropic cone etc. Since "separation singularity" difference method and implicit-explicit difference scheme are adopted in the calculation of inviscid flow field in the inlet, results of calculation are obtained with second order accuracy at boundary points and internal points, as well as near singular points. This program can offer required internal and external flow characteristics of inlets.

Numerical results for five examples are in satisfactory agreement with corresponding results obtained from the method of characteristics and experimental data.

THE METHOD FOR CALCULATING THE FUEL CONCENTRATION FIELD IN THE  
DOWNSTREAM POSITIONS OF THE PRESSURE JET ATOMIZER IN THE HIGH  
TEMPERATURE GAS STREAM

Fu Weikiao, Tsinghua University

ABSTRACT

Based on an analysis on a large number of experimental results, this paper finds that the fuel concentration distribution (total concentration which is the sum of gas phase and liquid phase concentrations) in the downstream positions of a direct flow type jet atomizer in the high temperature gas stream is a normal distribution. According to this concept, the formula for the calculation of the fuel concentration distribution in the downstream positions of direct flow type of jet atomizer in the high temperature gas stream with certain accuracy is derived which is suitable for engineering design purposes. Thus, a simpler method can be used to carry out the preliminary calculation of such full concentration field problems.

TABLE OF SYMBOLS

- $C_y, C_z$ --fuel flow densities in the y and z directions, respectively.  
(usually called as fuel density), ( $\text{kg}/\text{cm}^2 \text{ sec}$ )
- $C_{FM}$ --fuel concentration obtained experimentally ( $\text{kg}/\text{cm}^2 \text{ sec}$ )
- $C_{\max}$ --maximum fuel concentration ( $\text{kg}/\text{cm}^2 \text{ sec}$ )
- $G_T$ --fuel flow rate ( $\text{kg}/\text{sec}$ )
- $l_y, l_z$ --average square displacements in the y and z directions,  
respectively ( $\text{mm}$ )
- $\Delta p_T$ --pressure difference of the nozzle of the atomizer ( $\text{kg}/\text{cm}^2$ )

Received in February 1980

$t_T, t_B$ --temperatures of the fuel and air, respectively ( $^{\circ}\text{C}$ )  
 $W$ --gas flow velocity (m/sec)  
 $Z_{\text{max}}$ --position of maximum fuel concentration value in the  $Z$ -direction (mm)  
 $\theta$ --the sharp angle formed between the direction of the fuel jet (against the direction of the gas flow) and the direction of the gas flow (degrees)

## I. INTRODUCTION

Because of the simplicity of the structure and ease of arrangement and adjustment, the direct flow type jet atomizer is widely used in compression combustion chambers both here and abroad. The fuel concentration distribution in the downstream positions of the pressure jet atomizer has great influence over the stability of the flame as well as the combustion efficiency. Therefore, the prediction of the fuel concentration distribution downstream from the atomizer is very important for the arrangement of the atomizer and the determination of the relative position between the atomizer and the stabilizer. Henceforth, to solve the calculation formula for the fuel concentration field downstream from the atomizer is imperative to the design and adjustment of compressed combustion chambers. However, until this moment, there has not been any published method for calculating the fuel concentration field downstream from the direct flow type jet atomizer which can be used for engineering design purposes. Although in [1] this method is very difficult to be used in the actual design calculation. Its main problems are that the distribution of the diameter of the fuel droplets at the outlet of the atomizer and the initial velocity of the fuel droplet are difficult to determine. Besides, the friction coefficient of the evaporation of the fuel droplet is also hard to determine. In addition, the physical parameters in the calculation of the evaporation are also hard to define. Therefore, the results of calculation have a certain degree of arbitrariness. Because there are many factors affecting the distribution of the fuel concentration (such as the velocity of the incoming flow, temperature,

pressure, diameter of the nozzle, fuel characteristics and its temperature, nozzle pressure difference, relative position of the direction of the fuel jet, and the gas flow, etc.), it is very difficult to calculate the fuel concentration field downstream of a direct flow type jet atomizer. We discovered after analyzing a large amount of experimental data that the fuel concentration distribution in the downstream positions of a direct flow type atomizer coincides with a normal distribution.

This paper gives the formula to calculate this fuel concentration distribution on the basis of this idea. Preliminary results indicate that the agreement between the calculated results and the experimental data is good. Thus, a simpler method can be used to preliminarily solve a complicated calculation of the distribution of total fuel concentration problem. Its shortcoming is that the range of experimental parameters is not wide enough. Therefore, the application of this method is limited to certain situations. If the range of parameters can be widened continuously, the method proposed in this paper can be applied to calculate under the conditions of wider parametric range. This method may be a simple and effective way to resolve the problem of calculating the fuel concentration distribution downstream from the atomizer in high temperature gas flow. Therefore, it is presented here for the reference of further research, in the fuel concentration field downstream from the direct flow type pressure jet atomizer by relevant institutions.

## II. EXPERIMENTAL RESULTS

The experiments were carried out under the following conditions: (1) diameters of the nozzle are 0.5 and 0.75 mm; (2) the fuel is kerosene; (3) the environmental pressure is a constant pressure; (4) the gas flow velocity distribution is uniform.

The following parameters are changed: the incoming flow velocity  $W$ , the incoming flow temperature  $t_B$ , the nozzle pressure difference  $\Delta p_T$ , the nozzle diameter  $d_c$ , the fuel temperature  $t_T$ , the axial distance  $x$  and fuel jet direction  $\theta$  (mainly for the experiment in which the fuel jet direction is perpendicular to the gas flow direction but experiments were also carried out when the fuel jet is against the gas flow and a  $45^\circ$  angle with the gas flow direction). The measured quantity is the total concentration which is the concentration of the gas phase and the liquid phase combined.

In the experiments the coordinate system such as the one shown in Figure 1 was used with the origin located at the nozzle. The measurements were carried out at the cross-sections where  $x = 100$ , 160 and 220 mm. The fuel concentration distributions along both  $y$  and  $z$  directions were determined in every cross-section. The experimental results are shown in Figures 17 and 18 where the symbol "●" is an experimental point (due to limited page space, the other experimental curves under different working conditions are similar and will be omitted). The axial distance  $x = 220$  mm (for  $x = 100$  and 160 mm, the concentration distributions are not shown in the figures. Their shapes are similar to that at  $x = 220$  mm).

### III. FORMULAS FOR THE CALCULATION OF THE FUEL CONCENTRATION DISTRIBUTION AND ITS APPLICABLE RANGE

After analyzing Figures 17 and 18 as well as other experimental results, a certain law was found to be obeyed. This law is that no matter how the variations of the parameters are, the fuel concentration along the  $y$  direction or the  $z$  direction is a normal distribution (in the figures "▲" and the solid line are calculated based on the normal distribution Equations (1) and (2), and "●" is an experimental point. The two agree very well for all the working conditions. Therefore, the experimental results indicate that the concentration distribution appears to be a normal distribution).



The fuel concentration distribution in the z-direction is wider and the distribution in the y direction is narrower (as shown in Figure 2). Because at high temperatures most fuel drops have already been evaporated to the gas phase after  $x > 100$  mm, at this time diffusion of the turbulent flow has a major effect. Thus, it is similar to a single point source diffusion. Therefore, the concentration exhibits a normal distribution. On the other hand, if under low temperature conditions then because the fuel drops cannot evaporate, the turbulent flow diffusion does not have too much effect on the fuel drops (especially to large drops). The distribution of the fuel drops then primarily depends on the initial conditions of the nozzle and its motion trajectory. Therefore, the distribution in general will not appear as a normal distribution. The discovery of the law of normal distribution of the fuel concentration at high temperatures is very important. It may provide a simpler method to calculate the fuel concentration distribution.

Because it has been verified experimentally that the fuel concentration distributions along the y and z directions in the downstream positions of the direct flow type atomizer coincide with the normal distribution at any cross-section at  $x > 100$  mm, the fuel concentration distribution along y and z directions can be expressed using the following equations:

$$c_y = c_{\max} e^{-\left(\frac{y}{l_y}\right)^2} \quad (1)$$

$$c_z = c_{\max} e^{-\left(\frac{z}{l_z}\right)^2} \quad (2)$$

The problem now is summarized as how to determine the relationships of  $l_y$ ,  $l_z$  and  $c_{\max}$  with various parameters. Because these unknown quantities are related to the incoming flow temperature, velocity, pressure, diameter of the nozzle, pressure difference, property and temperature of the fuel and the direction of the fuel jet, if their mutual relationships can be found, then the problem

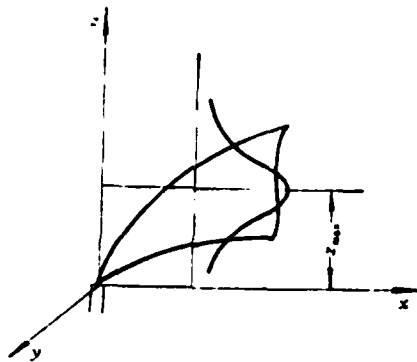


Figure 1

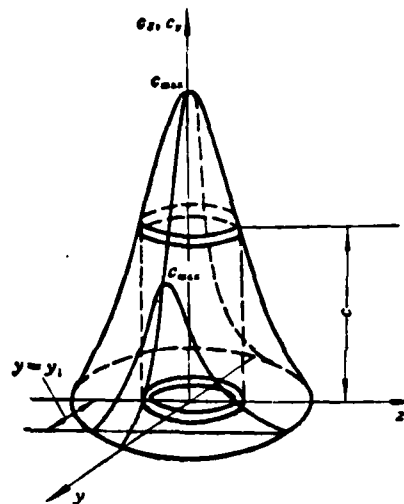


Figure 2. Fuel concentration distribution in downstream of a direct flow type of pressure jet atomizer

is solved. The effects of various parameters on  $l_y$  and  $l_z$  can be obtained from the experimental curves in Figures 17 and 18. The results are shown in Figures 3-14. From these figures, we found another important law which is that the variations of  $l_y$  and  $l_z$  with the parameters are all linear in relation. Thus, it is possible to obtain the relationship expressions using experimental results. Since the relationships are all linear, the relationships of  $l_y$  and  $l_z$  with respect to various parameters can be expressed as

$$l_y = a_0 + a_1 x + a_2 t_r + a_3 \Delta p_r + a_4 W + a_5 t_s + a_6 \theta + a_7 d_s \quad (3)$$

$$l_z = b_0 + b_1 x + b_2 t_r + b_3 \Delta p_r + b_4 W + b_5 t_s + b_6 \theta + b_7 d_s \quad (4)$$

where  $a_0, a_1, \dots, a_7, b_0, b_1, \dots, b_7$  are all constants. They can be determined from the slopes of the straight lines in Figures 3-14 and the results are as follows:

$$\left. \begin{aligned} l_y &= -0.858 + 0.0608 x + 0.0146 t_r + 0.218 \Delta p_r + 0.03 W \\ &\quad - 0.0489 \theta + 8.8 d_s \\ l_z &= 21.82 + 0.0715 x + 0.0273 t_r + 0.518 \Delta p_r - 0.134 W \\ &\quad + 0.004 t_s - 0.0222 \theta + 6 d_s \end{aligned} \right\} \quad (5)$$

where the units are

$$\begin{aligned}
x & \text{ --- mm} \\
t_r, t_s & \text{ --- } ^\circ\text{C} \\
\Delta p_r & \text{ --- kg/cm}^2 \\
W & \text{ --- m/sec} \\
d_s & \text{ --- mm} \\
\theta & \text{ --- degree}
\end{aligned}$$

The  $l_y$  and  $l_z$  calculated using Equation (5) are very close to the experimental results (the comparison of the two is omitted).

In the above, the relationships between the various parameters and  $l_y$  as well as  $l_z$  are given. But, in order to calculate  $c_y$  and  $c_z$ , we must know  $C_{\max}$  which is also related to the various parameters. Its calculation equation can be derived from  $l_y$ ,  $l_z$  and the conservation of fuel along the cross-section (see Figure 2).

$$G_T = \int_F c_s dF = \int_0^\infty c_{\max} e^{-\left(\frac{z}{l_z}\right)^2} d(\pi y z)$$

Based on the relationship of the equi-concentration curve in Figure 2, the relation between the long and short radii of the ellipse can be obtained:

$$\begin{aligned}
& \text{Since,} & c_y = c_s \\
& \text{Therefore,} & c_{\max} e^{-\left(\frac{y}{l_y}\right)^2} = c_{\max} e^{-\left(\frac{z}{l_z}\right)^2}
\end{aligned}$$

Henceforth,

$$\frac{y}{z} = \frac{l_y}{l_z}$$

Substituting it into the integral, we get

$$G_T = \int_0^\infty c_{\max} \pi l_y l_z e^{-\left(\frac{z}{l_z}\right)^2} d\left(\frac{z}{l_z}\right)^2 = \pi c_{\max} l_y l_z \int_0^\infty e^{-\left(\frac{z}{l_z}\right)^2} d\left(\frac{z}{l_z}\right)^2$$

i.e.,  $l_z$  and  $l_y$  do not vary with  $y$  and  $z$  and the proof is omitted.

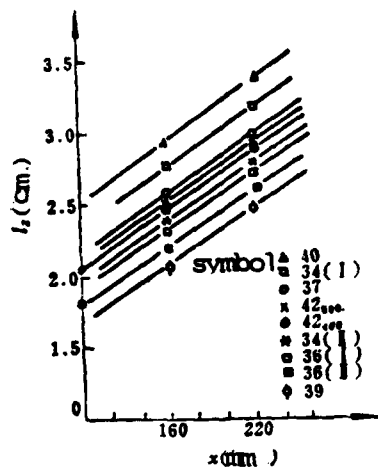


FIG. 3

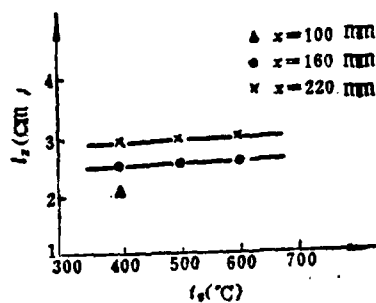


FIG. 4

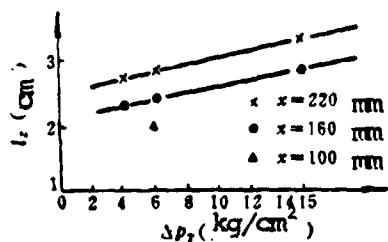


FIG. 5

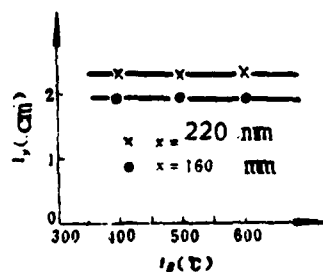


FIG. 6

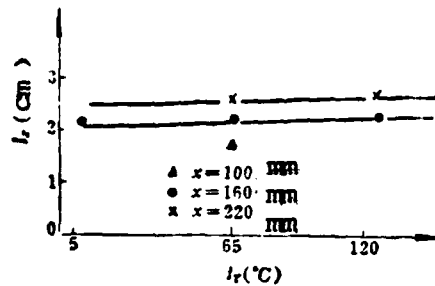


FIG. 7

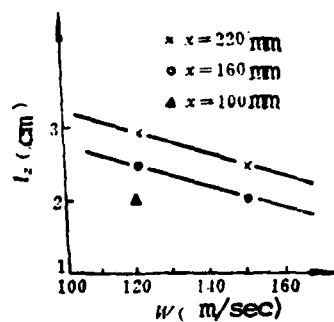


FIG. 8

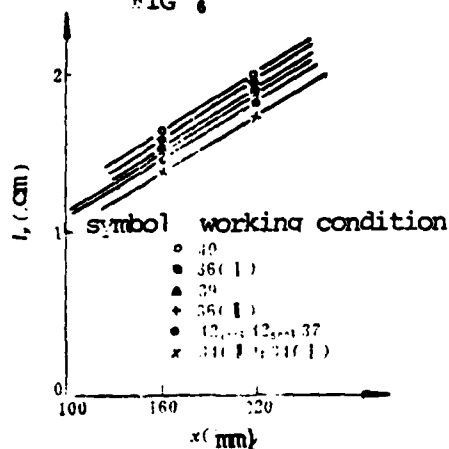


FIG. 9



FIG. 10

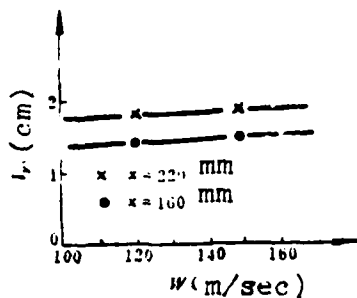


FIG 11

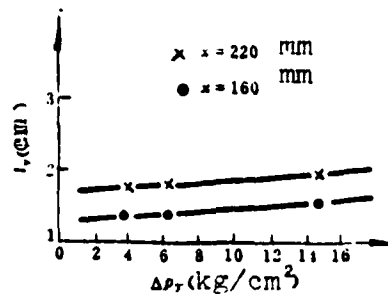


FIG 12

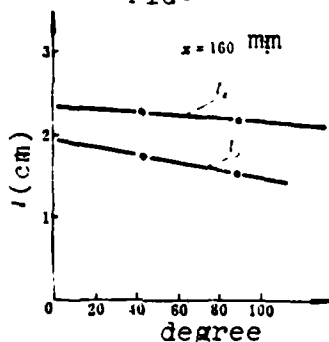


FIG 13

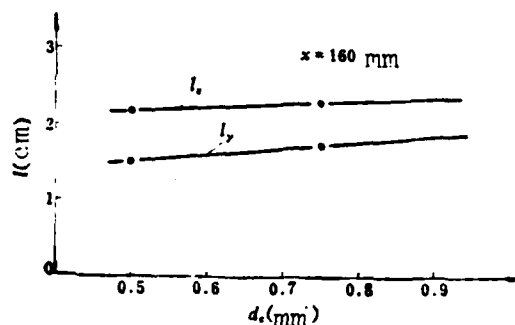


FIG 14

Integrating the above equation, we get

therefore

$$G_T = \pi c_{max} l_y l_x \quad (6)$$

$$c_{max} = \frac{G_T}{\pi l_y l_x}$$

$G_T$  is already known and  $l_y$ ,  $l_x$  can be calculated using Equation (5). The lack of agreement between the  $C_{max}$  calculated using Equation (6) and the  $C_{max}$  (exp.) obtained experimentally is due to measurement error (Note: the maximum value  $C_{max}$  in the  $c_{max} \sim z$  plot is indeed the maximum value of the fuel concentration which is specially assured in our experiments. But the peak value on the  $c_{max} \sim y$  plot is not necessarily the maximum because the  $z$  coordinate is arbitrarily chosen which may not coincide with the  $z$  at the maximum).

Finally, we must determine the position  $z_{max}$  of the maximum of fuel concentration distribution which also corresponds to the penetration depth of the fuel (refer to Figure 1). The variations of  $z_{max}$  with various parameters are shown in Figure 15. From

Figure 15 we know that  $z_{\max}$  varies linearly with flow velocity, temperature, fuel temperature, aperture and the fuel jet direction. Its variation with the nozzle pressure differential is an exponent relation. Therefore, the law of variation of  $z_{\max}$  with the parameters can be expressed as:

$$\begin{aligned} z_{\max} &= a_1 + a_2 i_T + a_3 (a \Delta p_T + b)^m + a_4 W + a_5 i_s + a_6 \theta + a_7 d_s \\ &= a_1 + a_2 i_T + a_3 P + a_4 W + a_5 i_s + a_6 \theta + a_7 d_s \end{aligned}$$

where  $P = (a \Delta p_T + b)^m$ , and the constants  $a$ ,  $b$ , and  $m$  can be determined experimentally because when the other parameters remain unchanged, then the relation between  $z_{\max}$  and  $\Delta p_T$  can be expressed as:

$$z_{\max} = A(a \Delta p_T + b)^m$$

where  $A$  is a constant. Taking the logarithm on both sides, we get:

$$\ln z_{\max} = \ln A + m \ln(a \Delta p_T + b)$$

Therefore, the relationship between  $\ln z_{\max}$  and  $\ln(a \Delta p_T + b)$  should be linear where  $z_{\max}$  and  $\Delta p_T$  are given experimentally. When the values of  $a$  and  $b$  are properly chosen then it is possible to arrange the experimental results into the linear relation between  $\ln z_{\max}$  and  $\ln(a \Delta p_T + b)$ . For example, if we take  $a = \frac{1}{6} [1/\text{atm}]$ ,  $b = -0.56$ , then the linear relationship is obtained as shown in Figure 16. Its slope  $m = 0.306$ . Thus we get

$$P = \left( \frac{1}{6} \Delta p_T - 0.56 \right)^{0.306}$$

Similarly, it is possible to determine other constants from the slopes and intercepts of the straight lines in Figures 15 and 16.

$$\begin{aligned} z_{\max} &= 22.1 - 0.111 i_T + 37.9 \left( \frac{1}{6} \Delta p_T - 0.56 \right)^{0.306} \\ &\quad - 0.47 W + 0.065 i_s + 0.1178 \theta + 10.8 d_s \end{aligned} \quad (7)$$

The units used in the equation are:  $Z_{\max}$ =mm;  $\Delta p_r$ =kg/cm<sup>2</sup>;  $W$ =m/sec;  $t_T, t_B$ -°C;  $d_c$ -mm;  $\theta$ -degree.

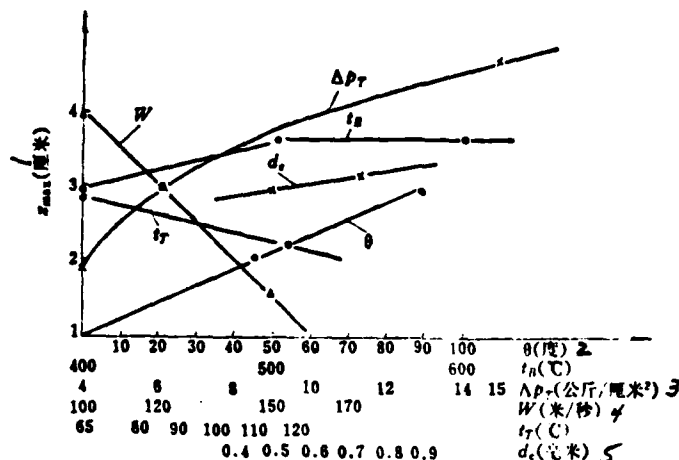


Figure 15. Relationships between  $Z_{\max}$  and  $t_B$ ,  $\Delta p_r$ ,  $W$ ,  $t_T$ ,  $\theta$  and  $d_c$ .

Key: 1-- $Z_{\max}$  (cm); 2--degree; 3--(kg/cm<sup>2</sup>); 4--(m/sec); 5--(mm)

Experimental results indicate that the variation of  $Z_{\max}$  along the x direction is not very large when the other parameters remained unchanged. Therefore, it is possible to assume that it does not vary and to take its average value to represent it.

The calculated value using Equation (7) has very little difference with the experimental value, therefore, it can be used on the calculation.

Caution: In our consideration of the effect of the flow temperature  $t_B$  on  $Z_{\max}$ , from Figure 5 we can see that when the temperature is greater than 500°C, then  $Z_{\max}$  remains unchanged. Therefore, when  $t_B > 500^\circ\text{C}$  we can calculate using Equation (7) based on  $t_B = 500^\circ\text{C}$ .

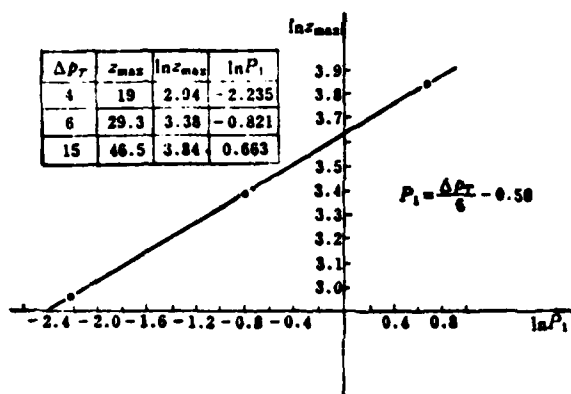


Figure 16. The relation between  $\ln z_{max}$  and  $\ln\left(\frac{\Delta p_r}{6} - 0.56\right)$

The applicable range of this method is as follows:

$$\begin{aligned}
 &400^\circ\text{C} < t_s < 600^\circ\text{C}, \quad 100 \text{ m/sec} < W < 170 \text{ m/sec} \\
 &70^\circ\text{C} < t_r < 120^\circ\text{C}, \quad 4 \text{ kg/cm}^2 < \Delta p_r < 15 \text{ kg/cm}^2 \\
 &100 \text{ mm} < x < 220 \text{ mm}; \quad 0.4 \text{ mm} < d_c < 0.9 \text{ mm} \\
 &0^\circ < \theta < 90^\circ
 \end{aligned}$$

However, from the tendency of the straight lines in Figures 3-14, we can see that the linear variations of  $l_y$  and  $l_z$  with the parameters are good and the slopes of variation are not large. Therefore, it should be possible to extend the range of parameters as described above. During the extension, it should be noticed that:

(1) when extending in the direction of decreasing nozzle pressure differential, according to  $P = \left(\frac{1}{6}\Delta p_r - 0.56\right)^{0.300}$  we know that when  $\Delta p_r = 3.36$ ,  $P = 0$ . Therefore, when  $\Delta p_r < 3.36$  we should still take  $P = 0$ ; (2) during the extension of the range of parameters, the calculated values of  $l_y$ ,  $l_z$  and  $z_{max}$  should not be negative. They should all be greater or equal to zero to be reasonable. For example, when  $\Delta p_r = 6 \text{ kg/cm}^2$ ,  $t_T = 70^\circ\text{C}$ ,  $t_B = 400^\circ\text{C}$  and  $W = 200 \text{ m/sec}$ , the calculated value of  $z_{max} = -8.1 \text{ mm}$  at this time which is unreasonable. It should be taken as  $z_{max} = 0$  to be reasonable. In other words, at this time the nozzle



pressure differential is small and the gas flow velocity is larger, therefore, the penetration depth of the fuel is zero. Or, we can say that the fuel is turned around the moment it leaves the nozzle. Equation (7) indicates that if the flow speed in the compression combustion chamber is large, in order to allow the fuel to reach a certain penetration depth, we must then raise the pressure differential of the nozzle. Similarly, it is known from Equation (5) that when the flow velocity is too large then  $l_z$  becomes very small. This means that the distribution of fuel concentration is concentrated thus creating a localized fuel rich situation affecting the efficiency. Therefore, the flow parameters in the combustion chamber and the parameters of the nozzle (e.g., aperture, fuel pressure, fuel jet direction, fuel temperature, etc.) must be reasonably matched to obtain a reasonable concentration distribution. With this method for the calculation of the fuel concentration, this work can be performed to obtain a preliminary nozzle arrangement in the combustion chamber before adjustment tests in order to minimize the blindness in the original trial. It also can reduce the time period of adjustment for the combustion chamber and save some expense in the adjustment. Therefore, it is necessary to preliminarily estimate the fuel concentration in the design of compression combustion chambers.

The procedures to calculate the fuel concentration distribution in downstream positions of a direct flow type pressure jet atomizer (the fuel concentration distribution at the  $y=y$  cross-section as shown in Figure 2) are as follows:

- (1) based on the work conditions to calculate  $l_y$ ,  $l_z$ ,  $C_{max}$  and  $z_{max}$  using Equations (5), (6) and (7).
- (2) calculate the following:

$$c_{max,1} = c_{max} e^{-\left(\frac{y}{l_y}\right)^2} = c_{max} e^{-\left(\frac{y_1}{l_y}\right)^2}$$

- (3) calculate the concentration along the  $z$  direction:

$$c_x = c_{max} e^{-\left(\frac{x}{l_x}\right)^2}$$

When the value of  $y$ , is varied from 0 to  $\infty$ , we can calculate the fuel concentration at any point in space.

The results obtained based on the method introduced in this work are shown as "x" in Figures 17 and 18 (the calculated results under other work conditions are similar and, therefore, omitted). They agree very well with the experimental results.

On the basis of the introduction in [1] and the indication of our experimental results (omitted), the fuel concentration field downstream from multiple atomizers can be formed by the superposition of the concentration fields of the single atomizers. Thus, the calculation of the fuel concentration field downstream from the nozzle becomes more meaningful. When such a fuel concentration field is known, it can be used to estimate the fuel concentration distribution downstream from the atomizer ring in the compressed combustion chamber.

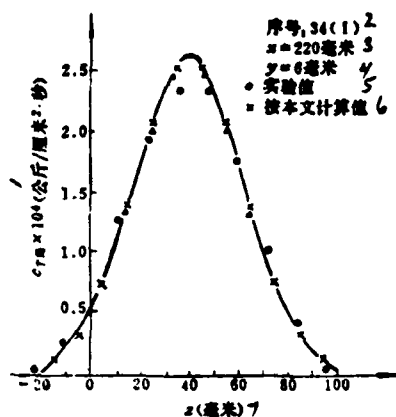


Figure 17

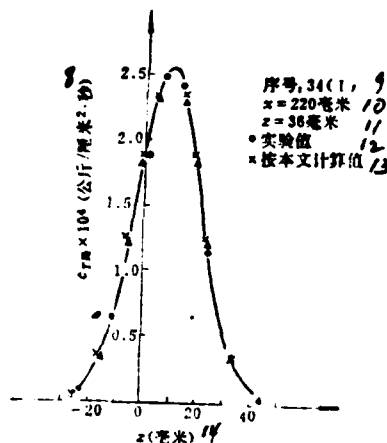


Figure 18

Key: 1--(kg/cm<sup>2</sup>.sec); 2--sequence number; 3--mm; 4--mm;  
5--experimental value; 6--calculated value in this work;  
7--mm; 8--(kg/cm<sup>2</sup>.sec); 9--sequence number; 10--mm;  
11--mm; 12--experimental value; 13--calculated value in  
this work; 14--mm

#### REFERENCES

1. B.V. Raushenbakh, S.A. Belyy. Physical bases of the working process in combustion chambers of air jet engines.

#### Abstract

It has been found from quite a number of experimental results that the distribution of the fuel concentration (the total concentration i. e. the resultant concentration of both vapour and liquid phases) is normal distribution. According to this idea, the formula for calculation of the fuel concentration is obtained. This formula is useful for engineering purpose with desirable accuracy. Thus, the calculation of such fuel concentration field may be carried out in a simpler way.

# A VEHICLE ATTITUDE CONTROL SYSTEM FORMING THE ERROR SIGNAL BY WAY OF THE OPTIMAL ROTATION AXIS

**Dai Zongli Shi Ruohua** (*Beijing Institute of Control Engineering*)

**Bi Dachuan** (*Institute of System Science and Mathematical  
Science Academia Sinica*)

## Abstract

This paper deals with a method forming the error signal to control the direction of the longitudinal axis of a vehicle by way of the optimal rotation axis. In order to control rotation around the longitudinal axis, the ways to form the error signals in the case of roll stability and slope stability are considered. The analytical formulae are developed in detail. As examples of application of this method we have also discussed how to form the error signals sensed by a three gimbal platform or a group of strapdown rate gyros mounted in the vehicle. Corresponding block diagrams are presented.

## I. INTRODUCTION

The function of the vehicle attitude control system is to control the rotational motion of aeronautical vehicles to reach the required attitude. We are going to separate the attitude control problem into the control of the direction of the longitudinal axis of the aeronautical vehicle and the control of the rotation around the longitudinal axis. The emphasis of this paper is to discuss the formation of the error signal using the optimal rotational axis method to control the direction of the longitudinal axis. As for the control of the rotation around the longitudinal axis itself, it mainly discussed the forming of the error signal under roll stability

---

Received April 16, 1979

and slope stability conditions. These error signals reflect the difference between the attitude of the vehicle required by the control and the actual attitude of the vehicle. These signals are then decomposed on the tilt axis, deviation axis and roll axis in the body coordinate system and the control channels of the attitude control system control the rotation motion of their corresponding axes according to the components of these error signals until the error signal becomes zero and the actual attitude of the aeronautical vehicle reaches the required attitude.

In the example of the forming of the error signals by a three gimbal platform and a strap-down rate gyro given to explain the actual application of this method, we only give the corresponding system structural theory diagram. As for the design problem such as the selection of the system parameters, we are not going to discuss it in this paper.

This method should be applicable to various aeronautical vehicles and various stages of the flight. When the required attitude angles vary significantly for the aeronautical vehicle, the use of this method has an even larger advantage.

We have carried out a simulated calculation on a system using a reaction nozzle as the attitude control of the vehicle structural space of an aircraft by this method, to control the direction of the longitudinal axis of the vehicle to rotate by  $90^\circ$  in different directions. The calculated result indicates that the system characteristics are good.

## II. THE COORDINATE SYSTEM

### 1. Launching point inertia coordinate system: $Z_f-ox_fy_fz_f$

The origin of the coordinate system is located at the launching point of the aeronautical vehicle. The  $ox_f$  axis is on the horizontal

plane pointing at the launching direction. The  $oy_f$  axis is perpendicular to the horizontal plane and pointing upward. The  $oz_f$  axis forms a right handed coordinate system with  $ox_f$  and  $oy_f$  axes.

## 2. Body coordinate system: $Z_1-ox_1y_1z_1$

(1) Definition: The origin of the coordinate system is located at the center of mass of the aeronautical vehicle. The  $ox_1$  axis is in the direction of the longitudinal axis of the aeronautical vehicle. The  $oy_1$  axis is on the longitudinal symmetry plane of the vehicle and perpendicular to the  $ox_1$  axis. The  $oz_1$  axis forms a right handed coordinate system with  $ox_1$  and  $oy_1$  axes.  $ox_1$ ,  $oy_1$  and  $oz_1$  axes are also called the roll axis, deviation axis and the tilt axis, respectively.

### (2) Relationship with the coordinate system $Z_F$

From now we are only going to discuss the rotational transformation relationships between coordinate systems. Therefore, the same symbol  $o$  is used as the origin of all the coordinate systems. The relations between the coordinate system  $Z_1$  and  $Z_F$  can be expressed as

$$\begin{bmatrix} x_1 \\ y_1 \\ z_1 \end{bmatrix} = B \begin{bmatrix} x_f \\ y_f \\ z_f \end{bmatrix} \quad (1)$$

$$B = (b_{ij}) \quad \begin{matrix} i = 1, 2, 3 \\ j = 1, 2, 3 \end{matrix}$$

where  $x_1$ ,  $y_1$  and  $z_1$  are the projections of a vector on the corresponding axes in the  $Z_1$  coordinate system. The matrix  $B$  is the coordinate transformation matrix from the  $Z_F$  coordinate system to the  $Z_1$  coordinate system.

The matrix  $B$  can be expressed by the attitude angles. Let  $\phi$ ,  $\psi$  and  $\gamma$  be the tilt angle, the deviation angle and the roll angle,

respectively. It is also to make the transformation from the  $Z_F$  to the  $Z_1$  coordinate system to begin with the tilt and then the deviation and finally the roll (as shown in Figure 1). The matrix  $B$  expressed in terms of the attitude angles can be written as

$$B = B_z = [\gamma][\psi][\varphi] \quad (2)$$

where

$$[\gamma] = \begin{bmatrix} 1 & 0 & 0 \\ 0 & \cos \gamma & \sin \gamma \\ 0 & -\sin \gamma & \cos \gamma \end{bmatrix}$$

$$[\psi] = \begin{bmatrix} \cos \psi & 0 & -\sin \psi \\ 0 & 1 & 0 \\ \sin \psi & 0 & \cos \psi \end{bmatrix}$$

$$[\varphi] = \begin{bmatrix} \cos \varphi & \sin \varphi & 0 \\ -\sin \varphi & \cos \varphi & 0 \\ 0 & 0 & 1 \end{bmatrix}$$

after calculation, we get

$$b_{11} = \cos \psi \cos \varphi$$

$$b_{12} = \cos \psi \sin \varphi$$

$$b_{13} = -\sin \psi$$

$$b_{21} = \sin \gamma \sin \psi \cos \varphi - \cos \gamma \sin \varphi$$

$$b_{22} = \sin \gamma \sin \psi \sin \varphi + \cos \gamma \cos \varphi$$

$$b_{23} = \sin \gamma \cos \psi$$

$$b_{31} = \cos \gamma \sin \psi \cos \varphi + \sin \gamma \sin \varphi$$

$$b_{32} = \cos \gamma \sin \psi \sin \varphi - \sin \gamma \cos \varphi$$

$$b_{33} = \cos \gamma \cos \psi$$

If the element  $b_{1j}$  of the matrix  $B$  is known, and the attitude angles are to be determined, then it is possible to derive the following based on the above equations:

$$\sin \psi = -b_{13} \quad -90^\circ < \psi < 90^\circ$$

$$\begin{cases} \sin \varphi = \frac{b_{12}}{\cos \psi} \\ \cos \varphi = \frac{b_{11}}{\cos \psi} \end{cases} \quad (3)$$

$$(4)$$

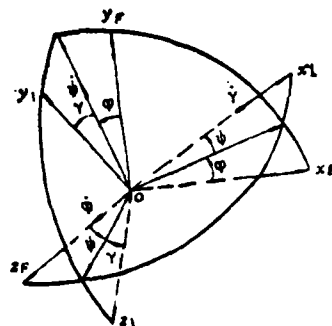


Figure 1. Transformation relationship between the  $Z_1$  and  $Z_F$  coordinate systems

or

$$\begin{cases} \operatorname{tg} \varphi = \frac{b_{12}}{b_{11}} \\ \operatorname{ctg} \varphi = \frac{b_{11}}{b_{12}} \end{cases} \quad (4)'$$

or

$$\begin{cases} \sin \gamma = \frac{b_{23}}{\cos \psi} \\ \cos \gamma = \frac{b_{33}}{\cos \psi} \end{cases} \quad (5)$$

$$\begin{cases} \operatorname{tg} \gamma = \frac{b_{23}}{b_{33}} \\ \operatorname{ctg} \gamma = \frac{b_{33}}{b_{23}} \end{cases} \quad (5)'$$

### 3. Command coordinate system: $Z_c$ - $ox_c, y_c, z_c$

Let the command attitude angles be  $\phi_c$ ,  $\psi_c$  and  $\gamma_c$  and the command coordinate systems  $Z_c$  is defined as the coordinate system which satisfies the following relations with the  $Z_F$  coordinate system, i.e. (see Figure 2)

$$\begin{bmatrix} x_c \\ y_c \\ z_c \end{bmatrix} = (\gamma_c)(\psi_c)(\phi_c) \begin{bmatrix} x_F \\ y_F \\ z_F \end{bmatrix} \quad (6)$$

where

$$\begin{aligned} (\gamma_c) &= \begin{bmatrix} 1 & 0 & 0 \\ 0 & \cos \gamma_c & \sin \gamma_c \\ 0 & -\sin \gamma_c & \cos \gamma_c \end{bmatrix} \\ (\psi_c) &= \begin{bmatrix} \cos \psi_c & 0 & -\sin \psi_c \\ 0 & 1 & 0 \\ \sin \psi_c & 0 & \cos \psi_c \end{bmatrix} \\ (\phi_c) &= \begin{bmatrix} \cos \phi_c & \sin \phi_c & 0 \\ -\sin \phi_c & \cos \phi_c & 0 \\ 0 & 0 & 1 \end{bmatrix} \end{aligned}$$

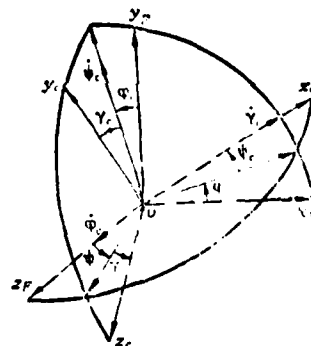


Figure 2. Relationships between the command coordinate system and the launching point inertia (coordinate system)

The command attitude angles are the attitude angles the flight control systems of the vehicle wishes to reach. They are the input quantities in the attitude control system. The function of the attitude control system is to control the attitude angles of the aeronautical vehicle so that they reach the values of those of the command attitude angles. Therefore,  $ox_c$ ,  $oy_c$  and  $oz_c$  axes are the directions of the corresponding axes of the ideal body coordinate



system when the aeronautical vehicle reaches the required attitude.

### III. THE ERROR SIGNALS CONTROLLING THE DIRECTION OF THE LONGITUDINAL AXIS

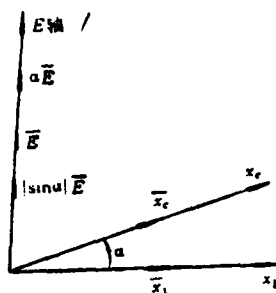
#### 1. Basic concept of the optimal rotation axis method

In order to transform the longitudinal axis  $ox_1$  of the aeronautical axis to the  $ox_c$  direction, it can be accomplished by rotating around a fixed rotation axis  $E$  by an angle  $\alpha$ . Apparently, the direction of this axis  $E$  is perpendicular to the  $ox_1$  and  $ox_c$  axes and the angle  $\alpha$  is the angle between the  $ox_c$  and  $ox_1$  axes (see Figure 3). It is the smallest angle to rotate the  $ox_1$  axis to the  $ox_c$  direction. We call the  $E$  axis as the optimal rotation axis.

Let  $\bar{E}$  be the unit vector on the  $E$  axis. We use  $\alpha\bar{E}$  as the error signal and then decompose  $\alpha\bar{E}$  onto the body coordinate system  $Z_1$  which forms the error signals in the direction of the axes in the body coordinate system. Through the various attitude control channels to eliminate them until  $\alpha = 0$ , then  $ox_1$  axis is being controlled to the  $ox_c$  direction. Thus this error signal forming method is called the optimal rotation axis method for the control of the direction of the longitudinal axis. We simply called it the optimal rotation axis method.

Figure 3. Schematic diagram of the optimal rotation axis

Key: 1--  $E$  axis



#### 2. Derivation of the error signal equations

Let us take a unit vector  $\bar{x}_1$  on the  $ox_1$  axis and also a unit vector  $\bar{x}_c$  on the  $ox_c$  axis (see Figure 3). We first find the

expressions of their projections in the  $Z_1$  coordinate system. The projections of  $\bar{x}$  in the  $Z_1$  coordinate system is 1, 0, 0, so its projection in the  $Z_1$  coordinate system expressed as  $\bar{x}_{1Z_1}$  is

$$\bar{x}_{1Z_1} = (1, 0, 0)^T \quad (7)$$

T represents the transformation of matrix. Let the projection of  $\bar{x}_c$  in the  $Z_1$  coordinate system be  $C_{x1}$ ,  $C_{t1}$  and  $C_{z1}$  and the projection in the  $Z_1$  coordinate system can be expressed as

$$\bar{x}_{cZ_1} = (C_{x1}, C_{t1}, C_{z1})^T$$

We are going to derive the expression of  $\bar{x}_{cZ_1}$ . The projection of the vector  $\bar{x}_c$  in the  $Z_c$  coordinate system is 1, 0, 0. The projection in the  $Z_c$  coordinate system can be expressed as

$$\bar{x}_{cZ_c} = (1, 0, 0)^T$$

The projection in the coordinate system  $Z_F$  is  $c_{x_F}$ ,  $c_{y_F}$ ,  $c_{z_F}$ .

The projection in the  $Z_F$  coordinate system can be expressed as

$$\bar{x}_{cZ_F} = (c_{x_F}, c_{y_F}, c_{z_F})^T$$

From Equation (6), there is

$$\bar{x}_{cZ_c} = (\gamma_c)(\psi_c)(\varphi_c)\bar{x}_{cZ_F}$$

then  $\bar{x}_{cZ_F} = (\varphi_c)^T(\psi_c)^T(\gamma_c)^T\bar{x}_{cZ_c}$

$$\begin{aligned} &= \begin{bmatrix} \cos \varphi_c & -\sin \varphi_c & 0 \\ \sin \varphi_c & \cos \varphi_c & 0 \\ 0 & 0 & 1 \end{bmatrix} \begin{bmatrix} \cos \psi_c & 0 & -\sin \psi_c \\ 0 & 1 & 0 \\ \sin \psi_c & 0 & \cos \psi_c \end{bmatrix} \begin{bmatrix} 1 & 0 & 0 \\ 0 & \cos \gamma_c & -\sin \gamma_c \\ 0 & \sin \gamma_c & \cos \gamma_c \end{bmatrix} \begin{bmatrix} 1 \\ 0 \\ 0 \end{bmatrix} \\ &= \begin{bmatrix} \cos \varphi_c \cos \psi_c \\ \sin \varphi_c \cos \psi_c \\ -\sin \psi_c \end{bmatrix} \quad (8) \end{aligned}$$

From Equation (1), there is

$$\bar{x}_{cZ_1} = \begin{bmatrix} c_{x1} \\ c_{y1} \\ c_{z1} \end{bmatrix} = R\bar{x}_{cZ_F} = R \begin{bmatrix} \cos \varphi_c \cos \psi_c \\ \sin \varphi_c \cos \psi_c \\ -\sin \psi_c \end{bmatrix} \quad (9)$$

With the expressions for  $\bar{x}_{1z_1}$  and  $\bar{x}_{ez_1}$ , Equations (7) and (9), the E axis and angle  $\alpha$  can be obtained. Let the unit vectors of the three axes of the  $Z_1$  coordinate system be  $\bar{x}_1, \bar{y}_1, \bar{z}_1$ . From the definition of the vector product

$$|\sin \alpha| \bar{E} = \bar{x}_1 \times \bar{x}_e$$

The calculation in the  $Z_1$  coordinate system has

$$|\sin \alpha| \bar{E} = \bar{x}_{1z_1} \times \bar{x}_{ez_1} = \begin{vmatrix} \bar{x}_1 & \bar{y}_1 & \bar{z}_1 \\ 1 & 0 & 0 \\ c_{x_1} & c_{y_1} & c_{z_1} \end{vmatrix} = -c_{x_1} \bar{y}_1 + c_{y_1} \bar{z}_1 \quad (10)$$

Considering model that  $|\sin \alpha|$  is  $\bar{x}_{1z_1} \times \bar{x}_{ez_1}$  then,

$$|\sin \alpha| = \sqrt{c_{y_1}^2 + c_{z_1}^2}$$

So Equation (10) can be written as

$$\bar{E} = -\frac{c_{x_1}}{\sqrt{c_{y_1}^2 + c_{z_1}^2}} \bar{y}_1 + \frac{c_{y_1}}{\sqrt{c_{y_1}^2 + c_{z_1}^2}} \bar{z}_1 \quad (11)$$

From the definition of the dot product

$$\cos \alpha = \bar{x}_1 \cdot \bar{x}_e$$

the calculation in the  $Z_1$  coordinate system has

$$\cos \alpha = \bar{x}_{1z_1} \cdot \bar{x}_{ez_1} = c_{x_1} \quad (12)$$

$$\alpha = |\arccos c_{x_1}| \quad \alpha \leq 180^\circ$$

taking

Multiplying Equations (11) and (12), we then obtain the projection expression of the error signal to control the direction of the longitudinal axis in the  $Z_1$  coordinate system:

$$\alpha \bar{E} = -\frac{c_{x_1}}{\sqrt{c_{y_1}^2 + c_{z_1}^2}} |\arccos c_{x_1}| \bar{y}_1 + \frac{c_{y_1}}{\sqrt{c_{y_1}^2 + c_{z_1}^2}} |\arccos c_{x_1}| \bar{z}_1 \quad (13)$$

From Equation (13), we can see that the longitudinal axis direction control error signal does not have a component in the  $ox_1$  axis direction. The error signals in the  $oy_1$  and  $oz_1$  axes are  $e_y, e_z$  respectively:

$$\epsilon_y = -\frac{c_{y_1}}{\sqrt{c_{y_1}^2 + c_{z_1}^2}} = |\arccos c_{z_1}| \quad (14)$$

$$\epsilon_z = \frac{c_{z_1}}{\sqrt{c_{y_1}^2 + c_{z_1}^2}} = |\arccos c_{z_1}| \quad (15)$$

### 3. Simplification of equations

We use  $|\sin \alpha| \bar{E}$  as the error signal then Equation (10) is a simple form of the expression of the projection in the  $Z_1$  body coordinate system of the error signals which control the direction of the longitudinal axis. Therefore, the error signals are

$$\epsilon_y = -c_{z_1} \quad (16)$$

$$\epsilon_z = c_{y_1} \quad (17)$$

When the command attitude angles  $\vartheta$ ,  $\psi$  are given, then the error signals  $\epsilon_y$ ,  $\epsilon_z$  control the direction of the longitudinal axis according to Equations (9) as well as (16) and (17) (or Equations (14) and (15)).

The calculated results indicate that the characteristics of the system do not have any difference between the one obtained using the simple error signal Equations (16) and (17) and that using the complicated Equations (14) and (15). Therefore, we chose Equations (6) and (17).

## IV. THE ERROR SIGNAL TO CONTROL THE ROTATION AROUND THE LONGITUDINAL AXIS

### 1. General conditions

The longitudinal axis direction control error signal does not have a component in the  $ox_1$  axis direction. Similarly, the error signal to control the rotation around the longitudinal axis does not have any component on the  $oy_1$  and  $oz_1$  axes. Therefore, the roll

control channel and the tilt-deviation control channel are independent.

If the roll angle command  $\gamma_c$  is given, then the difference between  $\gamma_c$  and  $\gamma$  can be used as the error signal  $\epsilon_x$  which can be used to control rotation around the longitudinal axis, i.e.,

$$\epsilon_x = \gamma_c - \gamma \quad (18)$$

Under many conditions, the control requirement of the roll angle is frequently not given. Only the command attitude angles  $\varphi_c, \psi_c$  are given and the control of the rotation around the longitudinal axis is carried out according to a certain method of stabilization.

## 2. Slope stability

The definition of slope stability is to require one of the axes in the body coordinate system of the aeronautical vehicle to remain parallel to a fixed plane during the course of the flight. For example, the commonly used one is to require the  $oy_1$  axis to remain parallel to the launch plane ( $x_0oy_0$  plane). This corresponds to  $\gamma_c \equiv 0$ . According to Equation (18)

$$\epsilon_x = -\gamma \quad (19)$$

Substituting the  $\text{tg } \gamma$  in Equation (5)' into Equation (19), we get

$$\epsilon_x = -\text{arctg} \frac{b_{23}}{b_{33}} \quad (19)'$$

We can also use  $\text{tg } \gamma$  to replace the  $\gamma$  of Equation (19) and plug  $\text{tg } \gamma$  into Equation (5)', then the error signal can be written as

$$\epsilon_x = -\frac{b_{23}}{b_{33}} \quad (19)''$$

## 3. Roll stability

The definition of roll stability is that it is required for the integral of the rotational angular velocity around the longitudinal axis of the aeronautical vehicle during the flight, i.e.,

$$\int \omega_{z_1} dt = 0$$

then the error signal becomes

$$e_z = - \int \omega_{z_1} dt \quad (20)$$

## V. ERROR SIGNAL ATTITUDE CONTROL SYSTEM FORMED BY SENSED SIGNALS USING A THREE GIMBAL PLATFORM AND A GROUP OF STRAP-DOWN RATE GYROS

### 1. General description

As an example, we will separately discuss the ways to calculate the matrix B and the attitude control signals according to their sensed signals when a three gimbal platform and a group of strap-down rate gyros are mounted in the vehicle. In addition, the corresponding theoretical structural diagrams of the attitude control system are also given.

### 2. Attitude control error signals formed by the frame angle signals of a three gimbal platform

(1) The mounting of the platform and the calculation of the matrix B.

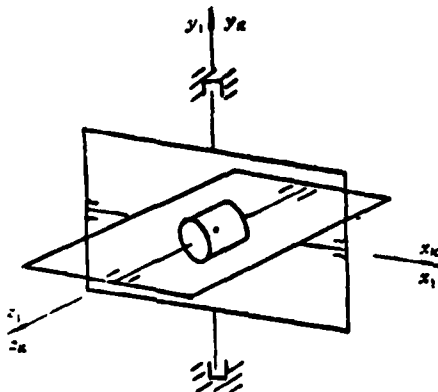


Figure 4. The Relationship Between the Initial State Coordinate System  $Z_1$  and  $Z_k$

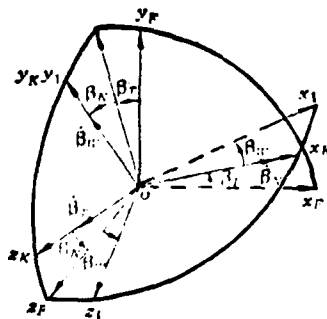


Figure 5. The Relationship Between the Flight Coordinate System  $Z_k$  with  $Z_1$  and  $Z_p$

We used the platform frame structure and the mounting arrangement as shown in Figure 4 as an example to provide the equations to calculate the matrix B. In the critical state, the  $Z_K$  coordinate system is parallel to the  $Z_1$  coordinate system where  $Z_K$  is the coordinate system of the platform frame axes (the origin of this coordinate system 0 is located at the intersection of the internal-external frame axis and the platform body axis,  $ox_K$  axis is solidly connected to the internal frame axis,  $oy_K$  axis is solidly connected to the external frame axis,  $oz_K$  axis is solidly connected to the platform body axis). During launching the coordinate system  $Z_1$  is parallel to  $Z_F$  or it is rotated by  $90^\circ$  around  $oz_F$ . In flight, the relations between the coordinate systems  $Z_K$ ,  $Z_1$  and  $Z_F$  are as shown in Figure 5 where  $\beta_T$  is the turning angle of the platform internal frame corresponding to the platform body axis,  $\beta_N$  is the turning angle of the platform external frame corresponding to the internal frame axis, and  $\beta_W$  is the turning angle of the aeronautical vehicle corresponding to the platform external frame axis; they are the frame angles of the platform. The matrix B can be expressed using the platform frame angles as

$$B = B_K = (\beta_W)(\beta_N)(\beta_T) \quad (21)$$

where

$$(\beta_W) = \begin{bmatrix} \cos \beta_W & 0 & -\sin \beta_W \\ 0 & 1 & 0 \\ \sin \beta_W & 0 & \cos \beta_W \end{bmatrix}$$

$$(\beta_N) = \begin{bmatrix} 1 & 0 & 0 \\ 0 & \cos \beta_N & \sin \beta_N \\ 0 & -\sin \beta_N & \cos \beta_N \end{bmatrix}$$

$$(\beta_T) = \begin{bmatrix} \cos \beta_T & \sin \beta_T & 0 \\ -\sin \beta_T & \cos \beta_T & 0 \\ 0 & 0 & 1 \end{bmatrix}$$

After calculation the elements of the matrix B are

$$\begin{aligned}
b_{11} &= \cos \beta_w \cos \beta_r - \sin \beta_w \sin \beta_N \sin \beta_r \\
b_{12} &= \cos \beta_w \sin \beta_r + \sin \beta_w \sin \beta_N \cos \beta_r \\
b_{13} &= -\sin \beta_w \cos \beta_N \\
b_{21} &= -\cos \beta_N \sin \beta_r \\
b_{22} &= \cos \beta_N \cos \beta_r \\
b_{23} &= \sin \beta_N \\
b_{31} &= \sin \beta_w \cos \beta_r + \sin \beta_w \cos \beta_N \sin \beta_r
\end{aligned}$$

$$\begin{aligned}
b_{32} &= \sin \beta_w \sin \beta_r - \sin \beta_N \cos \beta_w \cos \beta_r \\
b_{33} &= \cos \beta_w \cos \beta_N
\end{aligned}$$

(2) Error signals to control the direction of the longitudinal axis

$\epsilon_y, \epsilon_z$  are still calculated according to Equations (9), (16) and (17). The matrix B in Equation (9) is calculated based on (21).

(3) Error signals to control the rotation around the longitudinal axis

(a) under slope stability

Substituting the corresponding elements of matrix  $B_k$  in Equation (19)", we get

$$\epsilon_z = -\frac{\lg \beta_N}{\cos \beta_w} \quad (22)$$

when we consider  $\beta_N=0, \epsilon_x=0$ , then the above equation can be simplified as

$$\epsilon_z = -\beta_N \quad (23)$$

② under roll stability

In order to obtain  $\epsilon_x$ , we must add another rate gyro which is sensitive to the signal  $\omega_{x1}$  to the signals  $\omega_{x1}$  in Equation (20) or to carry out complicated data processing with respect to the frame angle signals. In general, roll stability is not used for such a three gimbal platform because the frame looking phenomenon may occur.



(4) Principle structural diagram of the attitude control system

We are only providing the principle structural diagram of the attitude control system under slope stability conditions (Figure 6).

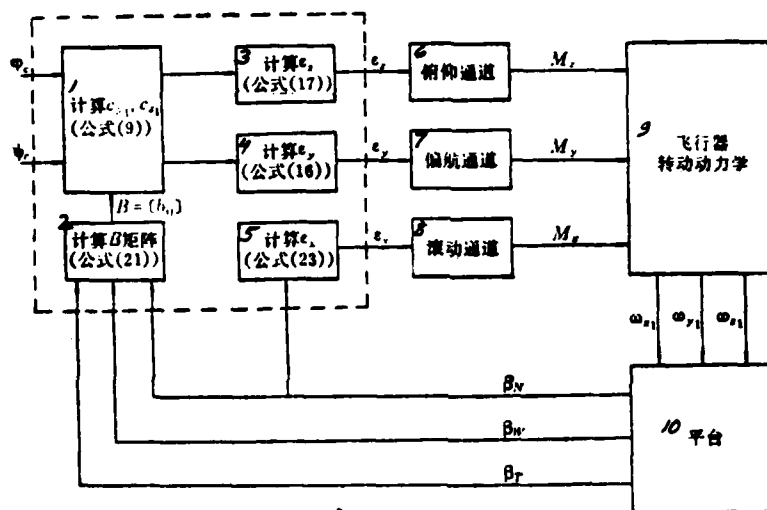


Figure 6. Principle structural diagram of the attitude control system of aeronautical vehicles with platforms under slope stability conditions

Key: 1--calculate...(Equation...; 2--calculate matrix...(Equation...; 3--calculate...(Equation...; 4--calculate...(Equation...; 5--calculate...(Equation...; 6--tilt channel; 7--deviation channel; 8--roll channel; 9--rotational dynamics of the aeronautical vehicle; 10--platform

$\varphi_n, \psi_n$  are the system input,  $\lambda, \beta_r, \beta_w, \beta_v$  are the feedback signals. Through calculation the error signals  $e_{\lambda}, e_{\psi}, e_{\beta}$  are formed. On the basis of these error signals (sometimes angular velocity feedback signals are also required and it is shown in the figure), the roll channel, deviation channel and the tilt channel control the executing mechanisms according to certain control regularities

to form the control torques  $M_x, M_y, M_z$  around the three axes of the body coordinate system of the aeronautical vehicle. These torques control the rotational motion of the vehicle. The variation of attitude of the vehicle is obtained from the error signals calculated using the platform sensed and platform sensed frame angle signals as the feedback signals.

### 3. Attitude control error signals formed using strapdown rate gyro sensed signals

- (1) Using the rate gyro sensed signals to calculate the matrix B.

A group of strapdown type of rate gyros are used to sensor the angular velocities  $\omega_{x_1}, \omega_{y_1}, \omega_{z_1}$  along the coordinates of the body coordinate system. From these signals we can solve based on Equation (24) for the transformation of the four element numbers  $q$  ( $q = [q_0, q_1, q_2, q_3]^T$ ) from the  $Z_F$  coordinate system to the  $Z_1$  coordinate system and then use Equation (25) to calculate the matrix B expressed by the elements of the four element number. The relationship between the four element number  $q$  and the angular velocities  $\omega_{x_1}, \omega_{y_1}, \omega_{z_1}$  satisfy the following differential equation

$$\begin{bmatrix} \dot{q}_0 \\ \dot{q}_1 \\ \dot{q}_2 \\ \dot{q}_3 \end{bmatrix} = \frac{1}{2} \begin{bmatrix} 0 & -\omega_{x_1} & -\omega_{y_1} & -\omega_{z_1} \\ \omega_{x_1} & 0 & \omega_{z_1} & -\omega_{y_1} \\ \omega_{y_1} & -\omega_{z_1} & 0 & \omega_{x_1} \\ \omega_{z_1} & \omega_{y_1} & -\omega_{x_1} & 0 \end{bmatrix} \begin{bmatrix} q_0 \\ q_1 \\ q_2 \\ q_3 \end{bmatrix} \quad (24)$$

The matrix B can be expressed by the equation using the four element number  $q$  as

$$B = B_q = (b_{ij}) \quad (25)$$

where

$$\begin{aligned}
b_{11} &= q_0^2 + q_1^2 - q_2^2 - q_3^2 \\
b_{12} &= 2(q_1 q_2 + q_0 q_3) \\
b_{13} &= 2(q_1 q_3 - q_0 q_2) \\
b_{21} &= 2(q_1 q_2 - q_0 q_3) \\
b_{22} &= q_0^2 - q_1^2 + q_2^2 - q_3^2 \\
b_{23} &= 2(q_2 q_3 + q_0 q_1) \\
b_{31} &= 2(q_1 q_3 + q_0 q_2) \\
b_{32} &= 2(q_2 q_3 - q_0 q_1) \\
b_{33} &= q_0^2 - q_1^2 - q_2^2 + q_3^2
\end{aligned}$$

(2) Error signals to control the direction of the longitudinal axis

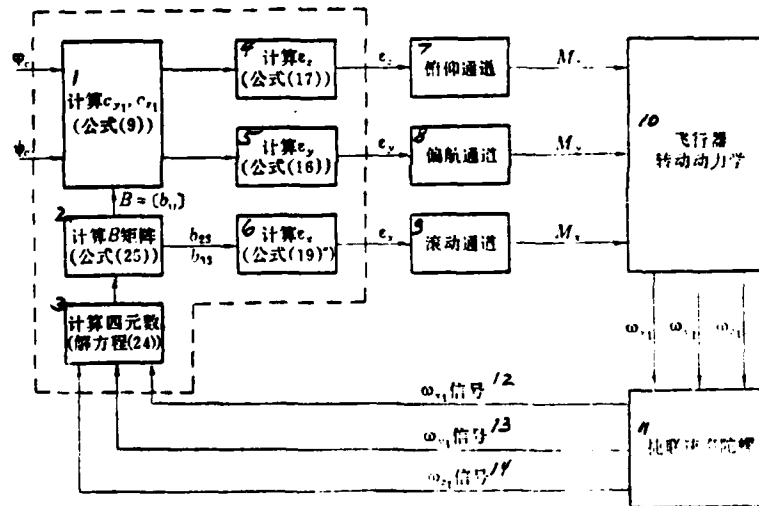


Figure 7. Principal structural diagram of an attitude control system with strapdown rate gyros under slope stability conditions  
 KEY: 1--calculate..(Equation..; 2--calculate..(Equation..; 3--calculate the four element number (solve equation (24)); 4--calculate..(Equation..; 5--calculate..(Equation..; 6--calculate..(Equation..; 7--tilt channel; 8--deviation channel; 9--roll channel; 10--rotational aerodynamics of aeronautical vehicles; 11--strapdown rate gyro; 12-- $\omega_{kl}$  signals; 13-- $\omega_{y1}$  signals; 14-- $\omega_{z1}$  signals

$\epsilon_1, \epsilon_2$  are still calculated based on Equations (9), (16) and (17). The matrix B in Equation (9) can be calculated using Equation (9).

(3) Error signals to control the rotation around the longitudinal axis

(1) under slope stability

$\epsilon_x$  is still calculated according to Equation (19)" where  $b_{23}$  and  $b_{35}$  are calculated based on Equation (25).

(2) under roll stability

$\epsilon_x$  is calculated according to Equation (20) when  $\omega_{x1}$  is the  $\omega_{x1}$  signals sensed by the strapdown rate gyros.

(4) Principal structural diagram of the attitude control system

The principal structural diagrams of the attitude control systems under slope and roll stability are shown in Figures 7 and 8 respectively.

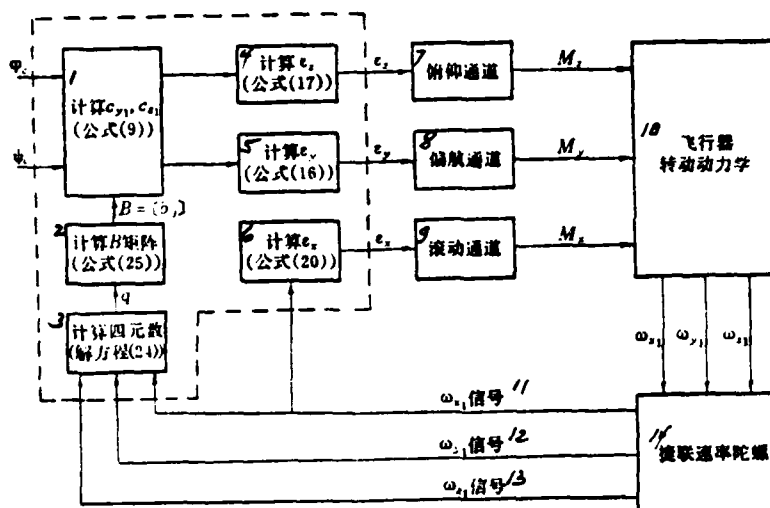


Figure 8. Principal structural diagram of an attitude control system for an aeronautical vehicle with strapdown rate gyros under roll stability conditions

Key: 1--calculate...(Equation..; 2--calculate...(Equation..; 3--calculate the four element number (solve equation (24)); 4--calculate...(Equation..; 5--calculate...(Equation..; 6--calculate...(equation..; 7--tilt channel; 8--deviation channel; 9--roll channel; ;10--rotational aerodynamics of aeronautical vehicles; 11-- $\omega_{x1}$  signals; 12-- $\omega_{y1}$  signals; 13-- $\omega_{z1}$  signals; 14--strapdown rate gyros

## REFERENCES

- (1) George W Cherry, "Design Principles for an Integrated Guidance & Control System for the Lunar Excursion Module". by AIAA 4th Manned Space Flight Meeting. October 11-13 pp 145-157
- (2) B P. Ickes, "A New Method for Performing Digital Control System Attitude Computation Using Quaternions". AIAA Journal vol 8 No 1 1970 pp 13-17.

# ON THE APPLICATION OF SELF-ADAPTIVE FLIGHT CONTROL SYSTEM BASED ON ENERGY BALANCE THEORY

Li Lichun

Institute of Automatic Flight Control System

## ABSTRACT

The application of the self-adaptive control theory in the flight control of aircraft has been studied for many years both here and abroad. However, there are very few plans which are actually practical. On the basis of the requirements of the development of our domestic flight control of aircraft, we carried out an actual experiment on the energy balance theory plan and offered an improved practical scheme. It was preliminarily established through experiments and flight tests that this scheme does not require test signals, is structurally simple, has better conveyance in adjusting parameters and basically is not affected by the input signal. It is more hopeful to be used in applications. This paper briefly described the selection of the scheme, design analysis, developmental experiments and major results of the flight tests for the open loop system. The design principle has been discussed in depth.

## I. INTRODUCTION

In the field of self-adaptive flight control, there must have been several tens of plans previously proposed or currently under study abroad. In our country, we have also carried out several

Received in February of 1979

studies. The major problems exposed can be summarized as:

- The excitation of the required test signals causing undesired aircraft motion;
- the poor certainty of the adjusted parameters, one defined flight attitude can correspond to several adjusted values;
- the self-adaptivity is affected by the input forms;
- the unsatisfactory convergence and following up of the adjusted parameters;
- the stability problems brought about to the entire system by the self-adaptative controller, and
- the complexity of the structure which makes it hard to materialize.

Because there are no satisfactory solutions to these problems, despite that the self-adaptive technology was presented for over 20 years, the flight control system still follows the atmospheric data program adjustment method. Lately due to the appearance of the excess degree electric transfer and the constant control planning flight control systems, the program adjustment method was found to be difficult to satisfy various requirements of the new systems. Therefore, the need for a self-adaptive control system is becoming more and more urgent.

On the basis of our analysis, we selected the self-adaptive system based on the energy balance theory to carry out a study on its practicality and improvements. It was applied to the self-stabilizing system and the automatic piloting device of high performance aircrafts. Through a wide range of development experiments and principle test flights, it indicated that the major self-adaptivity of the scheme can coincide with the requirements of the design. It does not require test signals, is structurally simple and is easy to realize. It is a hopeful practical plan. The core of the plan is the energy balance detector which detests the high frequency and low frequency energy components in the feedback or

error signals of the system under control. The adjustable element increases (when the low frequency energy dominates) or decreases (when the high frequency energy dominates) the gain of the system according to the difference of these two energies to bring the high and low frequency energies to a balance. Through the assurance in the design, the energy balance principle is basically in agreement with the flight quality targets.

## II. SYSTEM IMPROVEMENT SCHEME

The original energy balance plan (i.e., the early Marx system [1]) cannot satisfy the practical requirements of flight control. The scheme [2] obtained after applied research abroad still has many problems. They are mainly attributed to the effect of manipulation format as well as the poor convergence and abnormality of the adjusted parameters during the interference by wind, etc. The improved plan provided by this study can be explained by the longitudinal direction control-stabilization system as shown in Figure 1. The upper half of the diagram is a dynamic state control-stabilization system. The stabilization feedback circuit is used to increase the short cycle resistance and the electric control (increasing control) feedback circuit is used to compensate the loss of the dynamic state manipulation reaction after stabilization. The lower half is a self-adaptive control device. The major improvements can be summarized as the following:

(1) When it is applied to the automatic stabilization system, the input signals of the self-adaptive control device should not be the error signals of the system. This is because they contain a larger steady state component which is disadvantageous for spectral analysis. The feedback signals (from the gyros) should be used as the signal source for the energy detector.

(2) The gains of the control and the stabilization signals should be adjusted according to the same pattern. This not only



can simplify the structure but also is the desired form for flight quality.

(3) In order to decrease the effect of the manipulation format, a front load filter was installed.

(4) A second variable gain return circuit was installed in the band filter to provide a variable (floating) energy balance point to improve the convergence of the adjusted parameters.

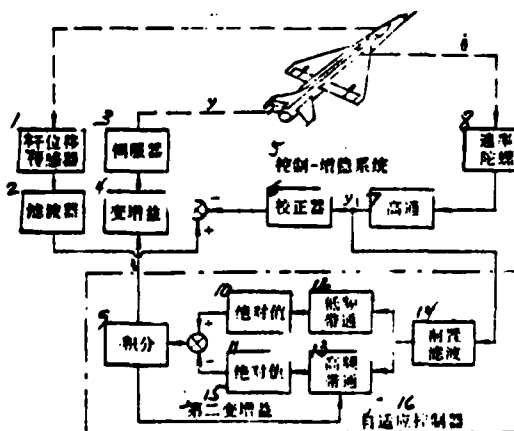
(5) The combination of the second variable gain circuit and the nonlinear electronic variable gain amplifier can make the energy balance point and the optimal gain value to be basically the same.

(6) Based on the characteristics of the domestic aircraft, we properly equipped the band filter with the basic parameters to make it possess good adaptivity and generality.

These improvements have already been materialized in early sample products. They were successfully proven through simulated ground tests and open-loop test flights.

Figure 1. Self-adaptive longitudinal direction control-stabilization system

Key: 1--lever displacement sensing device; 2--filter; 3--servo device; 4-- variable gain; 5--control-stabilization system; 6--calibration device; 7--high passage; 8--rate gyro; 9--integral; 10--absolute value; 11--absolute value; 12--low frequency band; 13--high frequency band; 14--front filter; 15--second variable gain; 16--self-adaptive control device



132

The close circuit transfer function of the stabilization back circuit is:

$$\Phi(P) = \frac{j}{x} = \frac{K_1 \left( P + \frac{1}{T_s} \right) \left( P + \frac{1}{T_i} \right) (P^2 + 2\zeta_s \omega_s P + \omega_s^2)}{(P^2 + 2\zeta_s \omega_s P + \omega_s^2) (P^2 + 2\zeta_s \omega_s P + \omega_s^2) \left( P + \frac{1}{T_i} \right) + K_D K_1 P \left( P + \frac{1}{T_i} \right)} \quad (1)$$

where  $K_1 = K_c K T_s \omega_s^2$ ,  $K_i = K_i \omega_s^2$ ,  $K_c = K_c K_s$ . The root trace schematic diagram of this simplified fifth order system is as shown in Figure 3. For the energy balance self-adaptive design, the major concern is the stability of the boundary of the main system (the intersection of the root trace and the imaginary axis) and the relationship between the open loop gain ( $K_D$ ) and the quality of the dynamic state. The calculated results obtained from the two boundary conditions of the selected high performance aircraft are shown in Table 1 (close loop main root). Under the constant gain conditions, when  $K_D=1$ , a barely acceptable dynamic state quality can be obtained. For the high altitude small dynamic pressure boundary condition, the resistance is still not sufficient which means the gain is small, while for the medium altitude large dynamic pressure boundary condition the resistance is too large and the stability storage is insufficient (only 6 dB gain storage) which means the gain is too large. Apparently, if the gain of the former can be increased to about  $K_D=2$ , and the gain of the latter condition can be decreased to about  $K_D=0.5$  (gain storage reaches 12 dB), then it is possible to obtain more ideal dynamic state quality. This is the basic problem which should be solved in the self-adaptive control method. In addition, the self-adaptive control system should reflect the maximum high frequency energy from the self-resonance point ( $\omega_s \approx 30$ ) of the main system in order to rapidly decrease the system gain under special conditions to assure the safety of the flight.

TABLE 1

$K_D$	$H=20公里, M=1.5$			$H=12.3公里, M=2.05$		
	$\omega_A$	$\zeta_A$	$2\zeta_A\omega_A$	$\omega_A$	$\zeta_A$	$2\zeta_A\omega_A$
0.25	—	—	—	7.00	0.20	4.15
0.50	—	—	—	8.20	0.43	7.08
1.00	3.37	0.35	2.38	8.85	0.79	14.0
2.00	3.42	0.64	4.40	9.25	1.47	27.2
4.00	3.40	1.33	9.05	—	—	—

Key: 1--kilometer

## 2. Analysis of the self-adaptive back circuit

### (1) Design of the energy balance detector

The energy balance detector actually measures the energy spectrum of the signals through sensing the frequency and the resistance of the input signals. The energy balance guideline should be properly determined based on the requirements of the flight quality and the dynamic characteristics of the main system. Under the actual conditions in our study, the natural frequency distribution characteristics under various flight conditions are shown in Figure 4. They also represent the common characteristics of high performance aircraft. The flight conditions with medium frequencies can give ideal flight qualities with proper open loop gain values. Therefore, it is proper to choose the condition  $\omega_n=5$  and  $K_D=1$  as the energy balance condition. For that it is necessary to make the frequency characteristics of the high frequency and low frequency band filters intersect at  $\omega=5$  radian/sec. Furthermore, it has also taken into consideration that the effects of the low frequency band filter on the minimum working frequency and the high frequency band filter on the self-resonance frequency of the system should be the strongest, respectively. From there we can preliminarily determine the amplitude-frequency characteristics of the energy balance detector which should be as shown in Figure 5. It should be noticed that

in order to avoid the gust interference an excessively high frequency energy is taken which is located in the frequency band above the self-resonance frequency of the system. The amplitude-frequency characteristics should be decreased according to a proper slope. On the basis of the above consideration, the design of the transfer functions of the two types of band filters is:

$$\left. \begin{aligned} \text{high frequency band } W_H(P) &= \frac{K_H P}{\left(\frac{P}{\omega_H}\right)^2 + 2\left(\frac{\zeta_H}{\omega_H}\right)P + 1} \\ \text{low frequency band } W_L(P) &= \frac{K_L T P}{(TP + 1) \left[ \left(\frac{P}{\omega_L}\right)^2 + 2\left(\frac{\zeta_L}{\omega_L}\right)P + 1 \right]} \end{aligned} \right\} \quad (2)$$

where  $\omega_H=30$ ,  $\omega_L=5$  (the final adjustment is 3),  $\zeta_H=\zeta_L=0.5$ ,  $T=0.5$ . In order to assure the working stability of the self-adaptive back circuit, the resistance of the band filter should be sufficiently large. But excessively high resistance would decrease the distinguishability of the flight condition. Therefore, it was chosen to be 0.5 as a compromise.

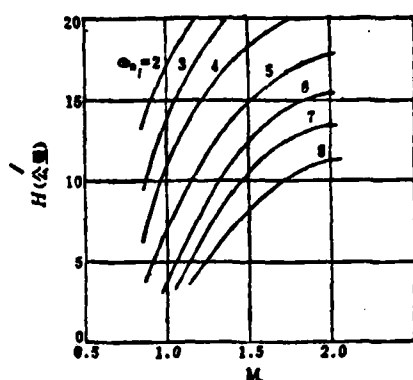


Figure 4. Distribution characteristics of the natural frequency  
Key: 1--kilometer

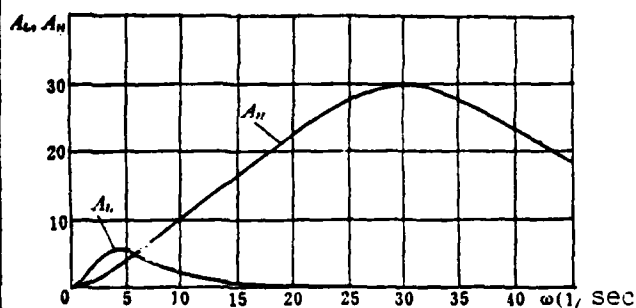


Figure 5. Amplitude-frequency characteristics of the energy balance detector

- (2) The design of the characteristics of the adjusted parameters and the improvements in convergence

Under the conditions that the front filter of the self-adaptive back circuit is not taken into consideration, the relationship between the energy difference between the high frequency and low frequency energies contained in the input signals and the adjusted gain can be calculated according to the following equation

$$\Delta K = -\frac{K_1 x^2}{\pi} \int_0^\infty \left| \frac{1}{P} W_{y1/x}(P) \right|^2 [ |W_n(P)|^2_{\omega=\omega_0} - |W_n(P)|^2_{\omega=\omega_1} ] d\omega \quad (3)$$

where  $\Delta K$ --self-adaptive adjusted parameter increment;  $K_1$ --gain of the integrator;  $W_{y1/x}(P)$ --transfer function of the main system feedback with respect to the input. The main system feedback transfer function under the conditions studied is

$$W_{y1/x}(P) = -\frac{y_1}{x} = \frac{b}{x} H_0(P) R(P) = \Phi(P) H_0(P) R(P) \quad (4)$$

Substituting Equation (1) into (4) and carrying out some proper simplification steps, we get

$$W_{y1/x}(P) \approx K_D \frac{K_1 P \left( P + \frac{1}{T_i} \right)}{(P^2 + 2\zeta_n \omega_n P + \omega_n^2) \left( P + \frac{1}{T_0} \right)} \quad (5)$$

In Equation (3), the multiplier  $(1/P)$  in front of the feedback transfer function represents the Laplace transformation of the step-jump input. Furthermore, Equation (3) can be finally written in the following form:

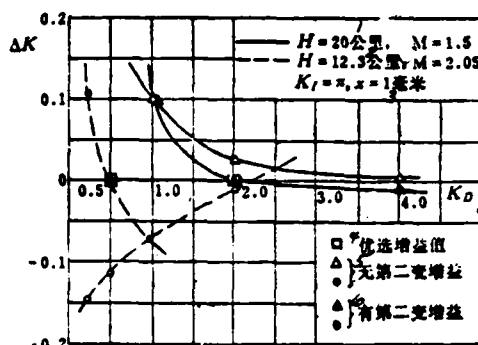
$$\Delta K = \int_0^\infty \frac{d\Delta K}{d\omega} d\omega \quad (6)$$

From Equation (6), it is possible to obtain the family of characteristic curves from  $d\Delta K/d\omega = f(\omega)$  according to various values of open loop gain. The covered area by the curves (algebraic sum) is the corresponding  $\Delta K$  value. Let us plot  $\Delta K = f(K_D)$  as the static characteristic curves as shown in Figure 6. It can be seen

that for small dynamic pressure boundary conditions the convergence of the gain is very slow due to the small high frequency energy amount. For large dynamic pressure boundary conditions, because of the insufficiency of the low frequency energy, it does not converge (gain divergence).

Figure 6. Static characteristics of the adjusted parameters.

Key: 1--kilometer; 2--kilometer; 3--mm; 4--priority gain value; 5--without second variable gain; 6--with second variable gain



The method to improve the convergence is to install a second variable gain in the self-adaptive feedback circuit. For example, it can be installed in the low frequency band filter. Its mathematical expression is

$$K_L = K_{L_0}(1 - m\Delta K) \quad (7)$$

where  $m$ --non-linear proportionality coefficient. When the gain is adjusted upward ( $\Delta K > 0$ ), it makes  $K_L$  decrease which actually artificially lowers the low frequency energy to promote an energy balance. This corresponds to the formation of a variable (floating) energy balance point. The second variable gain can also be installed in the high frequency band filter with the same effect. After the introduction of the second variable gain, the static characteristics  $\Delta K = f(K_D)$ , of the adjusted parameters can be calculated again according to the method described previously. The results are also shown in Figure 6 (the other group of curves). The second variable gain characteristics determined according to Equation (7) are actually designed to carry out compensation based on the degree of lack of energy and then providing proper values of  $K_L$  at various  $\Delta K$ . From the comparison of the two groups of curves in Figure 6, it can be seen that after introducing the second variable gain, the convergence obtained are obvious improvements. The large dynamic pressure boundary conditions become rapidly converging from non-

converging. However, it is more desirable to have an even faster rate of convergence for the small dynamic pressure boundary conditions. This can be achieved by adjusting partially the nonlinear coefficient as in Equation (7) to obtain a satisfactory solution.

### (3) Improvement on the effect of manipulation format

The above analysis was considered according to step-function input. If the input of a non-step function type of signals can cause a significant difference in the solution (general solution and particular solution) of the characteristic equations of the system from the ones obtained under the step-function input conditions, then under such an input format the self-adaptive back circuit would not be able to function normally. This is the motion the aircraft has, a dominant forced component, which does not reflect its natural frequency. This situation mainly occurs in slow rate manipulation regardless whether it is a trapezoidal wave, triangular wave or a discrete sine wave, etc.

The most simple and effective method to reduce the effect of the manipulation format is to install a front loading high passage filter ( $H_2$ ) at the input end of the self-adaptive control device to filter out the extremely low frequency component of the input. The guideline of the selection of the deflection frequency of the high passage filter is that it should be able to drastically reduce the extreme low frequency signals while not significantly affecting the frequency spectrum characteristics of the manual working frequency band of the system. Under the conditions studied, the normal working frequency band of the system is 3-8 radian/sec. Therefore, we should place the deflection frequency of the high passage filter at near the maximum natural frequency of the aircraft ( $\omega_n=8$ ). This means the high passage time constant is about 0.125 sec.



#### IV. RESULTS OF SIMULATED TESTS

It was verified through whole real object simulation tests that the system can effectively adjust the gain regardless of manipulation or under small disturbance in the aircraft. It does not require the excitation of the test signals and the adjusted gain value is basically the same as the priority value. Figure 7 shows the regularities of adjusted parameters under repeated manipulations. The parametric adjustment range is 0.36-2.0. The parametric adjustment sensitivity can reflect a 5 mm small lever manipulation. Figure 8 is the parametric adjustment process at high altitude at high speed with small amplitude of interference in the aircraft (blank noise). The average gust speed is as small as 1.8 m/sec and the system can still adjust parameters normally.

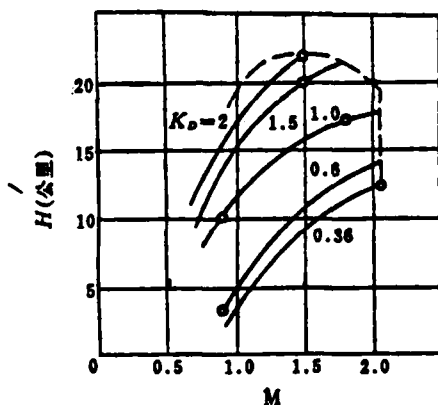


Figure 7. Regularities of self-adaptive adjustment of parameters

Key: 1--kilometer; 2--(degree/sec); 3--(degree); 4--m/sec; 5--(sec)

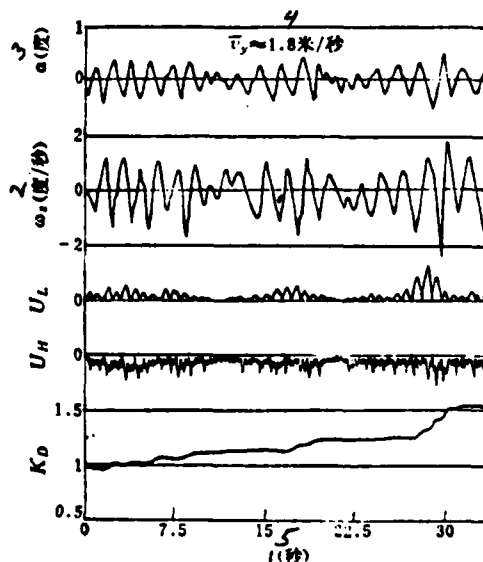


Figure 8. Effect of parametric adjustment under onboard interference.

In addition, we also carried out an experimental study on the transverse automatic piloting instruments. When the input signals are switched to the system error signals, the self-adaptive parametric adjustment is effective in a similar manner.

## V. PRINCIPAL OPEN LOOP TEST FLIGHT RESULTS

It was already discovered in the simulation tests that there is a certain ratio relation between the closed loop and open loop conditions in the energy balance self-adaptive system. Therefore, it is possible to indirectly verify the closed loop parametric adjustment characteristics through the open loop test flights.

On the selected high performance aircraft, the parts of open loop flight test system including the rate gyro, self-adaptive control device (electronic components), control desk and the gain indicator are all realized. The entire structural parameters of the system are the values experimentally adjusted on the ground. No changes were made during the test flight. Figure 9 shows the experimental results of three types of representative flight conditions (small dynamic pressure, medium dynamic pressure and large dynamic pressure) under manual manipulation. The open loop gain ( $K_D$ ) in the first condition was apparently adjusted upward. The second condition was the energy balance state, the open loop gain basically remained unchanged (slightly upward). The gain of third state was apparently adjusted downward. All the test flight results agree quantitatively with the simulation tests on the ground. It can also be shown from Figure 9 that the format of manipulation (displacement of the lever  $X_p$ ) was actually different every time. But it has no significant effect on the normal parametric adjustment capability. Figure 10 is the flight record of a low altitude interference flow flight. The flight altitude is below 2000 meters and the form of the interference flow is the medium or small discrete gust of  $\Delta n \leq \pm 0.4g$ . The corresponding tilt angular velocity  $\omega \leq \pm 2.5$  degree/sec. The interference flow is more obvious in the middle and

rear sections of the figure. In addition, there was a gentle climb correction motion by pulling the lever. We can see that under the influence of interference flow and manipulation, the open loop gain is closely following the variation of the flight condition (H from 1680 to 1950 m, Vi from 590 to 512 km/hour).

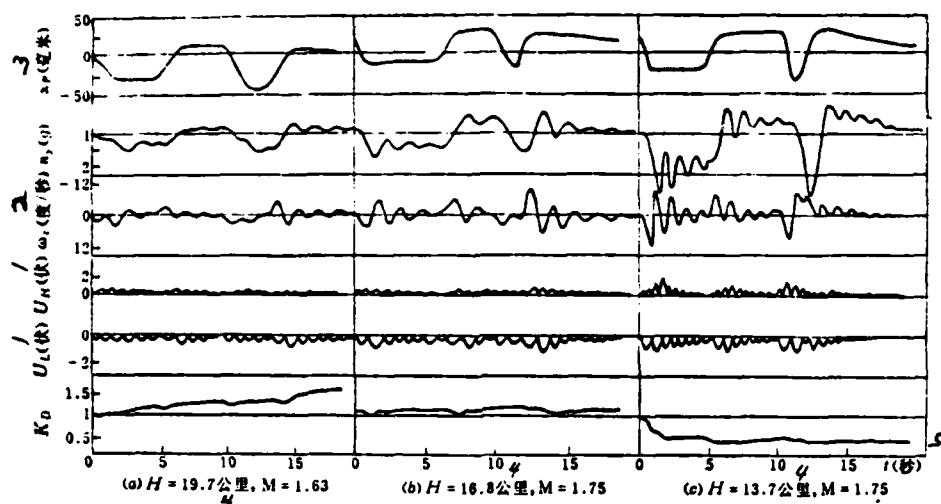


Figure 9. Open loop test flight results under classified conditions

Key: 1--volt; 2--degree/sec; 3--mm; 4--km; 5--(sec)

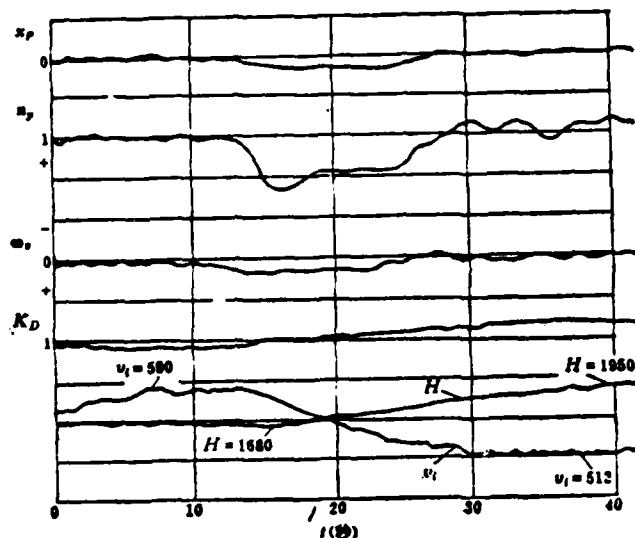


Figure 10. Test flight results of low altitude flight with interference flow

Key: 1--sec

## VI. CONCLUSIONS

Through the present stage of study, the major conclusions are as follows:

(1) There is a certain relevancy between the energy balance principle and the flight quality. The main design consideration is to make the energy balance obey the requirements of the flight quality.

(2) The improved plan is mainly to solve the convergence of the adjustment of parameters, the effect of the manipulation format and other practical problems. This plan is effective when applied to the longitudinal direction system. For a transverse system, it is effective in the same manner with respect to the adjustment of a single parameter or multiple parameters of similar principle.

(3) The work to follow is the closed loop flight demonstration and the application verification.

#### REFERENCES

- [1] Adaptive Control System, E. Mishkin and L. Braun, 1961.
- [2] U. S. Patent, 3, 216, 676.

#### Abstract

In this paper an adaptive flight control system for the longitudinal axis based on energy balance theory is described. A practical improved scheme and design details are presented, and preliminary evaluation from simulation and flight tests is made. The system exhibits better convergence in adjusting parameters and better performance of following up without testing signal. The system's architecture is simple and practicable. Selection of the scheme, design analysis, and brief results of the flight test for the open loop system, especially convergence of adjusting parameters and how to improve the effect of the input signal types are discussed.

## DIGITAL FILTER NETWORK DESIGN BY USING OBSERVERS

Beijing Electrical Engineering Design Department

Zhong Fuzhong

### ABSTRACT

This paper introduces a method to design digital filter networks using "observers". This method is to first provide the required close loop system pole positions and then obtain the digital filter network which satisfies the system characteristics. The commonly used logarithmic frequency method is to choose a certain network depending on the experience of the designer on the basis of the characteristics of the open loop logarithmic frequency and then to approach the desired ideal characteristics of the system using the engineering graphic method. Apparently, the former relies on digital simulation calculations which heavily depends on the realization of network digital computer while the latter method counts solely on the experience of the designer which lays stress on the physical realization of the network.

In addition, this paper used the state vector and matrix vector representation to describe a problem in order to make it more convenient for the numerical program calculation of the digital network design. Thus, it is also more convenient to modify the design and to redesign for the cross-type of networks.

---

Received in January of 1979

## I. THE PRESENTATION OF THE PROBLEM

Before discussing the design of a digital filter network using "observers", let us review the attitude control problems in a simulation system as shown in Figure 1. This is a principle block diagram for an elastic tilt channel attitude control system with weak resistance and static instability.

Let us assume the state vectors of the system to be:

$$\dot{X} = AX + Bu \quad (1)$$

$$Y = m'X \quad (2)$$

$$u = -a'X \quad (3)$$

where  $X$ -- $n \times 1$  dimensional state spatial vector

$A$ -- $n \times n$  dimensional system characteristics matrix

$B$ -- $n \times 1$  dimensional system input sensor matrix

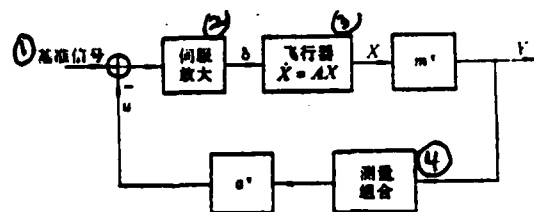
$m^T$ -- $1 \times n$  dimensional system output sensor matrix

$Y, u$ --input and output of the system, respectively

$a^T$ --system gain vector

Figure 1. Principle block diagram of the attitude control system

Key: 1--basic standard signal;  
2--follower amplifier; 3--  
aeronautical vehicle; 4--  
measuring combination



The so-called attitude control of the system is to obtain the relevant state components of the system (the object) using the measuring devices to force a feedback control in order to ensure the stability of the attitude of the system so that the pre-assigned mission of the flight can be accomplished. In the usual realization, in order to obtain better low frequency response and sufficient margin for high frequency stability, a combined calibration device must be introduced into the system. When comparing the simulation calibration network with the high reliability "digital filter

network" realized using a digital computer, it has disadvantages of structural complexity, poor reliability, limitation in physical realization, poor adaptability, etc., so that the satisfactory state response of the entire trajectory cannot be obtained. Here we raise the following questions: can we directly establish the relationship between the system required close loop pole positions and the gain vector  $a'$ ? Next, can we realize the indirect measurement of the state of the system? A hint is given from the "Kalman filter" concept: a "mathematical device" is installed on the system to estimate the state of the system in order to obtain the advanced signal of the system state component to realize the feedback to ensure system stability. Let us call this "mathematical device" realized by computer software as the "observer" [1]. The input of the "observer" is the direct sampling of the system's output and its output is the estimated value of the state of the system as shown in Figure 2.

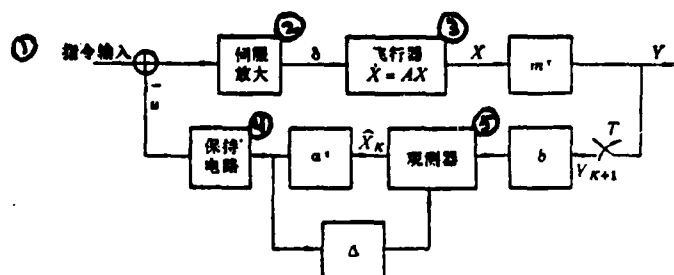


Figure 2. Object/observer close loop control

Key: 1--command input; 2--follower amplifier; 3--aeronautical vehicle; 4--maintenance electric circuit; 5--observer

The control scheme at this time is

$$U_k = -a' \hat{x}_k \quad (4)$$

where  $a'^T$  -- system gain vector  
 $\hat{x}_k$  -- estimated value of the state of the system

Apparently,  $a'^T$  and  $a^T$  are all gain vectors of the system. But  $a'^T$  has some new meaning: that is  $a'^T$  is determined by the given



close loop object pole positions through which the relationships between the control  $U_k$  with the system requires close loop object pole positions and the estimated values of the state of the system. Since the requirements of the system are directly reflected in the control signals to increase the flexibility of the system design, so that it is possible to design a satisfactory network to properly compensate the system characteristics.

## II. DIGITAL FILTER NETWORK DESIGN USING "OBSERVERS" [1]

The data sampling system corresponding to the Equation (1) system is:

$$X_{k+1} = \Phi X_k + \lambda u_k \quad (5)$$

$$Y_k = m^T X_k \quad (6)$$

where  $\Phi$ --the state transformation matrix of the system.

$$\Phi = L^{-1}[(SI - A)^{-1}] \text{ 或 } \Phi = \exp(AT) \quad (7)$$

$$\Delta = \int_0^T \Phi(t) B dt \quad (8)$$

The model of the observer is believed to be

$$\hat{X}_{k+1} = \hat{X}'_{k+1} + b(Y_{k+1} - \hat{Y}'_{k+1}) \quad (9)$$

where  $\hat{X}'_{k+1} = \Phi \hat{X}_k + \lambda u_k \quad (10)$

$$\hat{Y}'_{k+1} = m^T \hat{X}'_{k+1} \quad (11)$$

$b$ --gain vector of the observer

The physical meaning of the observation function (9) is: the estimate value  $\hat{X}_{k+1}$  of the state of the system at time  $t_{k+1}$  is equal to extrapolated estimated value  $\hat{X}'_{k+1}$  at that time plus a compensation term. The degree of compensation is determined by the gain vector  $b$  of the observer. From Equations (9) to (11), we get

$$\hat{X}_{k+1} = (I - bm)(\Phi \hat{X}_k + bY_{k+1}) + (I - bm)\lambda u_k \quad (12)$$

Therefore, the observer dynamic equation without the control ( $U_k$ ) feedback is:

$$\hat{x}_{k+1} = (I - bm')\Phi\hat{x}_k + bY_{k+1} \quad (13)$$

The observer characteristics matrix equation is

$$|ZI - (I - bm')\Phi| = 0 \quad (14)$$

In Equation (12), let

$$u_k = -\alpha'\hat{x}_k \quad (15)$$

and we obtain the close loop observer dynamic equation

$$\hat{x}_{k+1} = (I - bm')(\Phi - \Delta\alpha')\hat{x}_k + bY_{k+1} \quad (16)$$

Using Equations (5), (6), (9), (11) and (15), we get

$$X_{k+1} = (\Phi - \Delta\alpha')X_k + \Delta\alpha'(I - bm')\tilde{x}_k \quad (17)$$

where  $\tilde{x}_k$  -- error of estimated value of the observer;  $\tilde{x}_k = X_k - \hat{x}_k$ .

Equation (17) is the matrix vector equation of the object. Therefore, the characteristic equation of the object is

$$|ZI - (\Phi - \Delta\alpha')| = 0 \quad (18)$$

From Equations (15) and (16), the transfer function of the compensator can be obtained immediately as:

$$W_1(Z) = \frac{u(Z)}{Y(Z)} = \alpha' (ZI - G)^{-1} bZ = \frac{\alpha' \text{adj}(ZI - G) bZ}{|ZI - G|} \quad (19)$$

where

$$G = (I - bm')(\Phi - \Delta\alpha')$$

At this time, the principle block diagram of the digital control system is shown as in Figure 2.

The zero point of the compensator is:

$$\alpha' \text{adj}(ZI - G) bZ \quad (20)$$

Using the mathematical summarization method, it is not difficult to prove that Equation (20) and

$$\alpha' \text{adj}(ZI - \Phi) bZ \quad (21)$$

are equivalent [8], so Equation (19) can be transformed into:

$$W_1(Z) = \frac{u(Z)}{Y(Z)} = \frac{\alpha' (\text{adj}(ZI - \Phi)) bZ}{|ZI - G|} \quad (22)$$

The extreme points of the compensator become:

$$|ZI - G| \triangleq p(Z) = Z^n - p_1 Z^{n-1} - \dots - p_{n-1} Z - p_n \quad (23)$$

where the coefficients  $p_i$  are obtained using the "progressive method" [8] in order to be realized using a digital computer program, i.e.,

$$p_i = -\frac{1}{i} I_i K_i, \quad i = 1, 2, \dots, n \quad (24)$$

where  $K_i = GQ_{i-1}$ ,  $Q_i = K_i - p_i I_i$ ,  
 $Q_0 = I$  (unit matrix).

### III. ACTUAL DESIGN EXAMPLES

#### 1. Control of solid body aeronautical vehicles

Let us study the system given by Equation (1) and assume

$$A = \begin{pmatrix} 0 & 1 \\ u_\alpha & 0 \end{pmatrix}, \quad X = (\varphi, \dot{\varphi}) \quad (25)$$

$$B = \begin{pmatrix} 0 \\ e \end{pmatrix}, \quad m' = (1, 0) \quad (26)$$

where  $e$ --control torque gradient

$u_\alpha$ --aerodynamic torque coefficient

$\varphi$ --tilt angle of the aeronautical vehicle

$\dot{\varphi}$ --angular speed of the tilt of the aeronautical vehicle

#### (1) Design objectives

In the engineering realization, an actual higher order system is very frequently simplified to a classical second order system with a pair of main guidance control poles. Therefore, in the  $S$  region there is

$$S_{1,2} = -\lambda \pm j\Omega$$

where  $\lambda = \xi\omega$ ,  $\Omega = \sqrt{1 - \xi^2}\omega$

$\xi$ --system resistance coefficient

$\omega$ --non-resistance natural frequency of the system.

Now, it is required for the system to have

$$\xi \geq 0.5, \omega = 6.1/\text{sec}$$

which corresponds to requiring that the pair of main guidance control poles are located in the Z plane:

$$Z_{1,2} = e^{-(\pm j/6.1)T} \quad (27)$$

where T--sampling period; taking T=0.01 sec.

(2) Determine  $\alpha^t$  according to the given close loop object pole points  $Z_{1,2}$ .

Using Equation (7), we obtain

$$\Phi = e^{AT} = \begin{pmatrix} 1 & T \\ uT & 1 \end{pmatrix} \quad (28)$$

Again, we can obtain from Equation (8):

$$\Delta = \int_0^T \Phi(t) B dt = \begin{pmatrix} eT^2 \\ 2 \\ eT \end{pmatrix} \cong \begin{pmatrix} \Delta_1 \\ \Delta_2 \end{pmatrix} \quad (29)$$

and let

$$\alpha' = (\alpha_1, \alpha_2)$$

Therefore, on the basis of Equation (18) and using the Vieta principle [7], we get:

$$\left. \begin{aligned} \Delta_1 \alpha_1 + \Delta_2 \alpha_2 &= 2 - (Z_1 + Z_2) \\ (T\Delta_2 - \Delta_1) \alpha_1 + (\Delta_1 uT - \Delta_2) \alpha_2 &= (uT^2 - 1) + Z_1 Z_2 \end{aligned} \right\} \quad (30)$$

Substituting the given parameters into the equation, we get

$$\alpha' = (\alpha_1, \alpha_2) = (2.313, 0.2567)$$

### 3. Determine b based on the given pole positions of the "observers"

In order to correspond to the model of the object, a second order "observer" is chosen. Therefore, the far given pole positions of the observer are:

$$Z_{3,4} = e^{-0.07T} = 0.55$$

Using Equations (26) and (28) as well as letting  $b = \begin{pmatrix} b_1 \\ b_2 \end{pmatrix}$  then there is

$$(I - bm')\Phi = \begin{pmatrix} 1 - b_1 & T - Tb_1 \\ u_1 T - b_2 & 1 - Tb_2 \end{pmatrix} \quad (31)$$

Therefore, according to Equation (14) and using the Vieta principle, we obtain

$$\left. \begin{aligned} b_1 + Tb_2 &= 2 - (Z_1 + Z_2) \\ (1 - u_1 T^2)(1 - b_1) &= Z_1 Z_2 \end{aligned} \right\} \quad (32)$$

Plugging the given parameters into it, we get

$$b_1 = 0.695, \quad b_2 = 20.5$$

(4) Transfer function of the compensator

Using the results obtained above and according to Equation (22), we get

$$W_1(Z) = \frac{6.89(Z - 0.925)Z}{Z^2 - 1.046Z + 0.841}$$

## 2. Analysis of solid body motion with elastic bending of aeronautical vehicles

Considering the solid body characteristics of the aeronautical vehicle after double elastic bending, the system is given by Equation (1) where

$$\begin{aligned} X &= (\varphi, \dot{\varphi}, q, \dot{q}_1, q_2, \dot{q}_2)' \\ B &= (0, e, 0, d_{11}, 0, d_{21})', \quad u = \delta \end{aligned}$$

$$A = \begin{pmatrix} A_1 & O \\ O & A_2 \end{pmatrix}, \quad A_1 = \begin{pmatrix} 0 & 1 \\ \mu_1 & 0 \end{pmatrix} \quad (33)$$

$$A_2 = \begin{pmatrix} -\rho_1 & \omega_{d1} \\ -\omega_{d1} & -\rho_1 \end{pmatrix}, \quad A_3 = \begin{pmatrix} -\rho_2 & \omega_{d2} \\ -\omega_{d2} & -\rho_2 \end{pmatrix} \quad (34)$$

where

$$\begin{aligned} \dot{q}'_1 &= \frac{\rho_1 q_1 + \dot{q}_1}{\omega_{d1}}, \quad \dot{q}'_2 = \frac{\rho_2 q_2 + \dot{q}_2}{\omega_{d2}} \\ \omega_{d1} &= \sqrt{1 - \xi_1^2} \omega_1, \quad \omega_{d2} = \sqrt{1 - \xi_2^2} \omega_2 \\ \rho_1 &= \xi_1 \omega_1, \quad \rho_2 = \xi_2 \omega_2 \end{aligned}$$

$\delta$ --helm deviation angle

$\xi_i, \omega_i$ --resistance and frequency of the  $i$ th vibrational mode, respectively

$q_i$ --generalized coordinate

$d_{i1}$ --generalized control parameter

$$m' = (K_p, K_r, K_{p1}, K_{r1}, K_{p2}, K_{r2}) \quad (35)$$

where

$$K_{p1} = K_p \alpha_1(X_p) - K_r \alpha_1(X_r) \rho_1$$

$$K_{r1} = K_r \alpha_1(X_r) \omega_{d1}$$

$$K_{p2} = K_p \alpha_2(X_p) - K_r \alpha_2(X_r) \rho_2$$

$$K_{r2} = K_r \alpha_2(X_r) \omega_{d2}$$

$K_p$ --gain of position gyro

$K_r$ --gain of rate gyro

$\alpha_1(X_p)$ --slope of the  $i$ th vibrational mode at  $(X_p)$  where the position gyro is installed

$\alpha_1(X_r)$ --slope of the  $i$ th vibrational mode at  $(X_r)$  where the rate gyro is installed.

The given pole positions of the close loop object are given in Table 3-1.

TABLE 3-1

first group	$Z_{1,2} = e^{-(3.8 \pm 2.86)T}$	second group	$Z_{1,2} = e^{-(3.2 \pm 0.18)T}$
-------------	----------------------------------	--------------	----------------------------------

The given pole positions of the observer are tabulated in Table 3-2.

TABLE 3-2

1 组 别	2 观测数	$Z_{3,4}$	$Z_{5,6}$	$Z_{7,8}$
3 第一组		$e^{-6T}$	$e^{-(10 \pm 10)T}$	$e^{-20T}$
4 第二组		$e^{-60T}$	$e^{-(78 \pm 78)T}$	$e^{-90T}$

Key: 1--group; 2--order of observation; 3--first group;  
4--second group

After using the methods in 1. to obtain  $\alpha^T$  and  $b$ , and then the transfer function of the compensator can be obtained according to Equation (22) as:

$$W_1(Z) = \frac{(Z^3 + R_1Z + R_2)(Z^3 + R_3Z + R_4)(l_1Z + l_2)Z}{Z^6 - p_1Z^5 - p_2Z^4 - p_3Z^3 - p_4Z^2 - p_5Z - p_6} \quad (36)$$

where

$$R_1 = -2e^{-\alpha_1 T} \cos(\omega_1 T), \quad R_2 = e^{-2\alpha_1 T},$$

$$R_3 = -2e^{-\alpha_2 T} \cos(\omega_2 T), \quad R_4 = e^{-2\alpha_2 T},$$

$$l_1 = a_1 b_1 + a_2 b_2, \quad l_2 = a_1 a_2 T b_1 - a_1 b_1 + a_1 b_2 T - a_2 b_2,$$

$p_i, i = 1, 2, \dots, 6$ , are obtained from Equation (23) [8].

Let

$$H_1(q) = W_1(Z) \Big|_{Z = \frac{1+q}{1-q}}$$

$$W_1(jv) = W_1(q) \Big|_{q = j e^{jvT}} \quad v = \omega T$$

then the logarithmic amplitude characteristics are

$$W_A = 20 \lg |H_1(jv)| \quad (37)$$

The phase characteristics are

$$W_\varphi = \angle H_1(jv) \quad (38)$$

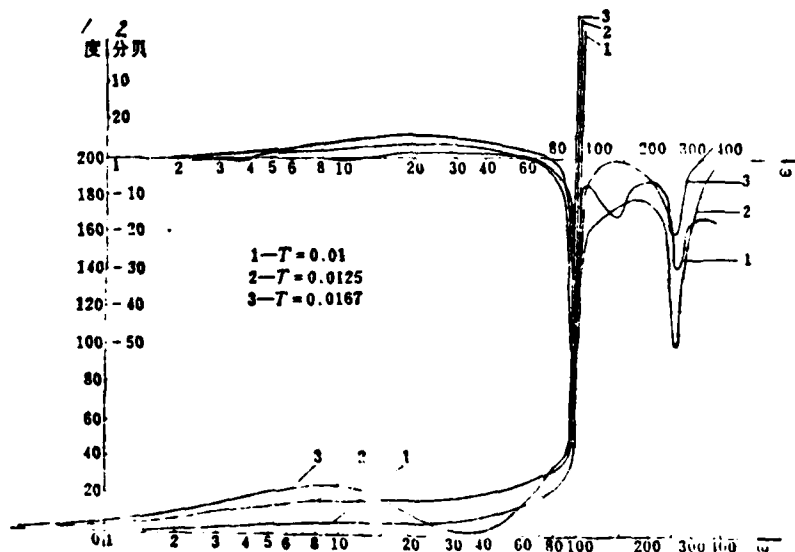


Figure 3. Taking off segment. Object pole points, the first group; observer pole points, the first group.

Key: 1--degree; 2--dB

The logarithmic amplitude-phase characteristics of the digital filter network obtained according to Equations (37) and (38) are shown in Figures 3-5.

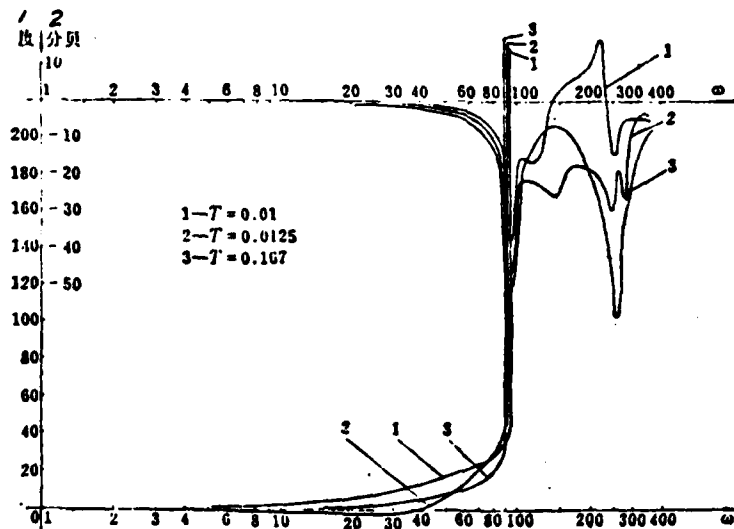


Figure 4. Taking off segment. Object pole points, the second group; observer pole points, the first group.

Key: 1--degree; 2--dB



TABLE 3-3

SYSTEM REQUIREMENTS	OBJECT POLE POINTS	OBJECT GAIN $\alpha^T$	
		$\alpha_1$	$\alpha_2$
resistance $\xi=0.7$ stability time $t_s=0.07$ sec	1st group	0.9964	0.3439
resistance $\xi=0.5$ stability time $t_s=1$ sec sec	2nd group	2.186	0.3746

From Figures 3 and 4 we can see the following two points:

(1) Because the close loop object pole points of the system are different, the low frequency characteristics of the network in Figure 3 is better than that in Figure 4. We can see from Table 3-3 that:

For the first group of object pole points the resistance is larger and the gain is smaller than the second group which makes the number of resonance of the system smaller and the stability better. Therefore, Figure 3 has better low frequency compensation characteristics when compared to Figure 4. From this we know that the object pole points are mainly influencing the low frequency characteristics of the networks.

(2) Due to the fact that the system close loop object pole points are different, the high frequency characteristics of the networks shown in Figures 3 and 4 are different. This is because the  $\alpha^T$  determined by the given object pole points moves the pre-given position of the pole point of the "observer" after the feedback of the  $U_k$  to the "observer". For that let us take a look at the output of the "observer" under solid body control conditions:

For simplicity, let us choose the fastest time observer which is  $Z_1=Z_2=0$ . Using Equation (32) to obtain  $b_1=1$ ,  $b_2=\frac{1}{T}$ , and then

using Equations (13) and (31), we get

$$\left. \begin{aligned} \hat{x}_1(Z) &= Y(Z) \\ \hat{x}_2(Z) &= \frac{Z - (1 - u_0 T^2)}{T Z} Y(Z) \end{aligned} \right\} \quad (39)$$

This is the output of the open loop observer.

If we make control  $U_k$  to feedback into the observer and take a second order adjustment principle which means letting

$\alpha' = \left( \frac{\alpha_1}{T^2}, \frac{\alpha_2}{T} \right)$ . The close loop observer output can be obtained using Equation (16):

$$\left. \begin{aligned} \hat{x}_1(Z) &= Y(Z) \\ \hat{x}_2(Z) &= \frac{Z - \left[ (1 - u_0 T^2) + \frac{e\alpha_1}{2} \right]}{T \left( Z + \frac{e\alpha_2}{2} \right)} Y(Z) \end{aligned} \right\} \quad (40)$$

Comparing Equations (39) with (40), we can see that the origin and the pole point of the observer are moved by  $\left( \frac{e\alpha_1}{2}, \frac{e\alpha_2}{2} \right)$ . Due to the difference in  $\alpha'$  (see Table 3-3), the pole points of the observers under the two conditions are different from Equation (40) which causes the difference in the high frequency characteristics in Figures 3 and 4. From this we know that the close loop observer pole point mainly affects the high frequency characteristics of the network.

Summarizing the above discussion, the unified selection of pole points and proper matching of object/observer can always find a network with the satisfactory high and low frequency characteristics. Thus, it properly treats the phenomenon that contradictory high and low frequency characteristics exist in conventional methods.

Comparing Figure 3 with Figure 6, we can see that Figure 6 is the logarithmic amplitude phase characteristics of a concave filter of the stable first order elastic resonance type obtained through Tustin transformation [4] on the basis of a continuous network. It can be shown from the figure that: the characteristic concave

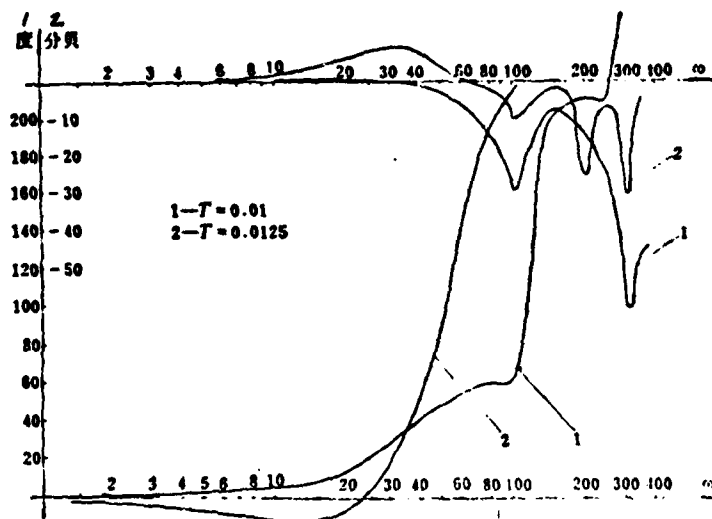
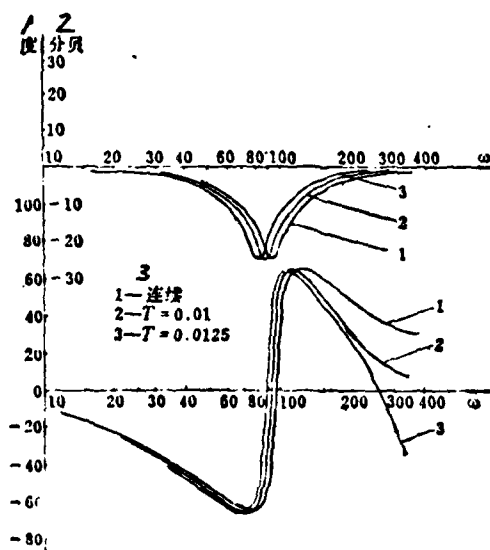


Figure 5 ( $\frac{u_0}{e}$ )...

Object pole point, 1st group; observer pole point, 1st group.  
Key: 1--degree; 2--dB



1--连续, 2-T=0.01, 3-T=0.0125.

Figure 6. Take-up segment. Continucus.

Key: 1--degree; 2--dB; 3--continuous;

TABLE 3-4

1 特征点	2 状态	3 指标	4 刚体控制		7 弹性稳定		10 说明
			5 幅裕度 $M$ (db)	6 相裕度 $\gamma$ (度)	8 一次弹性幅裕度 $m_1$ (db)	9 二次弹性幅裕度 $m_2$ (db)	
11 起飞段(某点)	12 补偿前		41	62	16 不稳定	17 不稳定	20 考虑回路总增益 (20lg 3.5 = 11db)
	13 补偿后		41	84	31	18	
$(\frac{u_1}{e})_{max}$	14 补偿前		10	66	18 不稳定	19 不稳定	21 考虑回路总增益 (20lg 2.8 = 9db)
	15 补偿后		10	106	4.8	12	

Key: 1--characteristic point; 2--state; 3--indicator; 4--solid body control; 5--amplitude margin; 6--phase margin  $\gamma$  (degree); 7--elastic stability; 8--first order elastic amplitude margin; 9--second order elastic amplitude margin; 10--remarks; 11--taking off segment (a certain point); 12--before compensation; 13--after compensation; 14--before compensation; 15--after compensation; 16--unstable; 17--unstable; 18--unstable; 19--unstable; 20--considering total gain of the return circuit; 21--considering the total gain of the return circuit

modulated frequency shifts to the left in an obvious manner with increasing sampling period  $T$ . From Figure 3 it shows that the characteristic concave modulated frequency of the network does not vary significantly with increasing  $T$ . This indicates that the requirements of  $T$  in the method introduced in this paper is lower which is the problem to be resolved in the digital network design.

Figures 3 and 5 are the logarithmic amplitude phase characteristics of the networks designed for the two classical characteristic points of a certain aeronautical vehicle respectively. From the figure it can be shown that: although their characteristics are different, yet the networks designed by taking  $T=0.0125$  for the two characteristic points are feasible. They all can obtain better compensation affect (see Table 3-4). This is because that the variation of the flight parameters are already considered in the network design. As for this point, it is also an obvious characteristic of this method as compared to other methods.

#### IV. CONCLUSIONS

This method is the direct network design in discontinuous regions. In the design proper treatment was made to the sampling delay. Therefore, for well designed networks, it is not necessary to consider the sampling delay compensation problem. In addition, this method considers a larger number of factors during the design process so that the flexibility of the network design is high and the applicability of networks obtained is also high. Actual design example shows that the effect of this method on the weak resistance static unstable elastic filter is very apparent. However, this method is also applicable to the design of other types and systems of filter networks.

Two points should be pointed: one of them is that the network design is carried out using a digital computer program on a computer on the ground. A large amount of numerical simulation computations is carried out with respect to various flight conditions and different systems to choose the proper network. First, the network is selected, then the network parameters are given. Then, the realization on a computer is very simple. Next, this method at the present moment relies on a trial method to solve the problem of properly matching the "object/observer" pole positions. Therefore, to seek for a better method to solve the problem is another area of research yet to be studied.

## REFERENCES

- [1] B. E. Bona, "Digital Filter Design Using Observers" 1971 Fifth Asilomar Conference on Circuits and Systems.
- [2] J. M. Johnson, "Digital Filter Using Observers Applied to ICBM Control Systems Design" AIAA Guidance and Control Conference, 1973.
- [3] D. G. Luenberger, "Observing the State of a Linear System" IEEE Transactions on Military Electronics, Vol MIL-8 No 1-4, 1963-1964.
- [4] G. L. Stater, "A Unified Approach to Digital Flight Control Algorithms" AIAA paper No 74-884, 1974.
- [5] A. L. Greensite, "Modern Control Engineering", 1970.
- [6] E. I. Jury, "Sampled-Data Control Systems", 1958.
- [7] Chou Paoyun, editor "Advanced Algebra", Higher Education Publishing Co., 1966.
- [8] Zhang Fuzhong, "A new method of digital filter network design", Communication in the Annual Meeting of the 1978 National Automation Science Meeting

## Abstract

A method of digital filter network design using observers is presented. This method consists in providing the required close loop system pole positions, and obtaining a digital filter network satisfying the characteristics of the system; whereas the conventional logarithmic frequency method is based on the open loop logarithmic frequency properties, in which the choice of the network depends on the experience of the designer in making system's properties approach the desired ideal properties by way of engineering graphical curves. The former method depends on digital simulation computation and lays stress on realization of the network design on a digital computer, but the latter method relies on designer's experience and lays stress on physical realization of the network design.

State vector and matrix vector representations are used in the numerical program calculation for digital network design through the computer. It makes modification and re-design work easier.

## ON THE DERIVATION OF BEZIER'S BASIC FUNCTIONS

Beijing Institute of Aeronautics and Astronautics

Shi Fazhong and Han Dackang

### ABSTRACT

In the book entitled "Numerical Control", Professor Bézier has given an elegant and detailed explanation on the Bézier curves and curved surfaces. The expressions of Bézier's basic functions are shown in (2) and (3) in this paper.

Bézier curves have a number of interesting and important geometric properties. They are the direct deduction of the properties of the Bézier basic functions. Up until this moment, there has not been any literature on the derivation of these functions.

This paper proved that these basic functions can be derived completely using three simple reasonable geometric requirements of the Bézier curves in two different ways.

### I. INTRODUCTION

In the area of computer assisted geometric design (CAGD), the method of structural curves and curved surfaces provided by Professor P. Bézier of France and the UNISURF system established based on this method is one of the most successful systems acknowledged by the international experts. In this publication [1], Bézier introduced the theoretical basis and applications of his method in detail.

---

Received in April of 1980

Chan Kensho and Wu Jiunhen [2] have carried out an even deeper and more rigorous study on the mathematical basis of this method.

The expression of the  $n$ th order Bézier curve is

$$\vec{P}(u) = \sum_{j=0}^n \vec{a}_j f_{n,j}(u) \quad 0 \leq u \leq 1 \quad (1)$$

where

$$\left. \begin{aligned} f_0(u) &\equiv 1 \\ f_j(u) &= \frac{(-u)^j}{(j-1)!} \frac{d^{j-1}}{du^{j-1}} \Phi_n(u) \quad (j=1, 2, \dots, n) \\ \Phi_n(u) &= [(1-u)^n - 1]/u \end{aligned} \right\} \quad (2)$$

They are also called the basic function of Bézier curves.

Vectors  $\vec{a}_0, \vec{a}_1, \dots, \vec{a}_n$  are connected sequentially from head to tail forming a polygon beginning at the starting point of  $\vec{a}_0$  and ending at the terminating point of  $\vec{a}_n$ , which is also called the characteristic polygon of Bézier curves.

From direct calculation we know that there is another expression for the basic functions (see [1])

$$f_{n,j}(u) = \sum_{i=j}^n (-1)^{i-j} C_n^i C_n^j (-u)^i \quad (3)$$

The basic functions have a series of properties (see [2] or [3]). From them the series of important and interesting geometric properties of Bézier curves can be derived. Among them, there are three basic properties.

(1) If we rearrange the sides of the characteristic polygon in the opposite direction and simultaneously change the vector directions of all the sides, we obtain the same Bézier curve but the orientation is opposite;

(2) the starting point (end point) of the curve is the first vertex (also the final vertex) of the characteristic polygon;



(3) at the starting point (end point) of the curve the  $k$ th order vector derivative is only dependent on the  $k$  sides of the characteristic polygon which are closest to this vertex and independent of any farther sides of the polygon.

But, we do not see how these basic functions are derived in the literature.

In this paper, two different methods were used to prove that on the basis of certain philosophy, the basic functions  $\{f_{n,j}(u)\}$  are uniquely defined by the three reasonable requirements (1), (2) and (3) of the curves.

## II. THREE BASIC REQUIREMENTS FOR THE BASIC FUNCTIONS

Since in this paper the discussion is limited to  $n$ th order Bézier curves, for simplicity of symbols, we will directly use  $f_j(u)$  as  $f_{n,j}(u)$ .

The three geometric properties of the curves described in the previous section are apparently assured by the three requirements for the basic functions  $\{f_j(u)\}$ .

(1) For  $u \in (0, 1)$  there is

$$f_j(u) = 1 - f_{n-j+1}(1-u) \quad (4)$$

This is because the Bézier curves defined by the reverse order directional characteristic polygon are defined as

$$\begin{aligned} \sum_{j=0}^n \vec{a}_j + \sum_{j=1}^n f_j(u)(-\vec{a}_{n-j+1}) &= \sum_{j=0}^n \vec{a}_j + \sum_{j=1}^n [f_{n-j+1}(1-u) - 1] \vec{a}_{n-j+1} \\ &= \vec{a}_0 + \sum_{j=1}^n f_j(1-u) \vec{a}_j \end{aligned}$$

(2)  $f_0(u) = 1$

$$\left. \begin{aligned} f_1(0) = f_2(0) = \dots = f_n(0) &= 0 \\ f_1(1) = f_2(1) = \dots = f_n(1) &= 1 \end{aligned} \right\} \quad (5)$$

(3) when  $k = 1, 2, \dots, j-1$

$$f_j^{(k)}(0) = 0 \quad (6)$$

when  $k = 1, 2, \dots, n-j$

$$f_j^{(k)}(1) = 0 \quad (7)$$

The two methods to derive the basic functions are explained in the following:

### III. THE FIRST METHOD

Since  $f_1(u), f_2(u), \dots, f_n(u)$  are all  $n$ th order polynomials and from property (2), we know that their constant terms are all zero, we can assume  $\{f_j(u)\}$  as

$$(f_1(u), f_2(u), \dots, f_n(u)) = (u \ u^2 \ \dots \ u^n)M \quad (8)$$

when  $M$  is an  $n$ th order constant coefficient matrix. To define the basic functions is actually to determine the coefficient matrix  $M$  on the right side of Equation (8).

Using  $u=1$  to substitute into both sides of Equation (8), we know from requirement (2) that

$$(1 \ 1 \ \dots \ 1) = (1 \ 1 \ \dots \ 1)M \quad (9)$$

which indicates that the sum of the elements of every column is equal to 1 for the matrix  $M$ .

It is not difficult to see from property (3) that  $M$  is a lower triangular matrix.

Let us define the following matrix

$$W(u) = \begin{bmatrix} f_1'(u) & f_2'(u) & \dots & f_n'(u) \\ f_1''(u) & f_2''(u) & \dots & f_n''(u) \\ \dots & \dots & \dots & \dots \\ f_1^{(n)}(u) & f_2^{(n)}(u) & \dots & f_n^{(n)}(u) \end{bmatrix}$$

After taking the first, second... $n$ th order derivatives on both sides of Equation (8), we get

$$W(u) = \begin{bmatrix} 1 & 2u & 3u^2 & \dots & nu^{n-1} \\ 0 & 2! & 6u & \dots & n(n-1)u^{n-2} \\ \dots & \dots & \dots & \dots & \dots \\ 0 & 0 & 0 & \dots & n! \end{bmatrix} M$$

Therefore,

$$W(0) = \begin{bmatrix} 1! & & & & \\ & 2! & & & \\ & & \ddots & & \\ & & & \ddots & \\ & & & & n! \end{bmatrix} M \quad (10)$$

$$W(1) = \begin{bmatrix} 1 & 2 & 3 & \dots & n \\ 0 & 2! & 6 & \dots & n(n-1) \\ \dots & \dots & \dots & \dots & \dots \\ 0 & 0 & \dots & 0 & n! \end{bmatrix} M \quad (11)$$

On the other hand, by taking the  $i$ th order derivation with respect to  $u$  on both sides of Equation (4), we can get

$$f^{(i)}(u) = (-1)^{i+1} f_{n-i,1}^{(i)}(1-u)$$

The above equation can be expressed in the matrix from

$$W(u) = \begin{bmatrix} 1 & & & & \\ & -1 & & & \\ & & 1 & & \\ & & & \ddots & \\ & & & & -1 \end{bmatrix} W(1-u)K \quad (12)$$

where  $K$  is the matrix which rearranges the columns of the  $n$ th order unit matrix in the reverse order, i.e.,

$$K = \begin{bmatrix} & & & & 1 \\ & & & 1 & \\ & & \ddots & & \\ & 1 & & & \\ 1 & & & & \end{bmatrix}$$

Very specially using  $u=0$  into Equation (12), there is

$$W(0) = \begin{bmatrix} 1 & & & & \\ & -1 & & & \\ & & 1 & & \\ & & & \ddots & \\ & & & & -1 \end{bmatrix} W(1)K$$

Substituting Equations (10) and (11) into both sides of the above equation, we get

$$\begin{aligned}
 M &= \begin{bmatrix} 1/1! & & & & \\ & 1/2! & & & \\ & & \ddots & & \\ & & & \ddots & \\ & & & & 1/n! \end{bmatrix} \begin{bmatrix} 1 & & & & \\ & -1 & & & \\ & & 1 & & \\ & & & -1 & \\ & & & & \ddots \end{bmatrix} \begin{pmatrix} 1 & 2 & 3 & \dots & n \\ 2 & 6 & \dots & n(n-1) & \\ & \ddots & & & \vdots \\ & & & & n! \end{pmatrix} MK \\
 &= \begin{bmatrix} 1 & & & & \\ & -1 & & & \\ & & 1 & & \\ & & & -1 & \\ & & & & \ddots \end{bmatrix} \begin{bmatrix} 1/1! & & & & \\ & 1/2! & & & \\ & & \ddots & & \\ & & & \ddots & \\ & & & & 1/n! \end{bmatrix} \begin{pmatrix} 1 & 2 & 3 & \dots & n \\ 2 & 6 & \dots & n(n-1) & \\ & \ddots & & & \vdots \\ & & & & n! \end{pmatrix} MK \\
 &= \begin{pmatrix} C_1^1 & C_2^1 & \dots & C_n^1 \\ & -C_2^2 & \dots & -C_n^2 \\ & & \ddots & \vdots \\ & & & (-1)^{n-1} C_n^n \end{pmatrix} MK
 \end{aligned}$$

If we let

$$A = \begin{pmatrix} C_1^1 & C_2^1 & \dots & C_n^1 \\ & -C_2^2 & \dots & -C_n^2 \\ & & \ddots & \vdots \\ & & & (-1)^{n-1} C_n^n \end{pmatrix}$$

then M should satisfy the matrix equation

$$M = AMK \quad (13)$$

Our objective is to solve for the lower triangular matrix M which satisfies Equation (13) and whose sum in every column is 1.

Let us assume  $M = (m_{ij})$ ,  $1 \leq i, j \leq n$ . Let us now compare the elements of  $i$ th row and  $j$ th column on both sides of Equation (13). We noticed that the  $j$ th column of the matrix MK happens to be the  $n+1-j$ th column of the matrix M, so

when  $M$  is a lower triangular matrix, if  $j > i$ , then  $m_{ij} = 0$ . From the above equation, we know

$$\sum_{k=i}^n C_k^i m_{k,n+1-i} = 0$$

which is

$$\sum_{k=n+1-l}^n C_q^{l, m_{k, n+1-l}} = 0$$

Here, there are  $\{j, n - (n - j) = j\}$  unknown quantities of  $m_{k, n+1-j} (k = n+1-j, \dots, n)$ . Since  $i = 1, 2, \dots, j-1$ , which means that the number of equations is  $j-1$ , it is short of that of the unknown quantities. The other equation is supplemented by condition (9). Therefore, we have the group of equations

$$\sum_{k=n+1-j}^n m_{k,n+1-j} = 1$$

$$\sum_{k=n+1-j}^n C_k^j m_{k,n+1-j} = 0$$

In order to simplify our symbols, we use  $j$  to replace the  $n+i-j$  in the above equations and then these equations can be expressed as

$$\left. \begin{aligned} m_{j,j} + m_{j+1,j} + \dots + m_{n,j} &= 1 \\ C_j^1 m_{j,j} + C_{j+1}^1 m_{j+1,j} + \dots + C_n^1 m_{n,j} &= 0 \\ &\dots\dots\dots \\ C_j^{r-1} m_{j,j} + C_{j+1}^{r-1} m_{j+1,j} + \dots + C_n^{r-1} m_{n,j} &= 0 \end{aligned} \right\} \quad (14)$$

Please note that if the superscript is larger than the subscript in these combinations then this combination should be considered as 0.

The Cramer method is used to solve this series of linear equations. For that, we have to calculate two determinant of some type. In order to find a unified method, we will prove the following:

The problem: Let us assume that  $k_1, k_2 \dots k_s$  are arbitrary non-negative integers, then

$$\begin{vmatrix} 1 & 1 & \dots & 1 \\ C_{k_1}^1 & C_{k_2}^1 & \dots & C_{k_s}^1 \\ \dots & \dots & \dots & \dots \\ C_{k_1}^{s-1} & C_{k_2}^{s-1} & \dots & C_{k_s}^{s-1} \end{vmatrix} = \frac{1}{1! \, 2! \, \dots \, (s-1)!} \prod_{i < m} (k_m - k_i)$$

Proof: Since for any non-negative integers  $p$  and  $q$  have the relationship

$$C_p^q = \frac{p(p-1)\dots(p-q+1)}{q!}$$

Therefore, after taking the common factor  $1/1!$  from the second row, the common factor  $1/2!$  from the third row, ...and the common factor  $1/(s-1)!$  from the last row, then adding the second row to the third row, and then adding  $(-2)$  times the second row and 3 times the third row to the fourth row..., finally the determinant becomes

$$\frac{1}{1! \, 2! \, \dots \, (s-1)!} \begin{vmatrix} 1 & 1 & \dots & 1 \\ k_1 & k_2 & \dots & k_s \\ k_1^2 & k_2^2 & \dots & k_s^2 \\ \dots & \dots & \dots & \dots \\ k_1^{s-1} & k_2^{s-1} & \dots & k_s^{s-1} \end{vmatrix}$$

This is the famous Vandermonde determinant which indicates that the conclusion of the problem is correct.

Applying the problem above to the calculation of the coefficient determinant of the series of equations in (14)

$$\begin{vmatrix} 1 & 1 & \dots & 1 \\ C_j^1 & C_{j+1}^1 & \dots & C_n^1 \\ \dots & \dots & \dots & \dots \\ C_j^{n-j} & C_{j+1}^{n-j} & \dots & C_n^{n-j} \end{vmatrix} = \frac{1}{1! \, 2! \, \dots \, (n-j)!} \times 1! \, 2! \, \dots \, (n-j)! = 1$$

when  $i$  suits  $j \leq i \leq n$ , then according to the Cramer method there is

$$m_{i,j} = \begin{vmatrix} 1 & 1 & 1 & 1 & 1 \\ C_j^{(1)} & C_{j+1}^{(1)} & 0 & C_{j+1}^{(1)} & C_n^{(1)} \\ \vdots & \vdots & \vdots & \vdots & \vdots \\ C_j^{(i-1)} & C_{j+1}^{(i-1)} & 0 & C_{j+1}^{(i-1)} & C_n^{(i-1)} \end{vmatrix} = (-1)^{i+j} \begin{vmatrix} C_j^{(1)} & C_{j+1}^{(1)} & C_{j+1}^{(1)} & C_n^{(1)} \\ \vdots & \vdots & \vdots & \vdots \\ C_j^{(i-1)} & C_{j+1}^{(i-1)} & C_{j+1}^{(i-1)} & C_n^{(i-1)} \end{vmatrix}$$

but because

$$C_n^{(i)} = \frac{p!}{q!(p-q)!} = \frac{p}{q} C_{n-1}^{(i)}$$

Therefore, after taking the proper factors out of every row and column from the above determinant we can get

$$m_{i,j} = (-1)^{i+j} \frac{j(j+1)\dots(i-1)(i+1)\dots n}{1 \times 2 \times 3 \dots \times (n-j)} \begin{vmatrix} 1 & 1 & 1 & 1 \\ C_{j+1}^{(1)} & C_{j+2}^{(1)} & C_j^{(1)} & C_{n-1}^{(1)} \\ \vdots & \vdots & \vdots & \vdots \\ C_{j+1}^{(i-1)} & C_{j+2}^{(i-1)} & C_j^{(i-1)} & C_{n-1}^{(i-1)} \end{vmatrix}$$

Using the conclusion of the problem above to the above determinant, we get

$$\begin{aligned} m_{i,j} &= (-1)^{i+j} \frac{n!}{i(n-j)!(j-1)!} \frac{1}{1! 2! \dots (n-j-1)!} \frac{1}{1! \dots (i-j-1)!} \\ &\quad \times \frac{(i-j+1)!(i-j+2)! \dots (n-j)!}{1 \times 2 \times \dots \times (n-i)} \\ &= (-1)^{i+j} \frac{n!}{i(j-1)!(i-j)!(n-i)!} = (-1)^{i+j} \frac{n!}{i!(\frac{n}{i}-i)!} \\ &\quad \times \frac{(i-1)!}{(j-1)!(i-j)!} = (-1)^{i+j} C_i^j C_i^{i-j} \end{aligned}$$

Henceforth

$$f_i(u) = \sum_{j=0}^i m_{i,j} u^j = \sum_{j=0}^i m_{i,j} u^j = \sum_{j=0}^i (-1)^{i+j} C_i^j C_i^{i-j} u^j$$

This agrees completely with the results of Equation (3).

#### IV. THE SECOND METHOD

From Equation (6), we know that 0 is the origin of  $f'_j(u)$  and it is at least  $j-1$  multiple. Similarly, from Equation (7), we know that 1 is the origin of  $f'_j(u)$  and it is at least  $n-j$  multiple. Because

$$j-1+(n-j)=n-1$$

and  $f'_j(u)$  is an  $n-1$  order polynomial, therefore, 0 just happens to be its  $j-1$  multiple origin and 1 is its  $n-j$  multiple origin. Thus, we can let

$$f'_j(u) = a_j u^{j-1} (1-u)^{n-j}$$

where  $a_j$  is a constant to be determined and the following is the determination of this constant. Because

$$\begin{aligned} 1 &= f_j(1) - f_j(0) = \int_0^1 f'_j(u) du = a_j \int_0^1 u^{j-1} (1-u)^{n-j} du \\ &= a_j B(j, n-j+1) = a_j \frac{\Gamma(j) \Gamma(n-j+1)}{\Gamma(n+1)} \\ &= a_j \frac{(j-1)! (n-j)!}{n!} \end{aligned}$$

here  $\Gamma(x)$  and  $B(x, y)$  are the well known gamma and beta functions, therefore

$$a_j = \frac{n!}{(j-1)! (n-j)!} = n C_{n-j}^{j-1}$$

Then

$$\begin{aligned} f_j(u) &= f_j(u) - f_j(0) = \int_0^u f'_j(t) dt = n C_{n-j}^{j-1} \int_0^u t^{j-1} (1-t)^{n-j} dt \\ &= n C_{n-j}^{j-1} \int_0^u t^{j-1} \left( \sum_{p=0}^{n-j} (-1)^p C_{n-j}^{p,j} t^p \right) dt = n C_{n-j}^{j-1} \sum_{p=0}^{n-j} (-1)^p C_{n-j}^{p,j} \int_0^u t^{p+j-1} dt \\ &= n C_{n-j}^{j-1} \sum_{p=0}^{n-j} (-1)^p C_{n-j}^{p,j} \frac{1}{p+j} u^{p+j} \end{aligned}$$



Let  $i = p + j$ , then

$$\begin{aligned}
 f_i(u) &= n C_{i-1}^{n-1} \sum_{j=0}^n (-1)^{i-j} C_{j-1}^{n-1} \frac{1}{i} u^i \\
 &= \sum_{j=0}^n (-1)^{i-j} \frac{n}{i} \frac{(n-1)!}{(j-1)!(n-j)!} \frac{(n-j)!}{(i-j)!(n-i)!} u^i \\
 &= \sum_{j=0}^n (-1)^{i-j} \frac{n!}{i!(n-i)!} \cdot \frac{(i-1)!}{(j-1)!(i-j)!} u^i \\
 \text{i.e.} \quad f_i(u) &= \sum_{j=0}^n (-1)^{i-j} C_{i-1}^{n-1} C_{j-1}^{n-1} u^i
 \end{aligned}$$

This completely agrees with the results in Equation (3).

This paper was completed under the guidance of Professor Wu Jiunhen. Professor Chan Kenshao of the Chinese Science Technology University also reviewed the entire paper in detail. He also provided complete instructions on the calculation method. We wish to express our sincere gratitude here.

#### REFERENCES

- [1] P. Bézier, "Numerical Control-Mathematics and Applications", John Wiley and Sons, London (1972)
- [2] Chan Ken Sheo and Wu Jiunhen, "Mathematical Basis of Bézier curves and its calculation" "Aeronautics Abroad", vol 1-6, 1979
- [3] Chan Kenshao and Wu Jiunhen, "On the mathematical Basis of Bézier curves", "Computational Mathematics", vol 1, 1980.

#### Abstract

In his book "Numerical Control" Professor P. Bézier gives an excellent exposition of his technique in CAGD. Bézier's Basic functions  $f_{n,i}(u)$  are shown in (2) and (3). Bézier's curves have a number of important and interesting geometric properties of the basic functions. As there has been no literature on the derivation of these basic functions so far, this paper attempts to prove in two different ways that the expressions of basic functions can be determined completely by three simple and reasonable geometric properties of the Bézier's curves.

## THE COMPLETELY SUCCESSFUL VISIT TO THE USA BY THE DELEGATION OF CHINESE SOCIETY OF AERONAUTICS AND ASTRONAUTICS

The delegation of the Chinese Society of Aeronautics and Astronautics with President Shen Yuen of CSAA as the leader and Vice President Yao Ehuin of CSAA and Vice President of the Chinese Institute of Aeronautics and Astronautics Liu Hongchi as the assistant leaders and a total of nine people, departed to visit the United States of America upon invitation by the American Institute of Aeronautics and Astronautics on April 30 this year.

The delegation stayed in the US for three weeks. They attended the "Year 2000 Global Technology" Technical Meeting sponsored by the American Institute of Aeronautics and Astronautics. They also visited the Lewis and Langley Research Centers of NASA, FAA, Environment Research Institute, General Electric Corporation, Lockheed Aircraft, Grumman Aircraft Company, O'Hare International Airport, Massachusetts Institute of Technology and Georgia Institute of Technology. These are the famous scientific research institutes, production departments and higher education institutes. In addition, the delegation was also invited to visit the branch offices of Boeing Company and Bendix Corporation.

The delegation was highly regarded by the American Aeronautical and Astronautical Society and received the hospitality of many well known scientists and related people. Both Chinese and American personnel carried out a wide range of contact and discussion on the scientific technical problems in aeronautics and astronautics as well as on problems in mutual communication and exchange of information. The visit by our delegation to the US has some very good effect on the promotion of the friendly relationship between the technical personnel in aeronautics and astronautics in China and in the US. It also has a significant meaning in the promotion of the development of the aeronautical and astronautical industries in our country.

## THE VISIT TO CHINA BY THE DELEGATION OF THE JAPAN SOCIETY FOR AERONAUTICAL AND SPACE SCIENCES

Upon the invitation of the Chinese Society for Aeronautics and Astronautics, the five member delegation of the Japan Society for Aeronautical and Space Sciences led by the former president of the Japan Society for Aeronautical and Space Science, Professor HoChun Ni Ma and Deputy Director of Japan Institute of Aeronautical and Space Sciences, Dr. Wu Tien Tsun arrived in Beijing on April 9. On April 16, they left Beijing on a visiting tour of Shenyau, Shanghai and Hangchow. They returned to Japan on April 24. During their visit in China, they visited the Mechanics Institute of the Chinese Academy of Science, Beijing Aeronautics Institute, Beijing Institute of Aerodynamics, Shenyau Li-Ming Machinery Company, Shenyau Soong-Lin Machinery Company, Hangchow Textile Factory and Double-Peak Commune Group. There were four technical seminars and four special topic discussion sessions in Beijing, Shenyau and Shanghai.

The members of the delegation of the Japan Society for Aeronautical and Space Sciences were composed of three college professors and one engineering Ph. D. and they were all highly regarded in the technical society in Japan. They were all well prepared before their visit to China. During the seminars and discussion sessions, they introduced the development in aeronautical science research in Japan as well as the advancement in aerodynamics, aeronautical engines, control and aeronautical mechanics. They also introduced the Japan Society for Aeronautical and Space Sciences, Japan Institute of Aeronautics and Astronautics and the research on the development of aircraft with short distance take-off and landing capabilities. These reports are beneficial to our aeronautical technical staff for the better understanding of the situation in aeronautical studies in Japan. Their visit to China has contributed greatly to the friendly relationship and technology exchange between Chinese and Japanese technical members in aeronautics.

## THE CONFERENCE ON THE POLICY OF CAGD/CAM TECHNICAL DEVELOPMENT

The Chinese Society of Aeronautics and Astronautics (CSAA) held a meeting on "Policy of Computer Assisted Geometrical Design and Computer Assisted Manufacturing (CAGD/CAM) of Aircraft Technique Development" in April 1980 in Suechow. Over 50 representatives from 30 organizations attended the meeting. Most of the representatives are experts from areas such as scientific research, education, front line in production as well as professors and engineers. There were also several leading comrades participating in the meeting. In the meeting the present status and the outlook in future development of domestic computers, the CAD/80 international meeting and a briefing on the establishment of the regulations in Computer Assisted Manufacturing (CAM) were introduced. In addition, sufficient and enthusiastic discussions were on six special topics regarding the major problems to be resolved in the short term and long term development of CAGD/CAM technique for the aircraft manufacturing industries in our country, viz., the connection between CAGD and CAD, the equipment of digital control machinery, the arrangement of electronic computer and the exchange type figure displacement device, the development of applied software, the rational equipment of CAGD/CAM machinery in the aircraft factory and the coordinating relationships between higher education institutions, research institutes and factories. We reviewed some of the accomplishments in the basic method research, applied program systems and numerical control devices made by the aircraft manufacturing industry in our country in the past decade using the CAGD/CAM technique. These accomplishments were applied in development and production work which resulted in the accumulation of some experience and the training of technical personnel. But due to the lack of understanding of the function of this advanced technique, its economical effectiveness was also not significant. All the comrades attending the meeting acknowledged the CAGD/CAM technique is a major reform in the conventional technology. It is a useful tool in the fast design and manufacturing of aircraft. It is an important landmark

in modern aeronautical industries which should be promoted rapidly. Therefore, everybody believed that this conference on the policy of the CAGD/CAM technique development was very important and timely.

On the basis of comparing the situation with foreign countries and summarizing the realization experience in our country, the meeting led to the rational suggestion of quite a few relevant policies of the CAGD/CAM technique development as well as the study and discussion of the current status in our country.

The representatives acknowledged that the computer is the basic material required in the advanced development of CAGD/CAM technique. The selection of the model should be unified. The characteristics should take the requirements of computer assisted design, manufacturing and management into consideration. It should have more abundant present and potential software resources and it should be readily available. The exchange type diagram display unit is an important peripheral equipment required to develop this technique. During the importing of foreign equipment, we should also select the model in a unified manner to make the proper arrangement. In addition, work should begin promptly on the development of basic and applied software in the display of diagrams. On the basis of the presently available materials and techniques, a small scale practical applied software system should be established which includes features such as geometrical model making, diagram sketching, automatic compilation, simple design analysis, etc. In the future, based on the acquisition of computers of a certain size, we should develop a higher function and larger size exchange type CAGD/CAM applied software system in order to be suited for the requirements in the development of new aircraft and to increase the economical effect of this combined technology. To be able to promote work in this area better, the meeting recommended the establishment of a software collaboration network to determine the guideline and standard of the compilation of the software as well as to organize functions such as information exchange and program evaluation.

We also suggested the formation of short-term training courses and lectures in order to raise the standard of the leading officials and technical personnel. Relevant higher educational institutions should try to train students both at the undergraduate and graduate levels in this new special technical area and attempt to investigate some new methods. Some feasibility and exploratory experiments should be carried out in order to have a handle on the direction of future development in this new technology.

In the latter part of the meeting, the founding of a CAGD/CAM special topic group was suggested and future activities were planned. It is expected that a technical meeting on the connection between CAD and CAGD and relevant systems will be held during the second season in 1981.

## BASIC PRINCIPLES OF MANUSCRIPTION SELECTION FOR "ACTA AERONAUTICA ET ASTRONAUTICA SINICA"

"Acta Aeronautica et Astronautica Sinica" is a technical periodical organized by the Chinese Society for Aeronautics and Astronautics. It is openly published both domestically and abroad. This journal is under the guidance of Marxism, Leninism and the thoughts of Mao tse-tung. It fully executes the principles of the "bloom and contend" movement to expand technical exchange in order to promote the modernization of aeronautical and astronautical technologies.

This journal is primarily designed to publish new technical results in the areas of astronautics and aeronautics. The readers are primarily specially trained personnel in the research, teaching, design, production and users in aeronautical and astronautical technologies.

(I) This journal publishes the following type of manuscripts:

1. New accomplishments related to aeronautics and astronautics, including creative technical papers of technology and materials in aerodynamics, aeronautical mechanics, design and structural strength of aeronautical vehicles, power equipment, electronic technology and automatic control, etc., as well as results and experience in the application of new theories and new techniques.
2. Creative technical notes, reports and commentaries in relevant aeronautical and astronautical techniques.
3. Introduction and comments on literature and books in aeronautics and astronautics.
4. Activities of the technical communities both domestic and abroad.

## (II) Requirements of the manuscript:

1. The analysis, computation and experimental data in the manuscript should be accurate. Its structure should be compact. It should be clear and based on rigorous theoretical ground. The language should be simple and easy to understand. Each manuscript is limited to 5000 words. Creative papers should not exceed ten thousand words (including figures and tables).

2. The manuscript should be written in ink by pen or size 16 block paper legibly. The terminology and units should be consistent throughout the paper.

3. The figures should be plotted using drafting paper according to engineering diagram specifications. The captions should be written by pencil. The position of the figure should be indicated in the manuscript by drawing a block occupying three blocks. The figure number, title and remarks should be written below the corresponding block. Do not attach the figures to the manuscript. They should be attached as an appendix.

4. Equations should be written in the middle of the paper. The sequence number of the written in ( ) to the right of the equation without adding a dotted line.

5. References should be listed by the sequence as they are mentioned in the text in the end of the paper. Only major and published references are required to be listed. The format is as follows: [number] authors(s), name of the book, publisher (year), page number. [number] authors(s), title of the article, journal name, volume number, book number (year), page number.

6. An English abstract, an English title and the name of author's working institution and name in English should be included in the manuscript. The abstract in Chinese should not exceed 300



words. The English abstract ought to be more in detail and generally should be between 500 to 700 words.

7. If the manuscript has already been published in the open literature, then it will not be accepted by "Acta Aeronautica et Astronautica Sinica".

(III) "Acta Aeronautica et Astronautica Sinica" is a journal published openly worldwide. We do not accept manuscripts involved in national security. The authors are responsible to prevent sensitive information from leaking out in the paper.

(IV) All manuscripts published in "Acta Aeronautica et Astronautica Sinica" will be rewarded financially according to the regulations.

**DATE**  
**ILME**